A Higher-Order Panel Method for Large-Amplitude Simulations of Bodies in Waves

by

Donald Gregory Danmeier

B.S., Mechanical & Environmental Engineering,
University of California at Santa Barbara, 1991

M.S., Naval Architecture & Offshore Engineering,
University of California at Berkeley, 1994

Submitted to the Department of Ocean Engineering
in partial fulfillment of the requirements for the degree of

Doctor of Philosophy in Hydrodynamics

at the

MASSACHUSETTS INSTITUTE OF TECHNOLOGY

February 1999

Author .....
Department of Ocean Engineering
November 6, 1998

Certified by .....
J. Nicholas Newman
Professor Emeritus of Naval Architecture
Thesis Supervisor

Accepted by .....
J. Kim Vandiver
Chairman, Department Committee on Graduate Students

A Higher-Order Panel Method for Large-Amplitude Simulations of Bodies in Waves

by

Donald Gregory Danmeier

Submitted to the Department of Ocean Engineering
on November 6, 1998, in partial fulfillment of the
requirements for the degree of
Doctor of Philosophy in Hydrodynamics

Abstract

In this thesis, we simulate large-amplitude motion of three-dimensional bodies in waves using a higher-order boundary element method. A 'geometry-independent' approach is adopted in which the representation of the body surface is separated from the discretization of the hydrodynamic solution.

Traditional formulations of the wave-body problem assume small-amplitude waves and body motions, and perturbation expansion about the mean position of the body and free surface leads to a completely linearized system. In the present thesis, the body boundary condition is imposed exactly, but disturbances at the free-surface are assumed to be small enough to justify linearization. Previous applications of this so-called body-exact problem have concentrated on the analysis of heave and pitch motion of ships with forward speed. This study focuses on marine applications where a large-amplitude response is induced by small-amplitude incident waves.

The time-varying nature of the body-exact formulation makes its numerical solution computationally intensive. Therefore, a new 'higher-order' panel method has been developed to overcome inefficiencies associated with the conventional constant-strength planar-panel approach. Unlike most higher-order schemes, the present method separates the discretization of the hydrodynamic solution from the representation of the body surface by applying a B-spline description of the potential over a generic parameterization of the geometry. This allows for accurate (or even analytic) representation of the surface while retaining the desirable characteristics of higher-order methods, most notably improved efficiency and the ability to evaluate gradients of the potential needed for nonlinear analyses. Robustness and efficiency of the present method are demonstrated by its application to three problems in which the large-amplitude response of the body is important.

In the first example, we examine the hydrodynamic loads on an underwater vehicle during a near-surface maneuver. The vertical drift force is found by integrating the quadratic Bernoulli pressure, and its variation with respect to submergence is shown to complicate the control of the vessel.

Next, multi-body interactions are examined in the context of the drift motion of a floating body in the vicinity of a fixed structure. Here, the presence of the structure is shown to repel the floating body against the direction of incident wave propagation for certain conditions.

In the final application, we examine instabilities of floating bodies to illustrate the importance of accounting for finite-amplitude motions. Period doubling and exponentially large motions in the numerical simulations are related to parametric forcing captured by the body-exact formulation.

Thesis Supervisor: J. Nicholas Newman
Title: Professor Emeritus of Naval Architecture

Acknowledgments

I am deeply indebted to all of my mentors, colleagues, family and friends for their support of the work contained in this thesis.

Throughout my studies, Professor Nick Newman provided academic guideness with patience and kindness. Thank you Dr. Tom Korsemeyer for your constant advice, encouragement and interest in my research. I am also thankful to Professors Jacob White and Jake Kerwin, as well as Dr. Chang-Ho Lee for their assistance during the preparation of this document.

Working at the Computational Hydrodynamic Facility has been extremely gratifying because of the friendly and supportive atmosphere created by Harry Bingham, Xuemei Zhu, Hiren Maniar, Thomas Farstad, Gro Sagli, and every other member of the group. I must also thank my OE classmates and DUSP friends for their company and laughs during all of my late nights on campus.

I am tremendously thankful for the love from my family that allowed me to leave home and build a life away from California. The generosity and care I recieved from my surrogate Brookline family made the past few years incredibly rich. To Nigel and Deborah, thanks for sharing your home and lives. To Jorgen, thanks for sharing the sandbox in preschool and the 3^{rd} floor in graduate school.

Major financial support of this work was provided by an Office of Naval Research grant under an Augmentation Award for Science and Engineering Research Training, contract #N00014-94-1-0837. Additional support came from ONR contract #N00014-97-1-0827, under the direction of Naval Facilities Engineering Services Center, and the Consortium on Numerical Analysis of Wave Loads on Offshore Structures, which included: Chevron Petroleum Technology Co., Statoil, Norsk Hydro Research Centre, Saga Petroleum A.S., Det Norske Veritas, Mobil, Shell Development Co., Exxon Production Research Co., Offshore Technology Research Center, David Taylor Model Basin, and Petrobrás.

Contents

List of Figures

List of Tables

Chapter 1

Introduction

1.1 Potential flow & panel methods

Knowledge of wave induced loads and motions is necessary for both the design and operation of ships and offshore structures. Over the past few decades computational hydrodynamics has matured as a powerful tool for ocean engineers and naval architects. Today, numerical simulations complement model tests during preliminary design stages. The low cost and relative ease of performing these computations allow for the evaluation of many design concepts over a range of sea conditions. Continued increase in computer power will undoubtedly spread the utility and popularity of numerically-based tools.

The success of any particular theory relies largely on its ability to capture the natural phenomena of interest. For a wide variety of engineering applications potential flow theory provides a framework that is mathematically attractive and physically appropriate. The assumptions of an ideal fluid and irrotational motion allow the flow field to be represented by the gradient of a scalar function, which is the solution of the Laplace equation and subject to appropriate boundary and initial conditions. Kinematic and dynamic boundary conditions imposed at the free surface ensure the correct wave-like behavior of the potential. This initial-boundary-value problem may be recast as an integral equation with the aid of Green's theorem and solved numerically by boundary element (panel) methods.

Since the pioneering work of Hess and Smith [13], panel methods have been applied to a wide variety of problems. Here, the integral equation is enforced by distributing singularities over a collection of *panels* that represent the body geometry. Methods based on a *free-surface Green function* automatically satisfy the radiation and linearized free-surface boundary conditions, and the body boundary condition is enforced by discretizing the body surface. The *Rankine* panel method uses the simple source as its fundamental singularity, therefore panels are required on the body and some portion of the free surface in order to numerically impose the boundary conditions. Since the free-surface condition is enforced directly, Rankine methods may accept various forms of this boundary condition and include terms neglected by formulations based upon the free-surface Green function.

The numerical implementation of these methods has various degrees of sophistication. *Lower-order* methods refer to schemes that use planar quadrilaterals or triangles to model the body, with the velocity potential assumed constant over each panel. This simplifies the integration of singularities over the surface, but a large number of elements are required to obtain accurate results. For many applications, such as the simulation of large motions induced by drift forces, evaluation of the gradient of the potential becomes important. In these instances, lower-order methods often fail to produce accurate descriptions of the necessary derivatives. While this may be overcome by deriving an alternative integral equation, such an approach fails if the second derivative of the potential is required. *Higher-order* panel methods have been developed to overcome the deficiencies of constant-strength planar-panel schemes. In addition to accurate evaluation of gradients, the efficiency of higher-order schemes makes computations of the first-order wave loads possible in cases where the lower-order approach would require a prohibitively large number of planar panels.

The present thesis is aimed at developing state-of-the-art numerical tools that may be applied to large-amplitude motion simulations. Here, restrictive assumptions of

small body motions are overcome by imposing the body boundary condition exactly. Gradients required for the evaluation of drift forces are computed with a novel higher-order panel method. The present scheme accepts a very accurate representation of the geometry, and only discretizes the hydrodynamic solution. The utility and robustness of this new approach are demonstrated by its application to a variety of wave-body problems.

1.2 Linear time-domain formulations

If the slope of the incident waves is small, the initial-boundary-value problem may be linearized. Therefore, we may expect the response of a stable body to be proportional to the amplitude of the incident waves, and perturbation expansion allows the problem to be defined over the mean position of the body and free surface. Fourier decomposition may be used to transform the transient problem in the *time domain* to a time-harmonic problem in the *frequency domain*, which is then solved at discrete frequencies. Although frequency-domain analysis is efficient at predicting the steady-state response of the body, stating the problem directly in the time domain may be advantageous for several reasons, including: frequency-domain formulations are less efficient in solving forward-speed problems because of difficulties in evaluating the required Green function [1], and nonlinearities may be directly incorporated in time-domain simulations.

The application of integro-differential equations of motion for wave-body problems is usually attributed to Cummins [5], who assumed linearity and small body motions in order to introduce the impulse response function. Ogilvie [49] gives a thorough discussion of the hydrodynamic problems involved in such a decomposition, and relates transient quantities to their frequency-domain analogs. Liapis [28] and Korsemeyer [21] obtained numerical solutions of impulse response functions for three-dimensional flows about bodies of arbitrary shape. Both authors used the transient

free-surface Green function to solve a series of linear radiation problems forced by impulsive motions, and discussed numerical issues involved in obtaining time-domain results from lower-order panel codes. King [20] and Bingham [2] extended, respectively, the work of Liapis and Korsemeyer by computing response functions for the linear diffraction problem. King forced the diffraction problem with a broad-banded but non-impulsive wave system, while Bingham used an impulsive incident wave profile. Parallel work with the Rankine panel method was carried out by Kring [22]. He extended the thesis of Nakos [39], and imposed the *double-body* free-surface condition to account for terms neglected by the *Neumann-Kelvin* approximations inherent in the transient free-surface Green function.

1.3 Nonlinear time-domain formulations

In special cases, extensions to linear theory that account for steep waves and/or large body motions may be appropriate. Perturbation expansion of the complete problem leads to a series of linear initial-boundary-value problems, one at each order. Numerical solutions of the second-order problem in the frequency domain have been reported in the literature [46, 27], but computations of the corresponding time-domain problem are less common. Instead, more attention has been devoted towards directly incorporating various nonlinearities into time-domain formulations.

An obvious extension of the traditional linear model is to impose the body boundary condition on the instantaneous position of the structure. This lifts the restriction of small-amplitude motions, but disturbances at the free surface must remain linearizable. This *body-exact* problem has been solved with various degrees of success. Difficulties of automatically re-gridding surface piercing bodies limited Magee [34] to the study of submerged bodies. Lin and Yue [29] and Magee [33] presented results for floating bodies undergoing finite-amplitude heave and pitch motions using lower-order panel methods. Huang [16] combined the exact body-boundary condition with

a free-surface condition linearized about the incident wave profile. The *weak-scatter* hypothesis used by Huang allows for both body motions and incident waves of large amplitude. Results of these researchers suggest that the exact treatment of the body boundary condition improves the simulation of large-amplitude motions.

A more complete treatment of the free-surface nonlinearities may be found in the *Mixed Eulerian Lagrangian* (MEL) method of Longuet-Higgins [32]. Early MEL implementations involved two-dimensional or axisymmetric wave flows (Vinje and Brevig [55], Lin [30], Dommeruth [7]). More recently, the method has been extended to general three-dimensional wave-body applications, with Ferrant's [11] work representative of its current state. Presently, the numerical effort associated with such computations is extreme, and problems with instabilities have yet to be fully sorted out.

1.4 Higher-order panel methods

Deficiencies of the constant-strength planar-panel method often limit its application. As mentioned earlier, higher-order methods have been developed to overcome difficulties in evaluating spatial derivatives of the potential. The efficiency of these methods have made the solution of computationally intensive problems more feasible. Most higher-order schemes allow for linear or quadratic variation of the geometry and potential by using first- or second-degree polynomials over individual panels. Hsin [15] and Maniar [36] developed a fundamentally different higher-order panel method based wholly on B-splines. This method allows the potential and geometry to have any degree of continuity, with basis functions of local or global support. The B-spline form of the potential provides a means of analytic differentiation of the solution. Therefore, the gradient of the velocity potential may be found without approximation. The efficiency of the method is demonstrated by its application to the analysis of problems with a large number of bodies [35].

Recently, Lee et. at. [24] presented results using a *geometry-independent* higher-order method. Here, the velocity potential is described by a set of B-spline basis functions, but the body surface may have any regular parameterization. Since no other assumptions are placed on the representation of the body surface, the hydrodynamic solution is completely separated from the geometric model. There are several advantages of such a scheme. Firstly, its compatibility with commercial computer aided design packages allows for the most convenient and accurate description of the body geometry. Secondly, an appropriate hydrodynamic discretization may be selected irrespective of the geometric modeling. In addition, the separation of geometric and hydrodynamic representation may lead to meaningful adaptive error control of the three-dimensional boundary element method. Finally, the fact that many hydrodynamic discretizations may be applied to a single geometric parameterization has the practical advantage of saving users from reconstructing new descriptions of the surface during the several computations needed to obtain a converged numerical solution.

1.5 Present thesis

The scope of the present thesis includes the development of new higher-order tools and their application to the body-exact problem. A robust panel method has been developed by adapting techniques from computer aided design to the geometry-independent higher-order methodology described above. A substantial portion of this thesis concerns the re-gridding of the body surface in the geometry-independent context. We demonstrate the effectiveness of the present method by simulating large-amplitude motions where robust evaluation of derivatives is needed. Superior efficiency of this higher-order method is observed with respect to the constant-strength planar-panel method. Additionally, the geometric tools developed in this thesis will aid the application of the higher-order method to more sophisticated nonlinear for-

mulations of the wave-body problem.

The initial-boundary-value problem and its associated integral equation are stated in Chapter 2. There, we explicitly state the assumptions of the hydrodynamic model. Chapter 3 describes the numerical schemes, which include algorithms that trim the body surface and solve for the potential. The time-dependent domain requires re-discretization of the geometry, and an automated trimming/interpolation scheme is introduced for this purpose. Since we have chosen a geometry-independent approach, the integral equation must be approximated by direct quadrature. Adaptive sub-division and triangulation are used in evaluating the singularity of the free-surface Green function.

Direct pressure integration is performed, as outlined in Chapter 4, in order to calculate oscillatory and drift forces on the body. In order to simulate the motions of a body, Newton's law and the hydrodynamic flow must be solved simultaneously. The equations governing translation and rotation of a rigid body are also presented.

Results that demonstrate the utility of the body-exact formulation, and the accuracy of our higher-order methods, are presented in Chapters 5, 6, and 7. Single- and multiple-body applications are chosen where large low-frequency motions parametrically influence the response at the higher wave frequency. In each case, small-amplitude waves provide the forcing of large-amplitude body motions.

Conclusions drawn from applications of the present method to the body-exact problem are presented in Chapter 8. Recommendations for future extensions are discussed there as well.

Chapter 2

Linear and Body-Exact Models

Even with the idealizations of a perfect fluid and irrotational flow, the resulting hydrodynamic problem is very complicated. This chapter describes more manageable formulations which result from simplifying the boundary conditions in some way. Following other investigators, we linearize the free-surface boundary condition but impose the body boundary condition without approximation. This will limit the application of our formulation to cases where the body generates small amplitude waves, but its motion is otherwise unrestricted.

Throughout this discussion, various decompositions of the velocity potential are introduced as an aid in contrasting the 'body-exact' model with conventional formulations of the ship motion problem. We compare our treatment of the free surface with another common linearization. In addition, the conventional perturbation applied at the body surface is briefly outlined in order to distinguish the present formulation from traditional approaches.

2.1 Governing equations and boundary conditions

The equations governing fluid motion are derived in an inertial reference frame. Let $\mathbf{X} = (X, Y, Z)$ [1] be a position vector of a point on the body surface in the $OXYZ$ earth-fixed coordinate system. The XY plane lies at the mean sea level, and Z is positive in the upward direction.

[1] Boldface characters are used to denote vector quantities.

We assume the fluid to be inviscid, incompressible, and free of surface tension. With the additional assumption of irrotational flow, Helmholtz' theorem ensures that the fluid velocity may be expressed as the gradient of a scalar potential,

$$\mathbf{V}(\mathbf{X},t) \equiv \nabla\Psi(\mathbf{X},t). \tag{2.1}$$

The total flow is comprised of a specified incident wave field and a disturbance due to the presence of the body. Let

$$\Psi = \Phi + \varphi, \tag{2.2}$$

where Φ represents the disturbance due to the presence of the body, and φ is the incident potential. We seek a solution of the body potential, Φ.

For incompressible fluids, the conservation of mass simplifies to the Laplace equation,

$$\nabla^2\Psi = 0. \tag{2.3}$$

The other fundamental conservation law concerns the balance of momentum. For irrotational flow of an ideal fluid, this leads to the Bernoulli equation. Therefore, the fluid pressure is

$$p - p_a = -\rho\left(\Psi_t + \frac{1}{2}|\mathbf{V}|^2 + gZ\right), \tag{2.4}$$

where p is the fluid pressure, p_a is the atmospheric pressure, and ρ is the mass density of the fluid. The free-surface elevation, ζ, is found by applying (2.4) at the air/water interface,

$$\zeta = -\frac{1}{g}\left(\Psi_t + \frac{1}{2}|\mathbf{V}|^2\right) \quad \text{on} \quad Z = \zeta. \tag{2.5}$$

Conditions must be imposed on the bounding surfaces of the fluid domain in order to fully define the boundary-value problem. At the body/fluid interface, the appropriate boundary condition is a statement of no-flux into the impermeable body surface. Therefore, the body boundary condition is

$$(\mathbf{U} - \mathbf{V}) \cdot \mathbf{n} = 0 \quad \text{on} \quad \mathcal{B}(t), \tag{2.6}$$

where $\mathcal{B}(t)$ is the wetted body surface, and $\mathbf{U}$ is its velocity.

The free surface requires two boundary conditions since both Ψ and ζ are unknowns. Let the air/water interface be described by

$$F(\mathbf{X},t) = Z - \zeta(X,Y,t) = 0. \tag{2.7}$$

Since this is a material surface, the kinematic free-surface boundary condition is

$$\frac{\partial F}{\partial t} + \mathbf{V}\cdot\nabla F = 0, \tag{2.8}$$

which may be written as

$$\Psi_Z = \zeta_t + \Psi_X\zeta_X + \Psi_Y\zeta_Y. \tag{2.9}$$

The dynamic free-surface boundary condition states that the fluid pressure just below the free surface must equal the atmospheric pressure above. Since this must hold along the entire free surface, the substantial derivative of the fluid pressure at the free surface must be equal to zero,

$$\left(\frac{\partial}{\partial t} + \mathbf{V}\cdot\nabla\right)\left(g\zeta + \frac{\partial\Psi}{\partial t} + \frac{1}{2}|\mathbf{V}|^2\right) = 0. \tag{2.10}$$

Substituting (2.9) into the expression above gives a single nonlinear free-surface boundary condition,

$$\Psi_{tt} + 2\nabla\Psi\cdot\nabla\Psi_t + \frac{1}{2}\nabla\Psi\cdot\nabla(\nabla\Psi\cdot\nabla\Psi) + g\Psi_Z = 0 \ \text{ on } \ Z = \zeta. \tag{2.11}$$

In three dimensions, the fluid velocity due to the presence of the body decays in amplitude and is negligible far from the disturbance. Denoting S_∞ as an imaginary surface a great distance away from the body, we have

$$\nabla\Phi \to 0 \ \text{ at } \ \mathrm{S}_\infty. \tag{2.12}$$

In addition, a radiation condition must be imposed to ensure that the body produces outgoing waves.

Two initial conditions must be imposed at the free surface in order to uniquely determine the subsequent fluid motion (see Stoker [53]). For flows beginning from a state of rest, the appropriate conditions are

$$\Psi = \Psi_t = 0 \text{ on } \zeta = 0,\ t = 0 \ . \tag{2.13}$$

The above initial boundary-value problem is exact within the limits of potential theory, but complications of the boundary conditions preclude any straightforward solution. Some simplifications are necessary in order to make the problem tractable. In particular, the free-surface and body boundary conditions will be the starting points of various linearizations.

2.2 Linearization at the free surface

If the amplitude of the wave motion is small compared to its characteristic length, the free-surface boundary condition may be linearized by simply neglecting terms quadratic and higher-order in Ψ. In these cases, the difference between $Z = \zeta$ and $Z = 0$ is a small first-order quantity, so we can apply the linear free-surface boundary condition at the undisturbed surface and maintain a consistent linearization. This straightforward linearization reduces (2.11) to

$$\Psi_{tt} + g\Psi_Z = 0 \text{ on } Z = 0. \tag{2.14}$$

The simplifications of this linearization are significant, and we should apply the above condition carefully. Neglecting nonlinear terms in the free-surface boundary condition will restrict the amplitude of the incident waves, the velocity of the body, or the geometry of the surface. Although not implemented in this thesis, the following decomposition of the body potential is instructive, and reveals what flow effects the above linearization neglects.

Assume the body oscillates while translating steadily in the $+X$ direction at speed U. The three coordinate systems shown in Figure 2-1 will be used to describe the

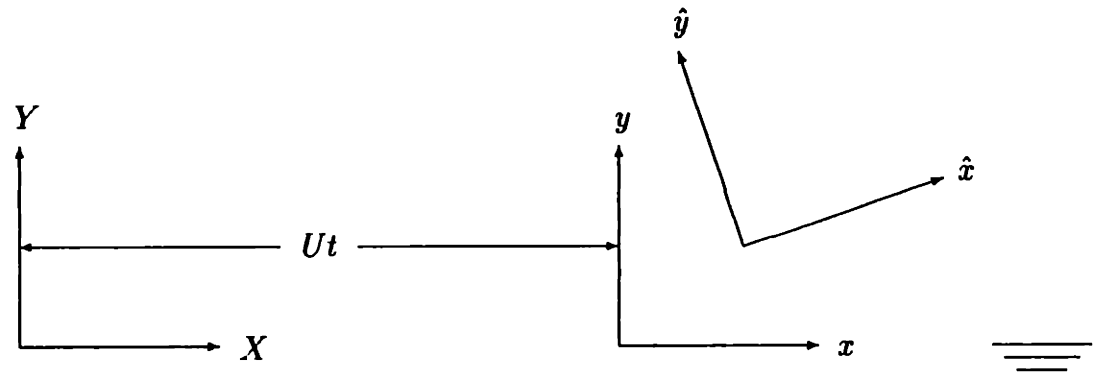

Figure 2-1: Two-dimensional view of the earth-fixed, steady, and body-fixed coordinate systems.

linearization of the exact initial-boundary-value problem. $\mathbf{X}$ denotes a point on the body surface with respect to the earth-fixed frame. This same point has a position vector $\hat{\mathbf{x}} = (\hat{x}, \hat{y}, \hat{z})$ in a body-fixed coordinate system, $\hat{o}\hat{x}\hat{y}\hat{z}$. A third coordinate system, the $oxyz$ reference frame, moves in the $+X$ direction at the steady velocity. Its position vector to the surface is $\mathbf{x} = (x, y, z)$. The steady and earth-fixed frames are related by

$$(x, y, z) = (X - Ut, Y, Z). \tag{2.15}$$

Care must be exercised when computing temporal derivatives. The rate of change measured in the earth-fixed frame is given by

$$\left.\frac{\partial}{\partial t}\right|_{OXYZ} = \left(\frac{\partial}{\partial t} - U\frac{\partial}{\partial x}\right)\Big|_{oxyz}. \tag{2.16}$$

In the steady frame, the velocity potential may be written as

$$\psi(\mathbf{x}, t) = \psi(X - Ut, Y, Z, t) \equiv \Psi(\mathbf{X}, t). \tag{2.17}$$

Breaking up the potential into steady and unsteady terms gives

$$\psi(\mathbf{x}, t) = \bar{\phi}(\mathbf{x}) + \tilde{\phi}(\mathbf{x}, t), \tag{2.18}$$

where $\bar{\phi}$ represents the steady-state flow as viewed in the $oxyz$ frame, and $\tilde{\phi}$ is the oscillatory potential. For general body shapes and velocity, the steady flow may not

necessarily be linearizable. Newman [45] compactly writes the steady free-surface boundary condition as

$$\frac{1}{2}\mathbf{W}\cdot\nabla(W^2)+g\bar{\phi}_Z=0 \ \text{ on } \ z=\bar{\zeta}. \tag{2.19}$$

Here, $\mathbf{W}$ is the relative velocity vector,

$$\mathbf{W}(\mathbf{x})=\nabla\bar{\phi}(\mathbf{x})-U\hat{i}, \tag{2.20}$$

and the steady wave elevation is given by the implicit equation

$$\bar{\zeta}=-\frac{1}{2g}\left(W^2-U^2\right) \ \text{ on } \ z=\bar{\zeta}. \tag{2.21}$$

Without the complications of the unsteady potential, it is worth appreciating the challenges in obtaining a solution of the steady flow. Like the full free-surface boundary condition, the nonlinearity of (2.19) and the fact that $\bar{\zeta}$ is unknown a priori present the main difficulties in obtaining a solution of the steady potential.

The unsteady motions are assumed to be linearly related to incident waves of small amplitude. Therefore, we may superpose a small oscillatory wave field onto the steady flow. A free-surface condition linear in $\tilde{\phi}$ comes from substituting (2.18) into (2.11). After Taylor expanding about the steady wave elevation, Newman arrives at

$$-(\tilde{\phi}_t+\vec{W}\cdot\nabla\tilde{\phi})\left\{\frac{\frac{1}{2}\frac{\partial}{\partial z}(\vec{W}\cdot\nabla W^2)+g\bar{\phi}_{zz}}{g+\vec{W}\cdot\vec{W}_z}\right\}+\tilde{\phi}_{tt}+2\vec{W}\cdot\nabla\tilde{\phi}_t \tag{2.22}$$
$$+\vec{W}\cdot\nabla(\vec{W}\cdot\nabla\tilde{\phi})+\frac{1}{2}\nabla\tilde{\phi}\cdot\nabla(W^2)+g\tilde{\phi}_z=0 \ \text{ on } \ z=\bar{\zeta}.$$

Although we have simplified the free-surface boundary condition, nonlinear steady terms in (2.22) make a solution of the linear unsteady problem extremely difficult. This means that regardless of whether or not the steady-state flow is of interest, we must accept some simplification of its potential in order to make the hydrodynamic problem tractable.

2.2.1 The Neumann-Kelvin approximation

The Neumann-Kelvin linearization borrows geometric assumptions from Michell's and slender body theories. Here, we exploit the fact that the disturbance caused by the

motion of the body will be proportional to its thickness (beam). This implies that the leading-order steady flow about thin or slender bodies is simply

$$\mathbf{W} = -U\hat{i} + O(\epsilon). \tag{2.23}$$

Substituting this approximation of the steady flow into (2.22) leads to the so-called Neumann-Kelvin free-surface condition,

$$\left(\frac{\partial}{\partial t} - U\frac{\partial}{\partial x}\right)^2 \tilde{\phi} + \frac{\partial \tilde{\phi}}{\partial z} = 0 \ \text{ on } \ z = 0. \tag{2.24}$$

This statement is equivalent to the linearized condition expressed in the earth-fixed reference frame, (2.14), so we may make some general observations regarding its validity.

We expect the Neumann-Kelvin approximation to reasonably model the steady flow if the body perturbs the uniform stream slightly at the free surface. This is true for thin or slender bodies, but (2.24) must be carefully applied to more full forms. Bingham [2] has used the Neumann-Kelvin free-surface condition to successfully solve for the steady resistance, sinkage force and trim moment of moderately fine ships. In addition to slender ships, this approximation may also be appropriate for bodies submerged below the free surface.

In some cases, large but slowly varying motions will parametrically influence the wave-frequency response. Here, the fast oscillations are of primary interest, and we accept the free stream approximation of 'steady' flow in order to simplify the free-surface boundary condition. Since the slowly-varying flow is of secondary importance, we expect the Neumann-Kelvin approximation to retain the desired accuracy of the solution. Higher-order terms may be important in special cases, such as the evaluation of wave-drift damping, but we will not attempt to model these subtle free-surface interactions.

2.2.2 The double-body approximation

Unlike the Neumann-Kelvin assumption, the double-body approximation includes a non-negligible perturbation of the uniform stream. Here, the steady potential is

$$\phi_{DB} = \bar{\phi} - Ux + O(\epsilon). \tag{2.25}$$

The idea is to model the non-wave steady disturbance as an infinite-fluid flow by applying a rigid-lid condition at the mean free surface,

$$\frac{\partial \bar{\phi}_{DB}}{\partial z} = 0 \ \text{ on } \ z = 0. \tag{2.26}$$

Nakos [39] provides a free-surface condition for the unsteady potential based on the above simplifications of the steady flow. After Taylor expanding to the $z = 0$ plane, he arrives at

$$\begin{aligned} \tilde{\phi}_{tt} + 2\nabla\phi_{DB} \cdot \tilde{\phi}_t + \nabla\phi_{DB} \cdot \nabla(\nabla\phi_{DB} \cdot \nabla\tilde{\phi}) + \frac{1}{2}\nabla(\nabla\phi_{DB} \cdot \nabla\phi_{DB}) \cdot \nabla\tilde{\phi} \\ + g\tilde{\phi}_z - \frac{\partial^2 \phi_{DB}}{\partial z^2}(\nabla\phi_{DB} \cdot \tilde{\phi}) = 0 \ \text{ on } \ z = 0. \end{aligned} \tag{2.27}$$

Clearly, the double-body free-surface condition reduces to the Neumann-Kelvin approximation as $\phi_{DB} \to -Ux$. Retaining the disturbance of the uniform stream may be important for accurate treatment of low speed steady flows past bluff bodies, but adds to the complexity of the free-surface boundary condition of the linear wave flow.

2.3 Exact versus linear body boundary conditions

We now turn our attention to the condition imposed at the fluid/body interface. Unlike the complete free-surface boundary condition, (2.6) is linear. However, it is implicit since the body position must be found by Newtonian mechanics, which itself requires a solution of the hydrodynamics.

The simplified free-surface boundary conditions described above produce a linear initial-boundary-value problem, and it is reasonable to expect a stable body to have

motions that are proportional to the amplitude of incident waves. If these oscillatory excursions about the *oxyz* frame are sufficiently small, the body boundary condition may be transferred to its mean position. To arrive at this fully-linearized body boundary condition, begin by decomposing the total potential in the steady frame as

$$\psi(\mathbf{x},t) = \phi_B + \phi_{SW} + \varphi + \phi_s + \sum_{k=1}^{6} \phi_k. \tag{2.28}$$

The *steady wave* potential, ϕ_{SW}, represents the wave-like disturbance due to the steady forward motion of the body. Its linearized free-surface boundary condition comes from Neumann-Kelvin or double-body approximations of the basis flow, ϕ_B. The *diffraction* problem consists of a specified incident wave field, φ, and its scattered waves, ϕ_s. The *radiation* potential, ϕ_k, describes the flow induced by the body as it moves in its k^{th} rigid mode. A systematic expansion of the exact body boundary condition about the equilibrium position of the body gives the following conditions for the decomposed velocity potential,

$$\nabla\phi_{SW} \cdot \mathbf{n} = \mathbf{U} \cdot \mathbf{n} \tag{2.29}$$

$$\nabla\phi_s \cdot \mathbf{n} = -\nabla\varphi \cdot \mathbf{n} \tag{2.30}$$

$$\nabla\phi_k \cdot \mathbf{n} = n_k\dot{x}_k + m_k x_k, \tag{2.31}$$

where, n_k is the k^{th} component of the generalized normal. The first term on the right-hand side of (2.31) is expected, and represents the velocity of the surface. Subtle implications of the expansion of the body boundary condition about its mean position give rise to the so-called m-terms, which Ogilvie [50] defines as

$$m_{1,2,3} = -(\mathbf{n} \cdot \nabla)\nabla\phi_B \tag{2.32}$$

$$m_{4,5,6} = -(\mathbf{n} \cdot \nabla)(\mathbf{n} \times \nabla\phi_B). \tag{2.33}$$

These hydro-geometric factors take into account two effects: the rotation of the body about its mean position, and the gradient of the steady flow field. Extending the Neumann-Kelvin assumptions to the body boundary simplifies the evaluation of these

coefficients. In this case, the m-terms reduce to

$$m_k = \{0, 0, 0, 0, Un_3, -Un_2\}. \tag{2.34}$$

The m-terms reveal the influence of the steady flow on the linearized oscillatory potential, and their introduction is due to the expansion of the body boundary condition about its mean position. In this thesis, we impose the body boundary condition without approximation and do not decompose the disturbance potential. Therefore, introduction of the m-terms is avoided, but of course the steady/unsteady coupling represented by these factors is implicit in the exact body boundary condition.

2.4 The boundary integral equation

Imposing the Neumann-Kelvin assumption at the free surface leads to following linear but time-varying initial boundary value problem in the global $OXYZ$ frame,

$$\nabla^2\Phi(\mathbf{X}, t) = 0 \quad \text{in} \quad \mathcal{V} \tag{2.35}$$

$$\Phi_{tt} + g\Phi_z = 0 \quad \text{on} \quad \mathrm{Z} = 0 \tag{2.36}$$

$$\nabla\Phi \cdot \mathbf{n} = (\mathbf{U} - \nabla\varphi) \cdot \mathbf{n} \quad \text{on} \quad \mathcal{B}(\mathrm{t}) \tag{2.37}$$

$$\nabla\Phi \rightarrow 0 \quad \text{at} \quad \mathcal{S}_\infty \tag{2.38}$$

$$\Phi = \Phi_t = 0 \quad \text{on} \quad \mathrm{Z} = 0,\ \mathrm{t} = 0. \tag{2.39}$$

Here, $\mathcal{V}$ is the fluid volume below the XY plane, and $\mathcal{S}_\infty$ and $\mathcal{B}(t)$ retain their previous definitions. We recast the boundary-value problem as an integral equation via Green's theorem in order to develop a problem that can be solved numerically.

The transient Green function satisfying the free-surface, far-field, radiation and initial conditions may be found in Wehausen and Latoine [56] or Stoker [53],

$$G(P, Q, t - \tau) = G^o(P, Q) + H(P, Q, t - \tau), \tag{2.40}$$

where the Rankine term is

$$G^o = \left(\frac{1}{r} - \frac{1}{r'}\right), \tag{2.41}$$

and

$$H = 2\int_0^\infty [1 - cos(\sqrt{gk}(t-\tau))]e^{k(z+\zeta)}J_o(kR)dk \tag{2.42}$$

is the wave part of the Green function.

Applying Green's Theorem to Φ and G produces the following boundary integral equation (see Appendix A),

$$2\pi\Phi + \iint_{\mathcal{B}(t)} \Phi G_n^o \, dS = \iint_{\mathcal{B}(t)} \Phi_n G^o \, dS + \int_0^t d\tau \iint_{\mathcal{B}(\tau)} (\Phi H_{\tau n} - \Phi_n H_\tau) \, dS \tag{2.43}$$
$$+\frac{1}{g}\int_0^t d\tau \int_{\Gamma(\tau)} (\Phi H_{\tau\tau} - \Phi_\tau H_\tau)\mathbf{U}_{2D} \cdot \mathbf{n}_{2D} \, dL,$$

where $\mathbf{U}_{2D}$ is the projection of the body velocity onto the XY plane. The two-dimensional unit normal in the XY plane is $\mathbf{n}_{2D}$, and Γ is the waterline.

The Rankine terms give rise to instantaneous effects, while all the memory effects of the wave flow are included by convolution. As discussed in the preceding section, traditional formulations linearize the body boundary condition about the mean position of the body. In these cases, the waterline term in (2.43) is only included if there is some gross forward-speed. In the body-exact context, we must include the waterline integral for any horizontal motion of finite-amplitude.

Our goal is to obtain a numerical solution of the above integral equation for three-dimensional geometries of arbitrary shape.

Chapter 3

The Numerical Solution

A new numerical scheme has been developed to solve the integral equation derived in Chapter 2. Previous investigators have solved the body-exact boundary-value problem using a collection of planar panels to represent the surface (Magee [34], Lin and Yue [29], and Huang [16]). Most assumed a piecewise constant distribution of the potential, although Huang used a bi-quadratic variation of the solution. The thesis of Maniar [36] demonstrates the efficiency and robustness of using B-spline basis functions in the solution of the linear frequency-domain problem. His restriction that the body surface also have a B-spline representation was recently lifted by Lee [24], who separated the discretization of the geometry and velocity potential. This thesis is aimed at applying such a *geometry-independent* method to the body-exact analysis in the time domain, where computational costs heighten the need for efficient algorithms.

The present method separates the hydrodynamic solution from the geometric modeling by superposing a grid onto a generic parametric representation of the surface. The complete body is comprised of a collection of patches, each with its own parameterization. The only restriction is that the mapping be regular. The parameterization of the geometric surface may take any form: non-uniform rational B-spline (NURBS), uniform and non-uniform B-splines, Bézier patches, analytic definitions, et cetera. The next step is to apply the discretized velocity potential over that portion of the surface that lies below the undisturbed free surface. The hydrodynamic solu-

tion is assumed to have a uniform and non-uniform B-spline representation. There is, however, no connection between the B-spline representation of the potential and the form of the geometric model. This separation of the geometric and hydrodynamic representation leads to a geometry-independent boundary element method.

Applying this approach to the body-exact initial-boundary-value problem introduces problems absent from typical lower-order panel methods. Most notable is the need to create a higher-order representation of the potential over the instantaneous wetted surface[1]. Essentially, this involves intersecting the body surface with the mean free surface, and mapping the B-spline discretization of the solution to the portion of the body that lies below $Z = 0$.

In addition to the overhead associated with redefining the time-varying surface, imposing the full body-boundary condition increases the numerical cost of solving the integral equation. In the body-exact formulation, convolution terms in the integral equation must be re-evaluated at every time step.

3.1 Trimming the master body

The body is comprised of a collection of patches, each of which has a parametric representation $\mathbf{X} = \mathbf{X}(u, v)$. This maps the unit square in the uv plane to some portion of the body surface. The first step in obtaining a numerical solution of the initial-boundary-value problem will be to properly define the instantaneous wetted surface. For patches that map to both wet and dry portions of the body surface, we perform two operations. First, a surface-surface intersection problem must be solved in order to find the instantaneous waterline. An interpolation scheme is then used to develop a mapping function from a square computational domain, the st space, to the wet portion of the uv plane. This intermediate mapping is not required on patches that lie completely below the free surface. In those cases, $(s, t) = (u, v)$.

[1] Because of the linear free-surface condition, we refer to the portion of the body below the $Z = 0$ plane as the *wetted surface*. The waterline is the curve on the body at $Z = 0$.

3.1.1 The marching algorithm

Assuming a regular surface, the geometry may be expressed locally as a polynomial in two parametric variables. The combination of an implicit algebraic surface (the mean free surface) with a regular parametric surface (the body surface) makes this intersection problem well suited for marching algorithms. These schemes are used to trace the two-dimensional curve in the uv plane that corresponds to the waterline. To make the intersection problem manageable, we will place some modest restrictions on the geometric parameterization. Self-intersecting waterlines are prohibited, and we assume the waterline curve crosses the boundaries of the relevant patch at exactly two points.

A bisection/Newton scheme is applied to the edges of the uv domain in order to initialize the marching algorithm. This search provides a point (u^*, v^*), such that $|Z(u^*, v^*)| < Z_{\text{tol}} = 10^{-6}$. The marching algorithm is schematically detailed in Figure 3-1, and combines differential properties of the geometry and the iterative Newton method.

Assume we prescribe a change in the u-coordinate, δu, and are searching for the appropriate change in v such that $Z(u^* + \delta u, v^* + \delta v) = 0$. The marching algorithm begins by expanding the surface about (u^*, v^*), with respect to u and v. Since $Z(u^*, v^*) \approx 0$, we are able to produce an estimate of δv in terms of δu, Z_u, and Z_v. $\tilde{v}$ is the initial guess of the waterline's v-coordinate, but since we only retain linear terms of the Taylor series, this point will not lie exactly at the mean free surface. An iterative method is needed to arrive at the correct variation in v. We begin each Newton iteration by expanding the surface in v about $(u^* + \delta u, \tilde{v})$. $Z(u^* + \delta u, \tilde{v})$ and $Z_v(u^* + \delta u, \tilde{v})$ give an improved estimate of $\tilde{v}$. This is repeated until the absolute value of $Z(u^* + \delta u, \tilde{v})$ is below Z_{tol}. Because of its quadratic convergence, the Newton scheme requires few iterations to arrive at the (numerically) true waterline.

At the end of a round of Newton iterations, we advance the waterline in the uv

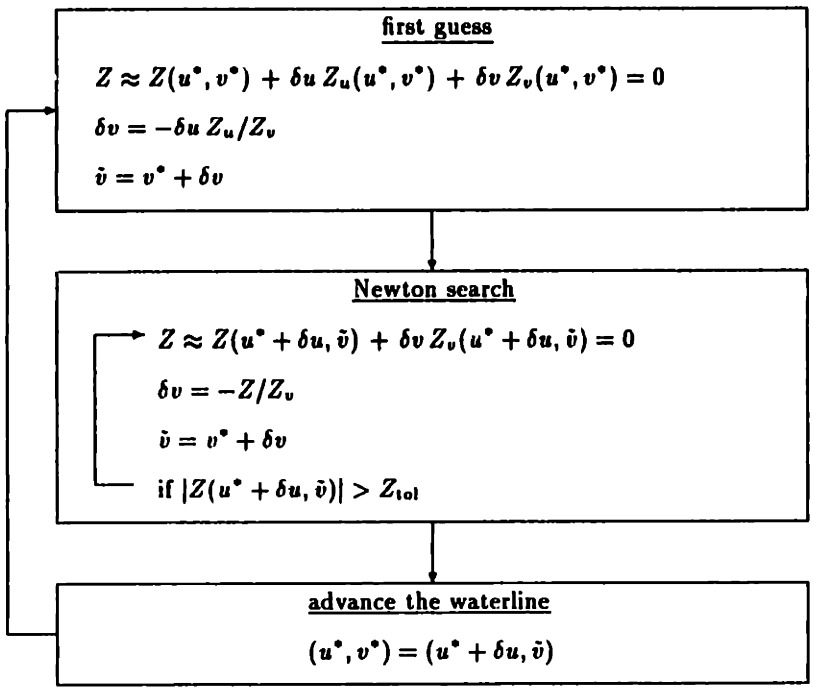

Figure 3-1: Flow chart of the marching algorithm.

plane. This new point is used to compute the next initial guess for another round of iterations. The tracing continues until we reach an edge of the uv square, which marks the end of the waterline on this patch. The shape of the two-dimensional curve generated by this marching scheme will depend on the instantaneous body position and the $\mathbf{X} = \mathbf{X}(u, v)$ parameterization of the surface. Figure 3-2 shows a typical waterline curve in the uv plane.

During the Newton search for δv, we must perform a division by Z_v. Likewise, Z_u appears in the denominator if δv is prescribed and δu is to be determined. The marching scheme implemented in this study chooses the search direction based on the relative magnitudes of these two derivatives. $Z_v(u^*, v^*)$ and $Z_u(u^*, v^*)$ are measured as the waterline curve is traced, and we search for δv if $|Z_v| \geq |Z_u|$, or for δu if $|Z_v| < |Z_u|$.

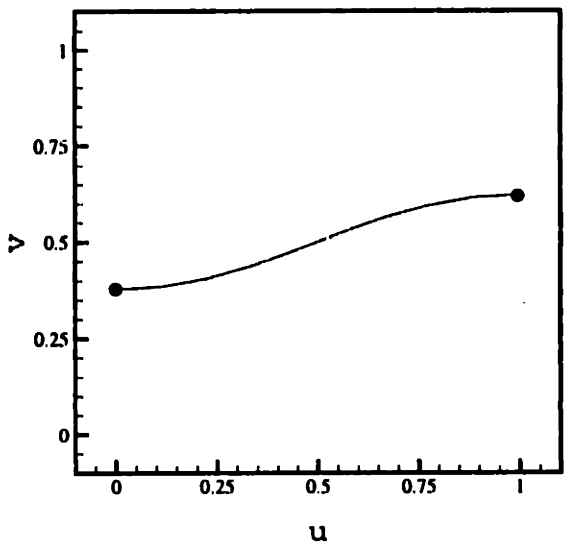

Figure 3-2: Typical waterline in the uv plane.

3.1.2 A square computational domain

In general, the wet portion of the uv square defined by the marching algorithm, $(u, v)_{\text{wet}}$, is non-rectangular. However, we wish to work in a square parametric domain in order to avoid complications with quadrature rules. We now derive a mapping function between the geometric uv plane and a new computational domain, the st unit square.

The idea of creating an interior surface from its boundary is credited to Gordon [12] and Coons [4]. The description of the Gordon-Coons interpolation scheme given below closely follows that of Hoschek [14].

A typical boundary of $(u, v)_{\text{wet}}$ consist of four curves, as shown in Figure 3-3. Each curve may be parameterized with respect to its arclength, in either s or t. We will interpolate between opposite boundaries using the following blending functions,

$$f_0(\chi) = (1 - \chi) \tag{3.1}$$

$$f_1(\chi) = \chi \tag{3.2}$$

where, $\chi = s$ or t. Although not implemented in this thesis, other Hermite poly-

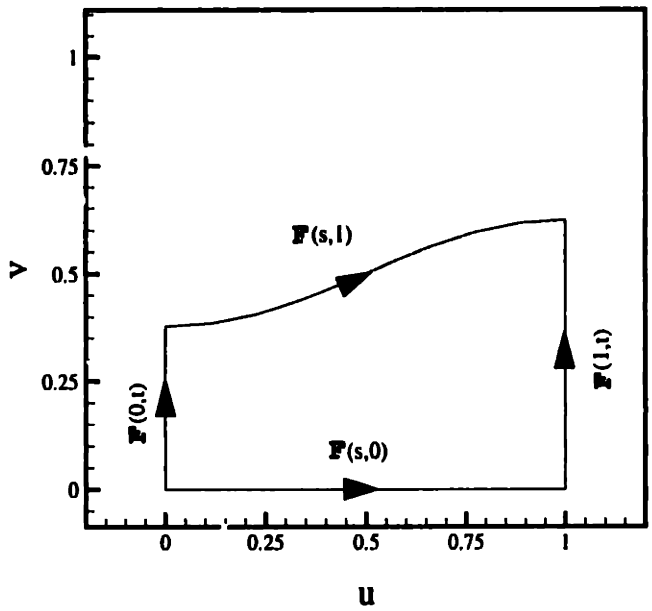

Figure 3-3: Boundary of a typical $(u, v)_{\text{wet}}$ space. $\mathbf{F}(s, 1)$ is the waterline.

nomials may be used to arrive at nonlinear interpolation schemes. However, linear blending functions will generate a mapping function adequate for our purposes.

The bi-linear Gordon-Coons scheme involves an interpolation and correction. Let $\mathbf{F}(s, t)$ be a function that maps points in the (s, t) unit square to points in $(u, v)_{\text{wet}}$. Suppose we interpolate between the lower and upper boundary curves, $\mathbf{F}(s, 0)$ and $\mathbf{F}(s, 1)$. B-spline representations of these two edges are obtained by a least-square fitting procedure, and parameterized by the s variable. The bottom curve lies at $t = 0$, and the top (waterline) boundary is the $t = 1$ isoparametric curve. To interpolate between these two curves, we apply the blending functions of (3.1) and (3.2). This gives

$$P_1\mathbf{F}(s, t) = (1 - t)\mathbf{F}(s, 0) + t\mathbf{F}(s, 1). \tag{3.3}$$

In the same manner, we interpolate between the left ($s = 0$) and right ($s = 1$)

bounding curves,

$$P_2\mathbf{F}(s,t) = (1-s)\mathbf{F}(0,t) + s\mathbf{F}(1,t). \tag{3.4}$$

In general, these linear interpolations by themselves are not exact. As an example, examine the error a linear interpolation introduces along the waterline. Unless $\mathbf{F}(s,1)$ is a straight line, the $P_2\mathbf{F}(s,t)$ interpolation introduces an error of

$$\mathbf{F} - P_2\mathbf{F} = \mathbf{F}(s,1) - [(1-s)\mathbf{F}(0,1) - s\mathbf{F}(1,1)]. \tag{3.5}$$

This correction should not only be applied at the upper boundary, but along all $t =$ constant curves defined by the $P_1\mathbf{F}$ interpolation. This may be symbolically written as

$$P_1(\mathbf{F} - P_2\mathbf{F}) = P_1\mathbf{F} - P_1P_2\mathbf{F}. \tag{3.6}$$

We obtain the correct $(u,v)_{\text{wet}}$ surface by interpolating in the s-direction and applying the appropriate correction. Adding (3.4) and (3.6),

$$\begin{aligned} \mathbf{F}(s,t) &= (u,v)_{\text{wet}} = P_2\mathbf{F} + P_1\mathbf{F} - P_1P_2\mathbf{F} \\ &= (1-t)\mathbf{F}(s,0) + t\mathbf{F}(s,1) + (1-s)\mathbf{F}(0,t) + s\mathbf{F}(1,t) \\ &- [(1-s)((1-t)\mathbf{F}(0,0) + t\mathbf{F}(0,1)) + s((1-t)\mathbf{F}(1,0) + t\mathbf{F}(1,1))]. \end{aligned} \tag{3.7}$$

Note that the Gordon-Coons interpolation reproduces the boundaries exactly. This ensures that the mapping excludes all dry portions of the body surface. Figure 3-4 shows isoparametric curves (with respect to s and t) generated by applying this bi-linear interpolation to the boundary shown in Figure 3-3, and illustrates the regular manner in which the $(u,v)_{\text{wet}}$ surface is partitioned.

Applying quadrature in the st plane will require the Jacobian of the Gordon-Coons interpolation. Since the bi-linear mapping is given explicitly by (3.7), and the B-spline representations of the boundary curves may be analytically differentiated, we may easily compute

$$J_{GC} = \frac{\partial(u,v)}{\partial(s,t)} = u_s v_t - u_t v_s, \tag{3.8}$$

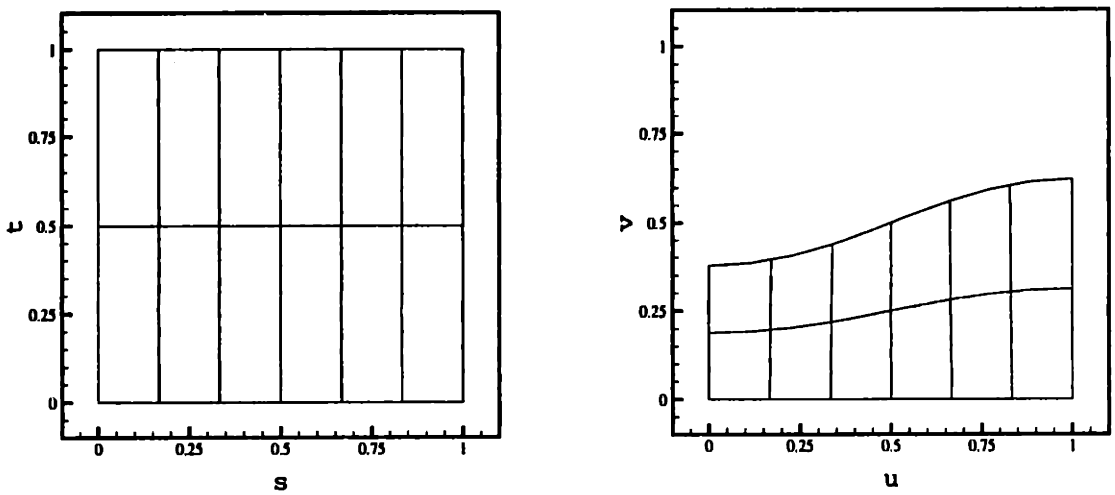

Figure 3-4: Isoparametric lines in the st and uv domains.

where, J_{GC} is the Jacobian of the $st \rightarrow uv$ transformation. Differentiating (3.7) gives

$$\mathbf{F}_s = (u,v)_s = (1-t)\mathbf{F}'(s,0) + t\mathbf{F}'(s,1) - s\mathbf{F}(0,t) + \mathbf{F}(1,t) \tag{3.9}$$
$$+s\left[(1-t)\mathbf{F}(0,0) + t\mathbf{F}(0,1)\right] - \left[(1-t)\mathbf{F}(1,0) + t\mathbf{F}(1,1)\right],$$

and

$$\mathbf{F}_t = (u,v)_t = -i\mathbf{F}(s,0) + \mathbf{F}(s,1) + (1-s)\mathbf{F}'(0,t) + s\mathbf{F}'(1,t) \tag{3.10}$$
$$-(1-s)\left[\mathbf{F}(0,1) - \mathbf{F}(0,0)\right] - s\left[\mathbf{F}(1,1) - \mathbf{F}(1,0)\right].$$

Subscripts denote partial differentiation, and primes indicate simple differentiation of the boundary curves. More details of the interpolation scheme are given in Appendix B.

3.2 The discrete integral equation

Identifying the portion of the body surface below $Z = 0$ and establishing a mapping function from the computational domain to the wetted surface are the first steps in solving the body-exact problem. We now turn our attention to the discretization of the hydrodynamic solution. Recent success with B-spline based panel codes has demonstrated the method's efficiency and robustness (Maniar [36], Nyvgaard and

Grue [48], Lee et. al. [25]), and we choose a higher-order discretization of the potential in the present thesis.

The solution of the velocity potential will require two rounds of integrations, each approximated by quadrature. First, quadrature is applied in order to evaluate the integral equation. This *inner* integration will require special care because of the singular behavior of the Green function. Next, the residual of the integral equation is minimized with respect to the B-spline basis functions directly in the parametric *st* space. Strictly speaking, this *outer* integration is a Petrov-Galerkin step since it involves test and trial functions that span different spaces.

3.2.1 A B-spline representation of the potential

As mentioned earlier, the velocity potential is represented by B-spline basis functions. This introduces higher-order panels, but we emphasize that these are only used in the description of the hydrodynamics. The geometric modeling is entirely separated from the hydrodynamic solution and supplied by the $\mathbf{X} = \mathbf{X}(u, v)$ parameterization.

The velocity potential over a patch is expressed as

$$\Phi(s,t) = \sum_{m=1}^{\mathcal{M}+k-1} \sum_{n=1}^{\mathcal{N}+k-1} \phi_{mn}\, \mathcal{S}(s)\, \mathcal{T}(t), \tag{3.11}$$

where, $\mathcal{S}$ and $\mathcal{T}$ are B-spline basis functions of order k, and $\mathcal{M}$ and $\mathcal{N}$ are the non-zero spans of the knot vectors in the s and t directions, respectively. We define a higher-order panel as the parametric space in the st plane between these spans. Therefore, the number of panels on a patch is $\mathcal{M} \times \mathcal{N}$. However, the total number of unknowns is $(\mathcal{M} + k - 1) \times (\mathcal{N} + k - 1)$ since k non-zero B-splines exist in each parametric direction at any point in the st unit square.

Figure 3-5 shows how the discretization of the velocity potential and the Gordon-Coons interpolation scheme combine to produce a hydrodynamic grid in Cartesian space. In this example, the body is comprised of two patches, each with $6 \times 2 = 12$ higher-order panels. The waterline of the body in its instantaneous position is found

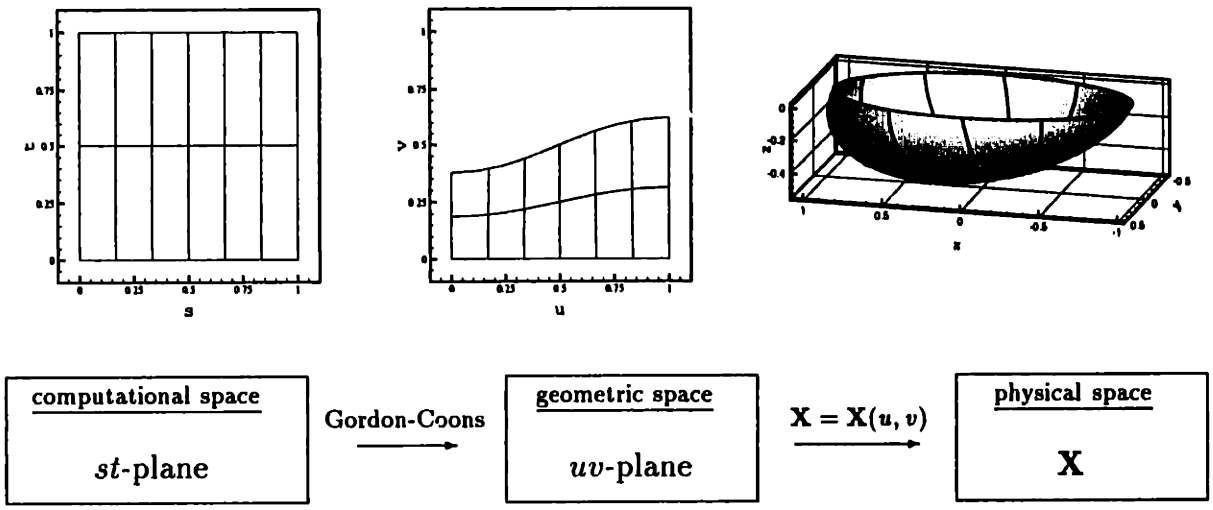

Figure 3-5: Higher-order panels, defined in the st square, are mapped into the uv and $\mathbf{X}$ domains. The lines are isoparametric curves at the B-spline knots.

by the marching algorithm described earlier, and (s,t) coordinates are mapped to the wet portion of the uv plane via the Gordon-Coons interpolation. The $\mathbf{X} = \mathbf{X}(u,v)$ geometric model then provides the transformation to Cartesian space. This treatment continues in a patchwise manner until the hydrodynamic grid is placed over the entire wetted surface.

The choice of B-spline order will determine the degree of continuity across panels. Basis functions of order k will produce a C^{k-2} continuous potential and fluid velocity of continuity C^{k-3}, giving a more physically reasonable description of the flow than the piecewise constant distribution of lower-order methods. Equally important is our ability to analytically differentiate the potential. This allows for accurate descriptions of the velocity field, which will be important in the evaluation of the complete Bernoulli pressure.

3.2.2 Quadrature schemes for the near- and far-fields

We now turn our attention to algorithms used to approximate the inner integration. The approach implemented in the present thesis follows that described by Maniar [36] and Lee [24], but the intermediate $(s,t) \rightarrow (u,v)$ mapping requires some modification.

Evaluating the Rankine terms of the integral equation requires special care due to their singularities when the field and source points coincide. Integrals of the wave components, however, are regular and may be computed by direct quadrature.

Substituting the B-spline representation of the potential into the integral equation, we obtain integrals of source and dipole moments of the form

$$SC_{ij} = \iint \mathcal{S}_i \mathcal{T}_j \frac{1}{R} dS = \iint \mathcal{S}_i \mathcal{T}_j \frac{1}{R} J \, ds \, dt, \tag{3.12}$$

and,

$$DP_{ij} = \iint \mathcal{S}_i \mathcal{T}_j \frac{\partial}{\partial n} \frac{1}{R} dS = \iint \mathcal{S}_i \mathcal{T}_j \frac{\partial}{\partial n} \frac{1}{R} J \, ds \, dt, \tag{3.13}$$

where J is the product of the Jacobians of the two transformations,

$$J = J_{uv} J_{GC} = \frac{\partial \vec{X}}{\partial(s,t)} = \frac{\partial \vec{X}}{\partial(u,v)} \frac{\partial(u,v)}{\partial(s,t)}. \tag{3.14}$$

In calculating the above integrals, conventional panel methods exploit the fact that the geometric representation is of a particular form. Most common is the constant-strength planar-panel method. There, Rankine terms may be exactly integrated over the quadrilaterals. The present thesis is less restrictive in its geometric assumptions. We only require that the parameterization $\mathbf{X} = \mathbf{X}(u,v)$ be regular. This allows for very accurate geometric models, but such a generic representation of the surface requires that the integral equation be approximated by numerical quadrature.

For any field point/panel combination, Rankine terms in the integral equation may be placed in one of three categories by measuring the characteristic length of the panel and its distance to the field point: the far-field, near-field, or self-influence. Figure 3-6 shows a typical field point/panel pair. We introduce the parameter α to measure the relative closeness of the field point to the panel, and define it as

$$\alpha \equiv \frac{D}{L}, \tag{3.15}$$

where, D is the distance from the field point to the parametric center of the panel, and L is the maximum distance from the center of the panel to its corners.

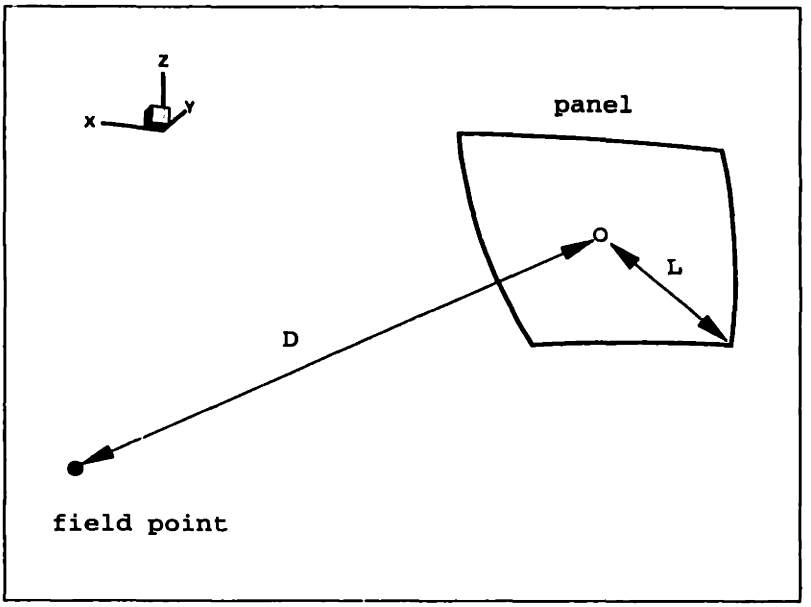

Figure 3-6: Typical field point/panel pair.

In the far-field, the field point and panel are separated by a large distance. There, $\alpha \geq \alpha_{\text{critical}}$, and the $\frac{1}{R}$ and $\frac{1}{R'}$ terms of the Green function are slowly varying. We apply Gauss-Legendre quadrature of fixed order to obtain approximations of SC_{ij} and DP_{ij}.

For small values of α, the field point lies close to the panel. In this near-field case $\alpha < \alpha_{\text{critical}}$, and we subdivide the panel in two. The Cartesian lengths of the panel are measured in both parametric directions, and we halve the panel along its longer side. This sub-division is applied adaptively until the characteristic length of a sub-panel gives $\alpha_{\text{sub-panel}} \geq \alpha_{\text{critical}}$. Quadrature is then applied over the sub-panels to evaluate the source and dipole moments.

As an example of near-field sub-division, we apply this scheme to the hemisphere shown in Figure 3-7. After the proper amount of adaptive sub-division, Gauss-Legendre quadrature is applied over the elements shown in Figure 3-8.

3.2.3 The self-influence panels

If the field point lies on the panel, care must be exercised since the Rankine terms are singular as $R \rightarrow 0$. Details of the self-influence evaluation scheme are given in

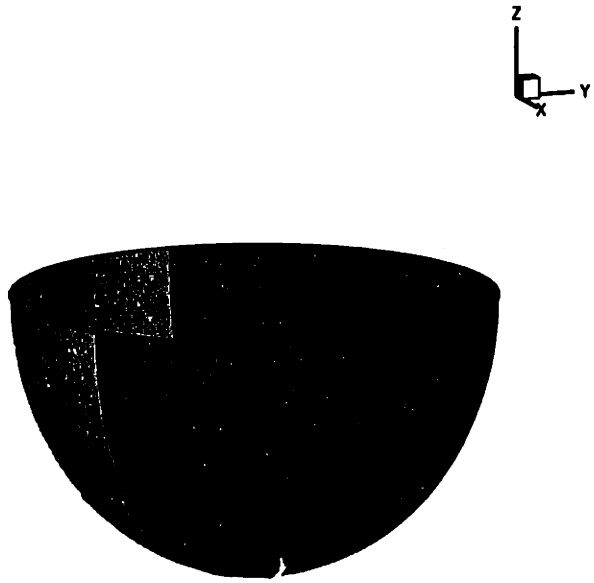

Figure 3-7: Hemisphere with $6 \times 2 = 12$ higher-order panels.

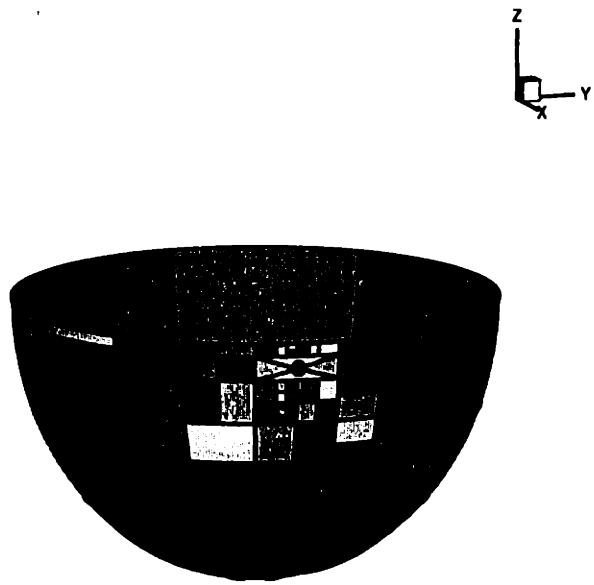

Figure 3-8: Adaptive subdivision applied to the near-field and self-influence panels of a hemisphere. The field point is the circle at the apex of the four self-influence triangles.

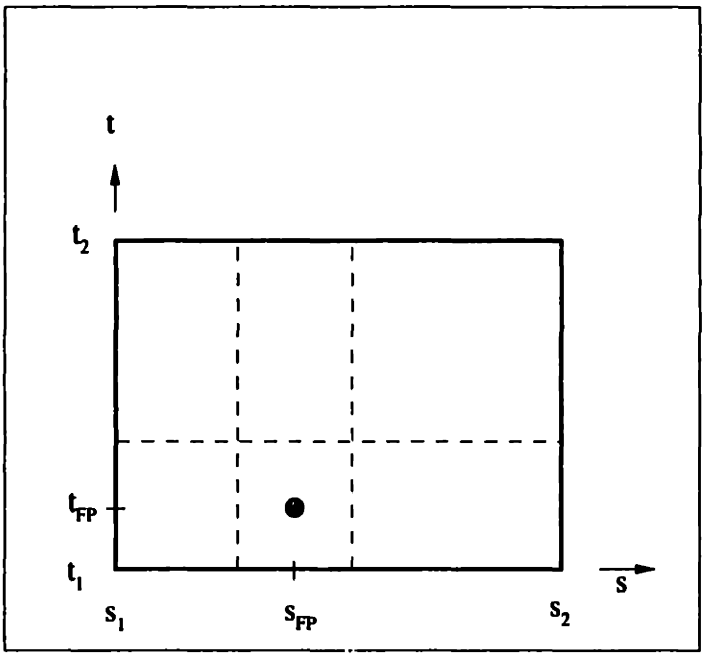

Figure 3-9: Division of the self-influence panel into one square and several rectangular sub-panels. The original panel has parametric dimensions $(s_1 : s_2, t_1 : t_2)$. (s_{FP}, t_{FP}) are the coordinates of the field point.

Appendix C, but we briefly summerize the method developed by Lee [24] below.

We begin our treatment of a self-influence panel by dividing it into sub-panels, one of which is a square centered about the parametric coordinates of the field point, (s_{FP}, t_{FP}), as shown in Figure 3-9. We will refer to the square with (s_{FP}, t_{FP}) as its center as the self-influence square. The Green function is non-singular over the remaining sub-panels, and the near-field algorithms described in § 3.2.2 may be applied. However, the Rankine terms are singular over the self-influence square and require special care.

We introduce the variables $(\bar{s}, \bar{t})$, which are normalized by the half-length of the square (σ) and centered at the field point. Four triangles are defined in the unit square upon which we apply a bi-quadratic transformation to analytically remove the singularity of the source term (Maniar [36]).

Contributions to the source and dipole moments from the self-influence square are defined as I. Noting that the B-spline basis functions have polynomial representation,

we may express I as a linear combination of terms,

$$I = \sum_{m=1}^{k} \sum_{n=1}^{k} I_{mn}(s - s_{\mathrm{FP}})^m (t - t_{\mathrm{FP}})^n. \tag{3.16}$$

After applying transformations to analytically remove the singularity (Lee [24]),

$$\begin{aligned} I_{mn} &= \sigma^2 p \int_{-1}^{1} \int_{-1}^{1} h_{m,n}(x, x(\alpha \sinh(pw+q)+\beta)) \frac{1}{|\mathbf{X}_v \cdot \mathbf{X}_v|} J \, dx dw \\ &+ \sigma^2 p' \int_{-1}^{1} \int_{-1}^{1} h_{m,n}(x(\alpha \sinh(p'w+q')+\beta'), x) \frac{1}{|\mathbf{X}_u \cdot \mathbf{X}_u|} J \, dx dw \end{aligned} \tag{3.17}$$

where

$$h_{m,n}(\bar{s}, \bar{t}) = (\sigma \bar{s} + s_{\mathrm{FP}})^{m-1} (\sigma \bar{t} + t_{\mathrm{FP}})^{n-1} \frac{\sqrt{e\bar{s}^2 + 2f\bar{s}\bar{t} + g\bar{t}^2}}{R} \tag{3.18}$$

for the source singularity, and

$$h_{m,n}(\bar{s}, \bar{t}) = (\sigma \bar{s} + s_{\mathrm{FP}})^{m-1} (\sigma \bar{t} + t_{\mathrm{FP}})^{n-1} \frac{\sqrt{e\bar{s}^2 + 2f\bar{s}\bar{t} + g\bar{t}^2}(\mathbf{R} \cdot \mathbf{n})}{R^3} \tag{3.19}$$

for the dipole singularity. e, f, and g are the first fundamental forms of the surface

$$e = \mathbf{X_u} \cdot \mathbf{X_u} \tag{3.20}$$

$$f = \mathbf{X_v} \cdot \mathbf{X_u} \tag{3.21}$$

$$g = \mathbf{X_v} \cdot \mathbf{X_v}. \tag{3.22}$$

The definitions of β, p and q are based on geometric quantities of the surface and given in Appendix C.

3.2.4 The convolution terms

The convolution terms of the integral equation do not contain any singularities because of the regular behavior of the wave part of the Green function. However, there are fast oscillations for nearby panel/field point pairs. These high spatial oscillations will dictate the order of Gauss-Legendre which is applied without sub-division or triangulation. In addition, an appropriate temporal discretization must be chosen in order to accurately convolve the spatially-integrated terms, which is approximated by trapezoidal integration.

3.3 Setup of the linear system

We have $\mathcal{M} \times \mathcal{N}$ higher-order panels over a patch, and k^2 B-spline coefficients on each panel. Therefore, the total number of unknowns is

$$N_u = \sum_{i=1}^{N_{\text{pat}}} (\mathcal{M}_i + k - 1) \times (\mathcal{N}_i + k - 1), \tag{3.23}$$

where N_{pat} is the number of patches. Collocation at centroids of planar panels in constant-strength lower-order methods always leads to an appropriately sized system of linear equations. Implementing such a scheme in the context of the present higher-order panel method is not straightforward. The placement of the collocation points will influence the numerical solution, and no optimal choice is obvious. As an alternative to collocation, we choose to produce a square system of linear equations by a Petrov-Galerkin procedure.

The integral equation is defined and evaluated in physical space, however its residual is minimized with respect to the B-splines directly in computational space. Therefore, the minimization step is

$$\iint r(\mathbf{X}, t)\, \mathcal{S}_i\, \mathcal{T}_j \, ds\, dt = 0, \tag{3.24}$$

where $r(\mathbf{X}, t)$ is the difference of the left- and right-hand sides of integral equation, and $\mathcal{S}_i$ and $\mathcal{T}_j$ are, respectively, the B-spline basis functions in the s and t directions. Since there are as many distinct splines as unknown coefficients, we arrive at a square system of linear equations for the B-spline coefficients of the potential. After the residual is evaluated, the outer integration of (3.24) is imposed by another round of Gauss-Legendre quadrature.

3.4 Computational efficiency of the higher-order method

The geometry-independent higher-order method described in the preceding sections has been implemented in the computer program `HITIM`. We may measure its efficiency

by comparing results from the present method to numerical solutions obtained from a code based on the constant-strength planar-panel approach.

Consider a hemisphere of unit radius floating in calm water. The body is held in its equilibrium position and given unit amplitude velocity in the vertical direction at $t = 0^+$. The heave-heave impulse response function is then computed using HITIM and the lower-order code TIMIT. Planar-panel and higher-order discretizations of the hemisphere are shown, respectively, in Figures 3-10 and 3-11. In the geometry-independent discretizations, B-splines are distributed over an analytically defined surface. The sizes of the resulting linear systems of equations are given in Table 3.1.

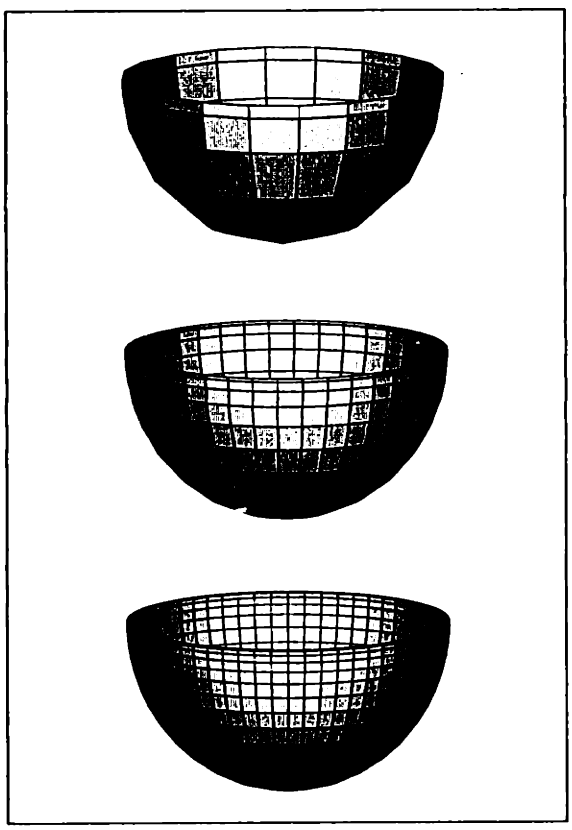

Figure 3-10: Lower-order discretizations used in TIMIT include 10x10, 20x20, and 30x30 planar panels over the hemisphere.

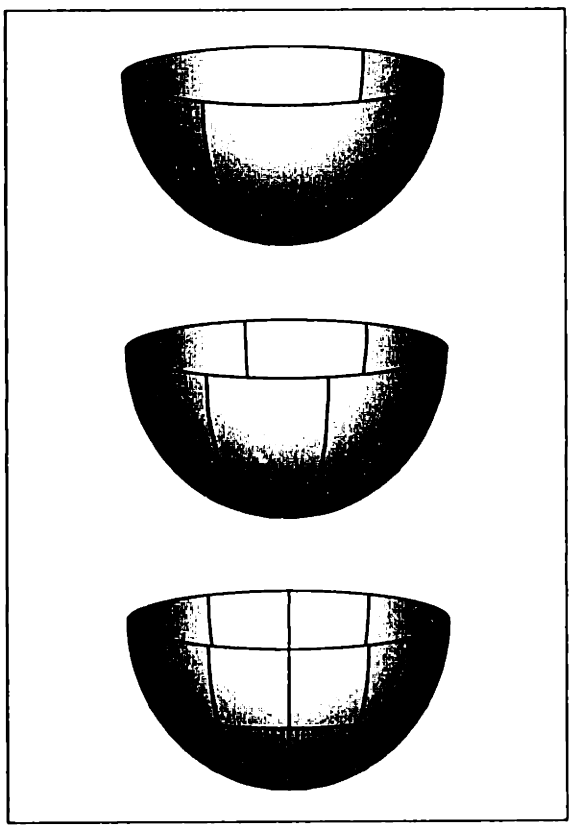

Figure 3-11: Higher-order discretizations used in HITIM include 2x2, 4x4, and 6x6 higher-order panels over the analytic hemisphere.

Computations of the heave-heave impulse response from TIMIT are shown in Figure 3-12. The same quantity is evaluated by HITIM using cubic B-splines ($k = 4$), and plotted in Figure 3-13. Comparing the impulse response function near its peak value,

Number of Unknowns						
code	# of panels	N_u	code	# of panels	order	N_u
TIMIT	10x10	100	HITIM	2x2	$k = 4$	25
	20x20	400		4x4	$k = 4$	49
	30x30	900		6x6	$k = 4$	81

Table 3.1: The number of unknowns in the linear system of equations using the lower- (TIMIT) and higher-order (HITIM) panel methods.

one may see that a converged result is obtained by the higher-order method using relatively few unknowns. Oscillations in the tail of the impulse response functions are due to irregular frequency effects, and may be mitigated by refined discretizations.

The errors in the peak values of the computed impulse response functions are plotted in Figure 3-14. One immediately sees that the higher-order method requires fewer unknowns to acheive results of a particular accurcay, and that the method converges more quickly than the constant-strentgh planar-panel approach. Runtimes associated with the lower- and higher-order computations are plotted in Figure 3-15.

The rate of convergence of a numerical method has important consequences with respect its efficiency. This is mostly clearly demonstrated by plotting the error against CPU time and required memory. For an absolute error of 10^{-3}, Figure 3-16 shows that the higher-order method uses approximately ten times fewer CPU minutes than the lower-order approach. Savings are also observed with regard to memory requirements, as seen in Figure 3-17. In the computation of the impulse response function, the higher-order method uses approximately half of the memory required of the lower-order method to achieve an absolute error of 10^{-3}. The difference in memory requirements is greater for more accurate solutions.

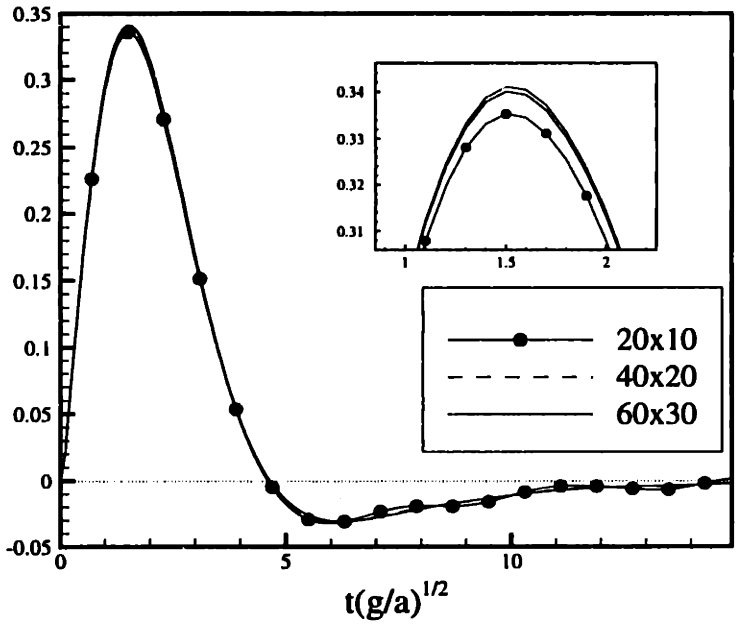

Figure 3-12: The heave-heave impulse response function of the floating hemisphere computed by `TIMIT`.

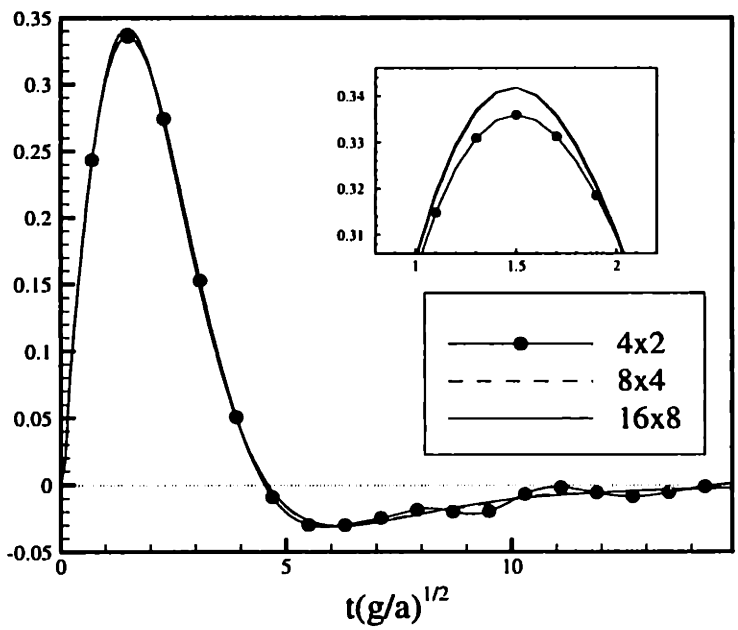

Figure 3-13: The heave-heave impulse response function of the floating hemisphere computed by `HITIM`.

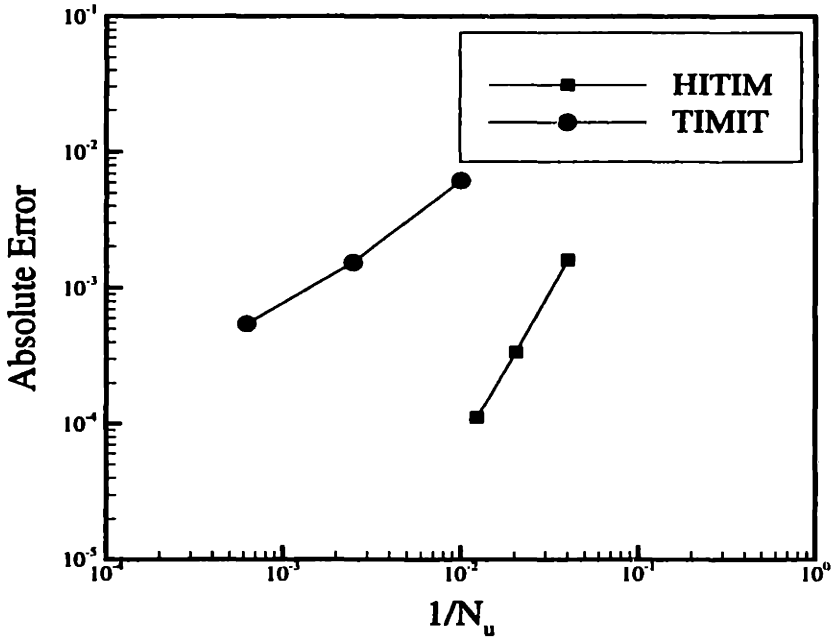

Figure 3-14: Convergence rates of the peak value of the heave-heave impulse response function using the constant-strength planar-panel and geometry-independent higher-order methods. Reference point is data from a 8×8 ($k = 4$) higher-order computation.

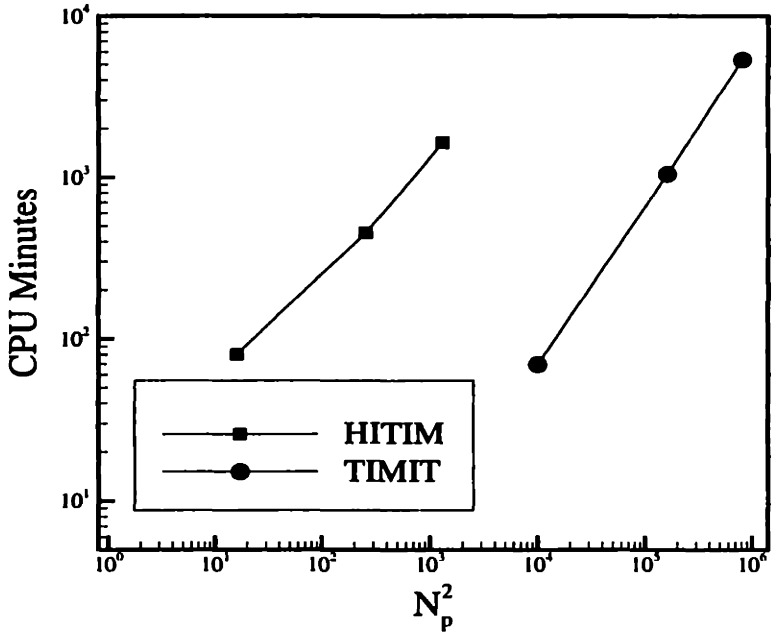

Figure 3-15: Computational effort of the constant-strength planar-panel and geometry-independent higher-order methods. N_{pan} is the number of panels. Computations were performed on a low-level DEC α workstation.

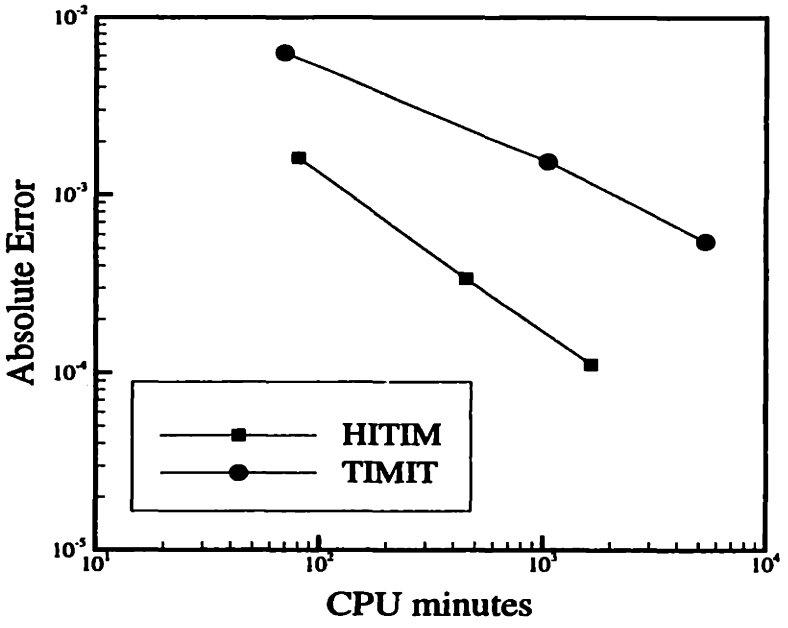

Figure 3-16: Error in the peak value of the impulse response function versus CPU time using constant-strength planar-panel and geometry-independent higher-order methods.

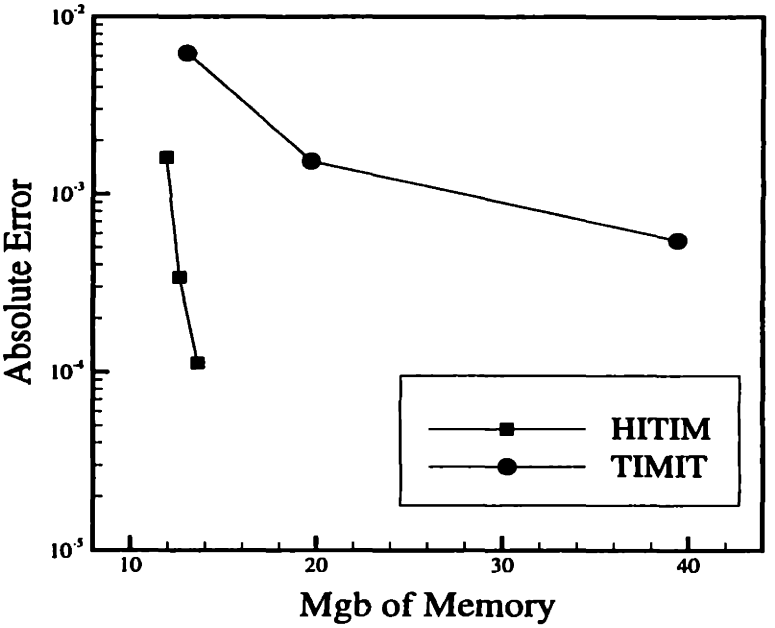

Figure 3-17: Error in the peak value of the impulse response function versus required memory using constant-strength planar-panel and geometry-independent higher-order methods.

Chapter 4

Global forces & Rigid-body Mechanics

In the present formulation, the hydrodynamic flow and rigid-body dynamics are coupled through the body boundary condition. For freely floating bodies, the equations of rigid-body motion are essentially a dynamic boundary condition. The fact that we impose the body boundary condition exactly means that the hydrodynamic and rigid-body problems must be solve simultaneously. In the preceding chapters, we were only concerned with obtaining a solution of the hydrodynamic flow. We now examine the rigid-body mechanics, and its coupling to the velocity potential through the hydrodynamic forces.

4.1 The hydrodynamic force

At each instant in time, the fluid pressure is integrated over the hull to obtain the global hydrodynamic forces. These wave loads will determine the subsequent motion of the body, in accordance with Newton's Law. Therefore, an accurate and complete description of the pressure is essential in properly simulating the response of a body. The bulk of the global hydrodynamic load may be obtained by integrating the linear Bernoulli pressure over that portion of the body that lies below the undisturbed mean free surface. However, important small-amplitude contributions to the global force come from the quadratic Bernoulli term and by accounting for the relative wave

runnup about the body.

The evaluation of the wave-induced forces may be separated into two terms: the integration of fluid pressure up to the mean free surface, and pressure integration from the undisturbed free surface to the actual wave elevation. Assuming the fluid velocity is of magnitude $O(\epsilon)$, where $\epsilon \ll 1$, the global hydrodynamic force, correct to $O(\epsilon^2)$, is

$$\mathbf{F} = -\rho \iint_{\mathcal{B}(t)} \left(\Psi_t + \frac{1}{2}V^2 + gZ\right) \mathbf{n} dS - \rho \iint_{\Delta\mathcal{B}(t)} (\Psi_t + gZ)\, \mathbf{n} dS \,, \tag{4.1}$$

where $V = |\nabla\Psi|$ is the magnitude of the total fluid velocity, subscripts denote partial differentiation in an inertial frame, $\mathcal{B}(t)$ is the body surface below $Z = 0$, and $\Delta\mathcal{B}(t)$ is the body surface between $Z = 0$ and the free-surface elevation ζ. The integral over $\Delta\mathcal{B}(t)$ may reduced to

$$\begin{aligned} -\rho \iint_{\Delta\mathcal{B}(t)} (\Psi_t + gZ)\, \mathbf{n} dS &= -\rho \int_{\Gamma(t)} dL \int_o^{\zeta} (\Psi_t + gZ)\, \mathbf{n} dz & (4.2) \\ &= \frac{\rho g}{2} \int_{\Gamma(t)} \zeta^2 \mathbf{n} dL \,, & (4.3) \end{aligned}$$

where the integrand of the inner integral in (4.2) has been expanded about $Z = 0$, and the first-order wave elevation $\zeta = -\frac{1}{g}\Psi_t$ has been used. The hydrodynamic force may then be expressed as

$$\mathbf{F} = -\rho \iint_{\mathcal{B}(t)} \left(\Psi_t + \frac{1}{2}V^2 + gZ\right) \mathbf{n} dS + \frac{\rho g}{2} \int_{\Gamma(t)} \zeta^2 \mathbf{n} dL \,. \tag{4.4}$$

Although we have not formulated a series of boundary value problems by perturbation expansion, the quadratic terms in (4.4) may be loosely thought of as contributions to the second-order force from the first-order solution. These give rise to mean, difference- and sum-frequency components of the force, but are not the only sources of nonlinearity. The potential itself may have, for example, a slowly-varying component since the solution of the initial boundary-value problem and the pressure integration are defined over a surface that oscillates in time.

4.1.1 Evaluating the V^2 term

A major benefit in representing the potential with B-splines is our ability to analytically differentiate the solution. This allows for the evaluation of the fluid velocity over the body surface without the errors associated with finite difference techniques.

The fluid velocity due to the body potential is found by combining terms tangential and normal to the body surface.

$$\nabla\Phi = \Phi_n \mathbf{n} + \nabla_S \Phi, \tag{4.5}$$

where ∇_S is the gradient operator tangential to the body surface, and the normal flow, $\Phi_n \mathbf{n}$, is known from the body boundary condition. We have solved for the potential over the body surface, so its gradients give the tangential fluid velocity,

$$\nabla_S \Phi = \frac{1}{eg - f^2}[\mathbf{X}_u(g\Phi_u - f\Phi_v) + \mathbf{X}_v(e\Phi_v - f\Phi_u)]\,, \tag{4.6}$$

where, e, f and g are the first fundamental forms of the surface and are computed from the gradients $\mathbf{X}_u$ and $\mathbf{X}_v$. Since the potential is defined in the st plane, we must invert the Jacobian of the Gordon-Coons transformation in order to obtain its derivatives in the u and v directions,

$$\left\{ \begin{array}{c} \Phi_u \\ \Phi_v \end{array} \right\} = [J_{GC}]^{-1} \left\{ \begin{array}{c} \Phi_s \\ \Phi_t \end{array} \right\} = \left[\begin{array}{cc} \frac{\partial s}{\partial u} & \frac{\partial t}{\partial u} \\ \frac{\partial s}{\partial v} & \frac{\partial t}{\partial v} \end{array} \right] \left\{ \begin{array}{c} \Phi_s \\ \Phi_t \end{array} \right\}. \tag{4.7}$$

The total velocity potential is a linear combination of the incident and disturbance potentials. Therefore, the fluid velocity is simply

$$\mathbf{V} = \nabla\Psi = \nabla\varphi + \nabla\Phi. \tag{4.8}$$

Gradients of the linear incident potential are known exactly, and $[J_{GC}]^{-1}$ may be explicitly computed from the $st \rightarrow uv$ mapping given in § 3.1.2. Therefore, the errors in calculating the fluid velocity from the potential are only associated with the geometric quantities. These may be minimized by an accurate parameterization of the body, or eliminated completely by an analytic definition of the surface.

4.1.2 Approximating the time derivative of the solution

The linear Bernoulli term requires the derivative of the potential with respect to time, but we have only solved for the potential up to the present instant. Therefore, backward difference techniques are used to approximate Φ_t. The body on which we obtain a solution is moving at speed $\mathbf{U}$, and the position of the panel on the surface is changing in time. Therefore, two applications of the chain rule are needed to evaluate the temporal derivative of the potential,

$$\frac{\partial \Phi}{\partial t} = \frac{d\Phi}{dt} - \mathbf{U} \cdot \nabla \Phi - \{u_t, v_t\} \cdot \{\Phi_u, \Phi_v\}. \tag{4.9}$$

A three-point backward difference scheme approximates the total derivative, $\frac{d\Phi}{dt}$. The panel velocity, $\{u_t, v_t\}$, is found by examining the Gordon-Coons mapping functions of two consecutive body positions. Once the time rate of change of the body potential is computed, it is added to the linear incident pressure to give

$$\Psi_t = \Phi_t + \varphi_t. \tag{4.10}$$

4.2 Rigid-body mechanics

Once the hydrodynamic loads are computed, we may find the resulting body motion using the equations of rigid-body mechanics. These ordinary differential equations are derived by applying the conservation laws of linear and angular momentum. Conventional schemes are then used to numerically integrate the matrix form of the equations of motion. A new solution of the hydrodynamic problem is required at each of these sub-steps, since the body boundary condition is imposed exactly.

4.2.1 Working with rotating reference frames

The equations governing rigid-body motion are derived by applying Newton's Second Law in an inertial reference frame, but we introduce a body-fixed coordinate system in order to conveniently describe the mass distribution of the body. The distinc-

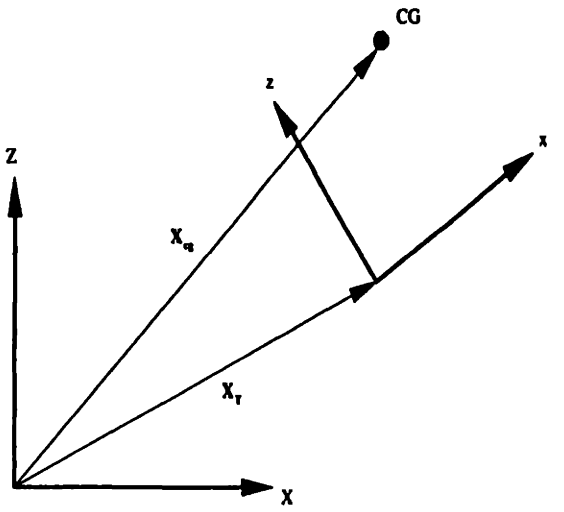

Figure 4-1: Two-dimensional view of body- and earth-fixed frames. Position vectors to the center of gravity and origin of the body-fixed frame.

tion between these two frames is non-negligible because of the finite-amplitude body motions.

Any two reference frames may be related by three translations and a set of Euler angles (see Figure 4-1). $\mathbf{X}_T$ is a position vector from the origin of the $OXYZ$ frame to the origin of the body-fixed coordinate system, and $\mathbf{X}_R$ is the set of Euler angles defining the rotation of the body,

$$\mathbf{X}_T = \begin{Bmatrix} X \\ Y \\ Z \end{Bmatrix} \quad \text{and} \quad \mathbf{X}_R = \begin{Bmatrix} \alpha \\ \beta \\ \gamma \end{Bmatrix}. \tag{4.11}$$

Let $\hat{\mathbf{X}}$ [1] be a position vector in the $oxyz$ coordinate system. Its representations in the earth- and body-fixed frames are related by

$$\hat{\mathbf{X}} = [D](\mathbf{X} - \mathbf{X}_T) \tag{4.12}$$

$$\mathbf{X} = \mathbf{X}_T + [D]^T\hat{\mathbf{X}}, \tag{4.13}$$

where $[D]$ is the rotational transformation matrix, which depends on the order of the

[1] Quantities with hats denote representations in the body-fixed coordinate system

rotation. Assuming we prescribe the sequences as yaw(γ) $\rightarrow$ pitch(β) $\rightarrow$ roll(α), the transformation matrix is

$$[\mathrm{D}] = \begin{bmatrix} \mathrm{c}\gamma\ \mathrm{c}\beta & s\gamma\ c\beta & -s\beta \\ -\mathrm{s}\gamma\ \mathrm{c}\alpha + \mathrm{c}\gamma\ \mathrm{s}\alpha\ \mathrm{s}\beta & c\gamma\ c\alpha + s\alpha\ s\beta\ s\gamma & s\alpha\ c\beta \\ \mathrm{s}\gamma\ \mathrm{s}\alpha + \mathrm{c}\gamma\ \mathrm{c}\alpha\ \mathrm{s}\beta & -c\gamma\ s\alpha + s\gamma\ s\beta\ c\alpha & c\beta\ c\alpha \end{bmatrix}, \tag{4.14}$$

where we have used the shorthand notation

$$\begin{aligned} \mathrm{c}\alpha &= \cos(\alpha) \quad & \mathrm{s}\alpha &= \sin(\alpha) \\ \mathrm{c}\beta &= \cos(\beta) \quad & \mathrm{s}\beta &= \sin(\beta) \\ \mathrm{c}\gamma &= \cos(\gamma) \quad & \mathrm{s}\gamma &= \sin(\gamma). \end{aligned}$$

Since this is an ortho-normal transformation, $[D]^{-1} = [D]^T$. For small Euler angles, the rotational transformation matrix reduces to the identity matrix.

Angular velocity resolved into the body frame becomes

$$\hat{\omega} = \begin{Bmatrix} -\dot{\gamma}\ \mathrm{s}\beta + \dot{\alpha} \\ \dot{\gamma}\ \mathrm{s}\alpha\ \mathrm{c}\beta + \dot{\beta}\ \mathrm{c}\alpha \\ \dot{\gamma}\ \mathrm{c}\alpha\ \mathrm{c}\beta + \dot{\beta}\ \mathrm{s}\alpha \end{Bmatrix}, \tag{4.15}$$

where, the overdot denotes temporal differentiation. Thus, the time rate change of the Euler angles may be related to angular velocity by

$$\dot{\mathbf{X}}_R = [W]\hat{\omega} = \begin{bmatrix} 1 & \mathrm{s}\alpha\ \mathrm{s}\beta/\mathrm{c}\beta & \mathrm{c}\alpha\ \mathrm{s}\beta/\mathrm{c}\beta \\ 0 & \mathrm{c}\alpha & -\mathrm{s}\alpha \\ 0 & \mathrm{s}\alpha/\mathrm{c}\beta & \mathrm{c}\alpha/\mathrm{c}\beta \end{bmatrix} \hat{\omega}. \tag{4.16}$$

Like the rotational transformation matrix, $[W]$ reduces to the identity matrix for small angular displacements.

4.2.2 The equations of rigid-body motion

Applying the conservation laws of linear and angular momentum at the center of gravity will lead to the equations governing three-dimensional translation and rotation

of a rigid body. The only complication comes from the fact that the mass distribution is most conveniently defined in the body-fixed reference frame. Therefore, the moment equation must first be stated in the earth-fixed frame, and then transferred to the non-inertial body-fixed frame. The derivation given below closely follows that of Ogilvie [50].

The conservation of linear momentum requires that Newton's second law be applied at the center of gravity. The acceleration of this point may be expressed relative to the motion of the origin of the body-fixed coordinate system,

$$\frac{\partial^2 \mathbf{X}_{cg}}{\partial t^2} = \frac{\partial^2 \mathbf{X}_T}{\partial t^2} + \frac{\partial \omega}{\partial t} \times \mathbf{R}_{cg} + \omega \times (\omega \times \mathbf{R}_{cg}), \tag{4.17}$$

where $\mathbf{R}_{cg} = \mathbf{X}_{cg} - \mathbf{X}_T$. The force is then related to the translational motion by treating the body as a point mass,

$$\mathbf{F} = m \left(\frac{\partial^2 \mathbf{X}_T}{\partial t^2} + \frac{\partial \omega}{\partial t} \times \mathbf{R}_{cg} + \omega \times (\omega \times \mathbf{R}_{cg}) \right). \tag{4.18}$$

The conservation of angular momentum applied at the center of gravity is

$$\mathbf{M}_{cg} = \frac{\partial \mathbf{H}}{\partial t}, \tag{4.19}$$

where $\mathbf{M}_{cg}$ is the moment about the center of gravity, and $\mathbf{H}$ is the angular momentum of the body. The moment is commonly determined with respect to a body-fixed origin. Therefore, the left-hand side of the above equation is replaced by

$$\mathbf{M}_{cg} = \mathbf{M}_{\mathbf{o}} - \mathbf{R}_{cg} \times \mathbf{F}. \tag{4.20}$$

Angular momentum is a vector quantity and therefore remains invariant if the body frame is selected. Only its representation will differ according to the transformation rule,

$$\hat{\mathbf{H}} = [D]\mathbf{H}. \tag{4.21}$$

Since $\hat{\mathbf{H}}$ is measured in an accelerating coordinate system, its time rate of change is

$$\dot{\hat{\mathbf{H}}} = [I_{cg}]\dot{\hat{\omega}} + \hat{\omega} \times [I_{cg}]\hat{\omega}, \tag{4.22}$$

where $[I]_{cg}$ is the inertia tensor of the body describing its distribution of mass about the center of gravity, defined with respect to the body-fixed frame.

Substituting (4.20) and (4.22) into (4.19) gives the following vector-valued equation governing rotational motion of the body,

$$[D](\mathbf{M_o} - \mathbf{R}_{cg} \times \mathbf{F}) = [I_{cg}]\dot{\hat{\omega}} + \hat{\omega} \times [I_{cg}]\hat{\omega} \tag{4.23}$$

$$\hat{\mathbf{M}}_\mathbf{o} - \hat{\mathbf{R}}_{cg} \times [D]\mathbf{F} = [I_{cg}]\dot{\hat{\omega}} + \hat{\omega} \times [I_{cg}]\hat{\omega} \tag{4.24}$$

4.2.3 Integrating the equations of motion

A system of equations governing the six rigid degrees of freedom may be derived by combining the equations governing translational and rotational motion. Retaining terms linear in ω, we arrive at

$$\begin{bmatrix} [m] & -m\mathbf{R}_{cg} \times [D]^T \\ m\hat{\mathbf{R}}_{cg} \times [D] & [I_o] \end{bmatrix}_{6\times6} \begin{Bmatrix} \ddot{\mathbf{X}}_T \\ \dot{\hat{\omega}} \end{Bmatrix} = \begin{Bmatrix} \mathbf{F} \\ \hat{\mathbf{M}}_o \end{Bmatrix}. \tag{4.25}$$

Here, $[m]$ is the 3×3 matrix with the body mass along its main diagonal and zero everywhere else. $[I_o]$ is the inertia tensor with respect to the body origin. The vector-matrix cross-product used to assemble the 6×6 matrix in (4.25) is defined in Appendix D.

Denoting the above 6×6 matrix as [M], we may cast these six second-order differential equations into a set of twelve first-order equations. From (4.16), the equations of motion become

$$\frac{\partial}{\partial t} \begin{Bmatrix} \dot{\mathbf{X}}_T \\ \hat{\omega} \\ \mathbf{X}_T \\ \mathbf{X}_R \end{Bmatrix} = \begin{Bmatrix} [M]^{-1} \begin{Bmatrix} \mathbf{F} \\ \hat{\mathbf{M}}_\mathbf{o} \end{Bmatrix} \\ \cdots \\ \dot{\mathbf{X}}_T \\ [W]\hat{\omega} \end{Bmatrix}. \tag{4.26}$$

This may be symbolically written as

$$\dot{\mathbf{y}} = \mathbf{f}(\mathbf{y}, t)\,, \tag{4.27}$$

Runge-Kutta Rules	
2^{nd}-order	$\mathbf{y}_{n+1} = \mathbf{y}_n + \Delta t\, \mathbf{k}_2$
3^{rd}-order	$\mathbf{y}_{n+1} = \mathbf{y}_n + \frac{\Delta t}{6}(\mathbf{k}_1 + 4\mathbf{k}_2 + \mathbf{k}_3)$
intermediate steps	$\mathbf{k}_1 = \mathbf{f}(\mathbf{y}_n)$
	$\mathbf{k}_2 = \mathbf{f}(\mathbf{y}_n + \frac{\Delta t}{2}\mathbf{k}_1)$
	$\mathbf{k}_3 = \mathbf{f}(\mathbf{y}_n + \Delta t(2\mathbf{k}_2 - \mathbf{k}_1))$

Table 4.1: Rules for 2^{nd}- and 3^{rd}-order Runge-Kutta integration. $\mathbf{y}$ and $\mathbf{k}_i$ are, respectively, the left and right side of (4.27). At any instant in time, $t = n\Delta t$

and integrated by standard numerical schemes. We choose the family of Runge-Kutta schemes for the cases in this thesis since they offer substantial stability. Free motion simulations presented in this thesis are obtained from either the 2^{nd}- or 3^{rd}-order schemes shown in Table 4.1.

Chapter 5

Submarine Near the Free Surface

Although the dominant wave loads on a body oscillate at the frequency of the incident waves, mean and low-frequency forces due to second-order effects are important in some practical cases. One such example is the quadratic interaction of the first-order potential that induces large horizontal excursions of moored vessels and tension leg platforms. Fortunately, the mean horizontal forces and vertical moment may be efficiently evaluated by methods based on momentum conservation (Maruo [37], Newman [43]), and computationally intensive pressure integration may be avoided. Components of the drift force and moment in the vertical and horizontal directions, respectively, are of importance to unrestrained submerged vessels or floating bodies with small waterplane areas. Unlike the horizontal drift forces and vertical moment, these quantities are usually computed by direct pressure integration.

The existence of a vertical drift force on submerged bodies has been known for some time and has been the subject of previous studies. The zero-speed three-dimensional solution of C.-H. Lee and Newman [26] showed that in addition to the mean vertical force, second-order effects produce a nonzero mean trim moment on a spheroid submerged just below the free surface. Computations from the spectral method of Liu [31] indicated that the asymmetry of higher-order corrections to the distribution of the mean vertical force along the length are important as the incident waves steepen. The mean forces on a moving body beneath incident waves has been investigated by

Musker [38], Wilmott [57], and Bingham et. al. [3], among others. The numerical methods of [38] and [3] are suitable for general body shapes, while the method of matched asymptotic expansions of [57] was used to calculate the flow about slender axisymmetric body. The above studies assumed either small body motions about a prescribed depth or no body oscillations at all.

In this chapter, we use the body-exact formulation to examine the mean vertical force and trim moment acting on a submarine as the vessel performs a near-surface maneuver. The effect of small-amplitude oscillations is examined by allowing the submarine to respond to waves while undergoing large-amplitude motions.

5.1 The analytic geometry

For the purpose of this study, we define the surface of the submarine using an axisymmetric form defined by Jackson [17]. The geometric model consists of a parabolic nose, parallel middle body, and tapered stern. The surface is a body of revolution, and its local radius is a function of position forward (x_f) or aft (x_a) of the parallel middle body,

$$r_f = r_{pmb}\left[1-\left(\frac{x_f}{L_f}\right)^2\right]^{1/2} \tag{5.1}$$

$$r_a = r_{pmb}\left[1-\left(\frac{x_a}{L_a}\right)^3\right], \tag{5.2}$$

where the parallel middle body has a radius r_{pmb}, and $x_{f,a}$ are local coordinates running from zero at the parallel middle body to L_f or L_a. The geometry used in this thesis has the following dimensions: $r_{pmb} = \frac{33}{720}$, $L_f = \frac{60}{360}$, and $L_a = \frac{140}{360}$. Since our model does not include appendages, we cannot capture the flow about the sail or fins. However, wave interactions with the bare hull should produce the main contribution to the hydrodynamic loads on the body and reveal general trends in the mean forces.

Three of the discretizations used to demonstrate the spatial convergence of HITIM results are shown in Figure 5-1. When possible, results from the present method are

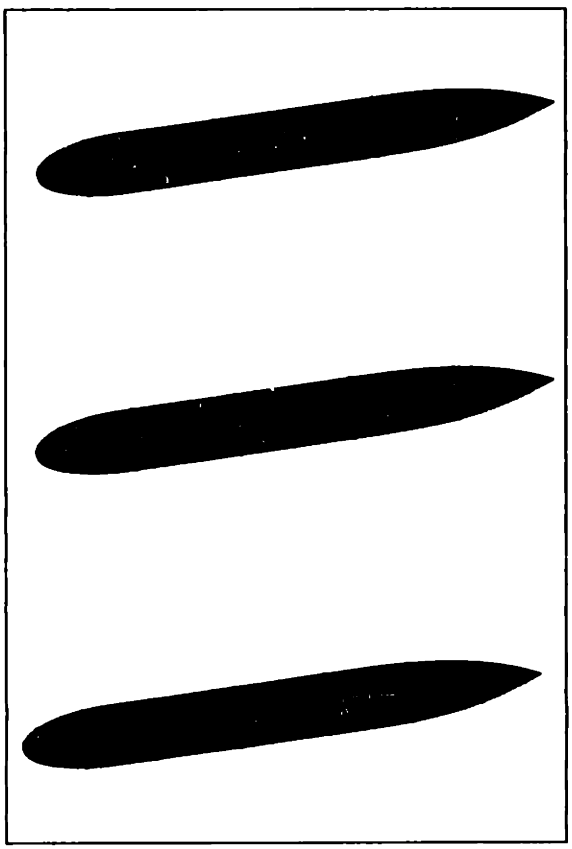

Figure 5-1: 5x4, 7x4 and 9x6 higher-order panels distributed over the analytic submarine. Panels have cosine spacing in the longitudinal direction.

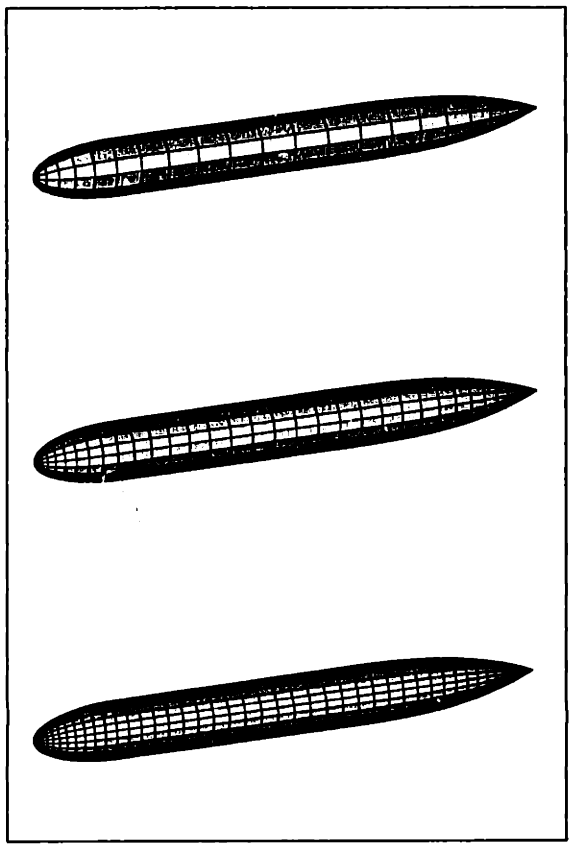

Figure 5-2: Lower-order panel representations of the submarine include bodies with 24x12, 36x18 and 48x24 planar elements. Panels have cosine spacing in the longitudinal direction

compared to those from the lower-order panel code TIMIT. Typical discretizations of this constant-strength planar-panel method are shown in Figure 5-2. Two observations are immediately obvious. Firstly, the higher-order method uses many fewer panels. Secondly, the HITIM computations are carried out over the same geometric surface, whereas the surface of the submarine is converging to its real shape as the number of panels in the lower-order discretizations are refined.

5.2 Steady forces in calm-water

Consider a submarine steadily cruising at a depth such that its longitudinal axis lies a distance $2r_{pmb}$ below the free surface. In order to compare with TIMIT results, the vessel is impulsively accelerated to Fn $= \frac{U}{\sqrt{gL}} = 0.0783$ (5 knots) at $t = 0^+$. The calm-

water forces are produced by the linear Bernoulli pressure, which has the following form at steady-state,

$$\begin{aligned} \mathbf{F}_{\text{steady}} &= -\rho \iint_{B(t)} \frac{\partial \Phi}{\partial t} \mathbf{n}\, dS = -\rho \iint_{B_o} \left(\frac{D\Phi}{Dt} - \mathbf{U} \cdot \nabla \Phi \right) \mathbf{n}\, dS \\ &= \rho \iint_{B_o} U \Phi_x \mathbf{n}\, dS. \end{aligned} \tag{5.3}$$

Convergence of the vertical steady calm-water force computed by TIMIT is shown in Figure 5-3. This steady suction force acts to draw the vessel towards the free surface. The steady moment acting on the body is computed about the longitudinal center of buoyancy and shown in Figure 5-4. Its sign indicates that the moment is in the 'bow-up' direction. The finest discretization contains over one thousand planar panels and would be expected to be suitable for the evaluation of many hydrodynamic quantities. However, even with 60x36 planar panels, the lower-order computations of the steady suction force and trim moment have yet to converge.

Convergence of the steady vertical force and trim moment using HITIM are shown, respectively, in Figures 5-5 and 5-6. Quadratic B-splines are distributed over higher-order panels and lead to effective hydrodynamic discretizations in the geometry-independent method.

5.3 Mean force and moment in waves

Mean forces arise from higher-order interactions of the diffraction field. The time-averaged loads may be computed by the hybrid method of Ferreira [6], which has been implemented in TIMIT. This approach combines time- and frequency-domain techniques, and allows the mean wave loads to be computed over a range of frequencies. We now present results of the mean vertical force and the mean pitch moment for head and following seas. In both cases, the body is impulsively accelerated to $F_n = 0.0783$ and travels steadily at a centerline depth equal to one diameter of the parallel middle body.

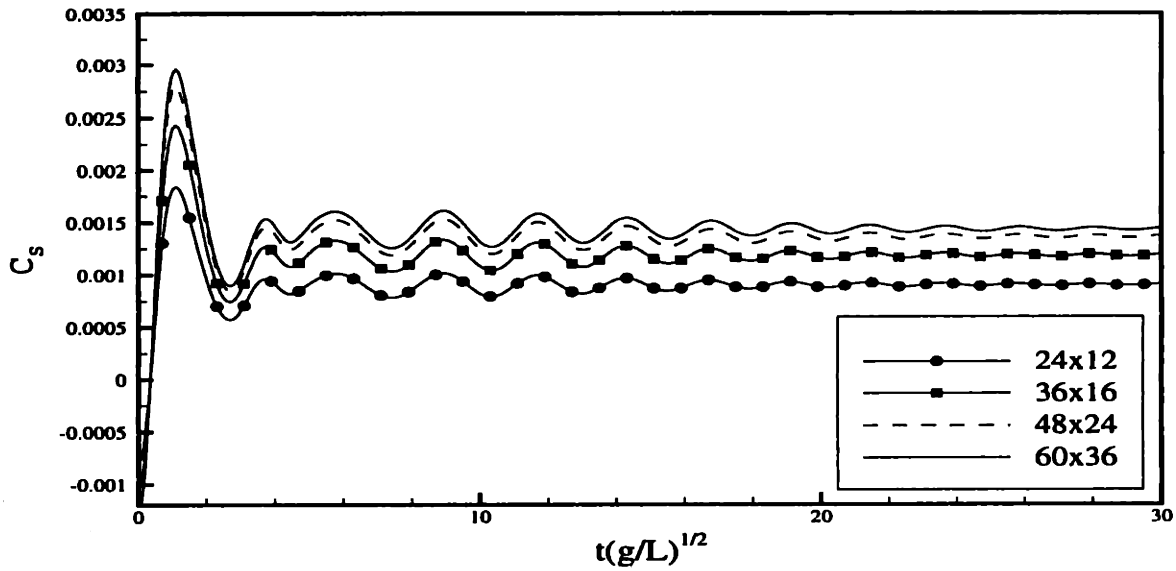

Figure 5-3: Convergence of steady calm-water suction force using **TIMIT**. Non-dimensional force is $C_S = \frac{F_{steady}(3)}{\frac{1}{2}\rho U^2 S}$, where S is the surface area of the submarine. In all runs $\Delta t = 0.10$.

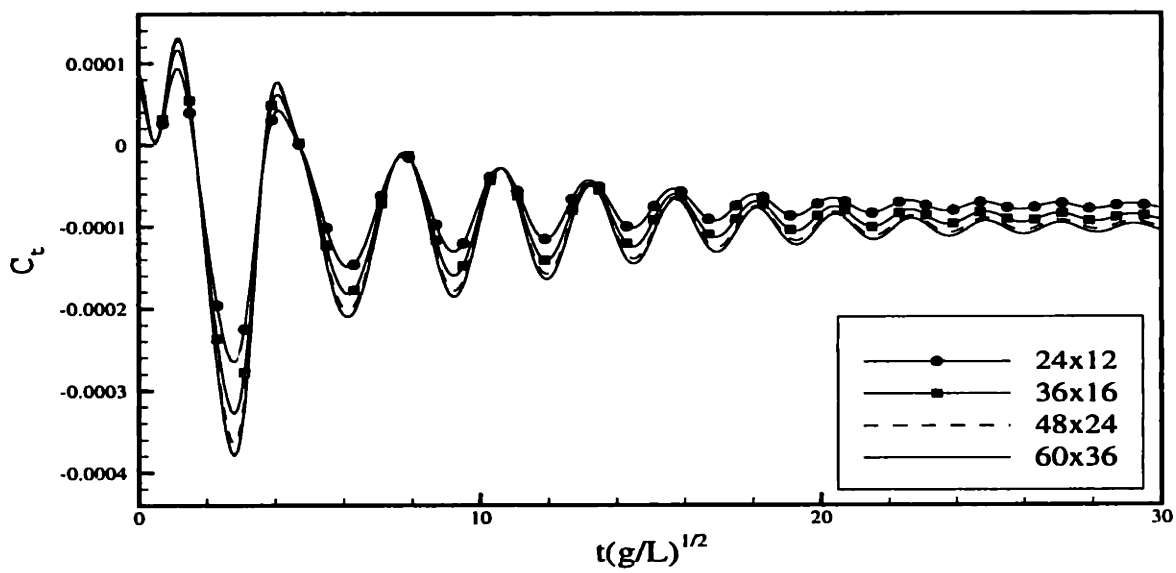

Figure 5-4: Convergence of steady calm-water trim moment using **TIMIT**. Non-dimensional moment is $C_t = \frac{F_{steady}(5)}{\frac{1}{2}\rho U^2 L S}$, where S is the surface area of the submarine, and L is its length. In all runs $\Delta t = 0.10$

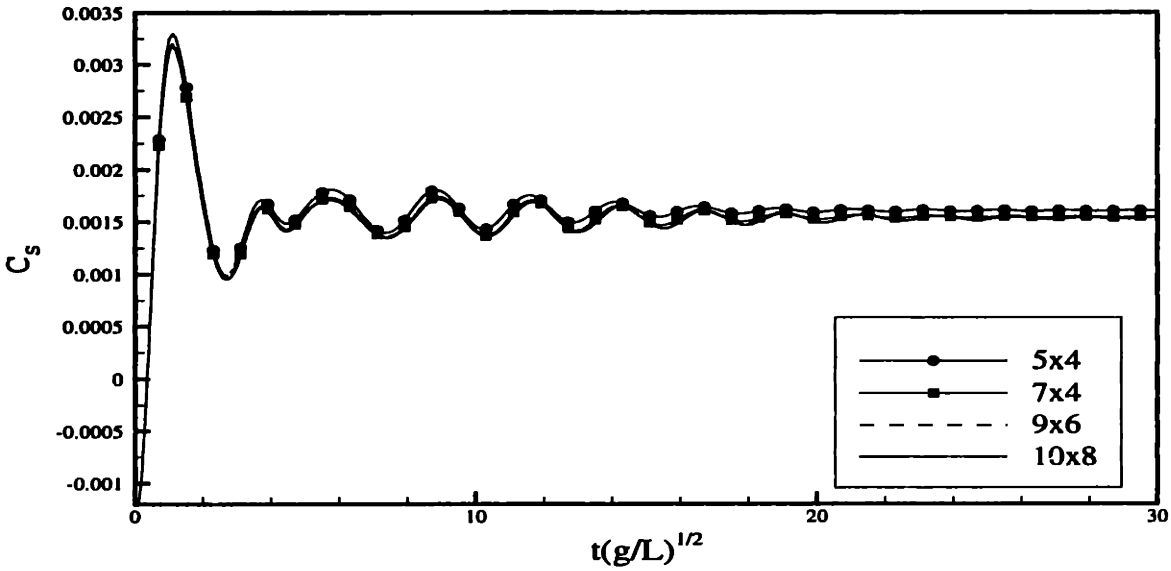

Figure 5-5: Convergence of steady calm-water suction force using **HITIM**. Non-dimensional force is $C_S = \frac{F_{steady}(3)}{\frac{1}{2}\rho U^2 S}$, where S is the surface area of the submarine. In all runs $\Delta t = 0.10$, and $k = 3$

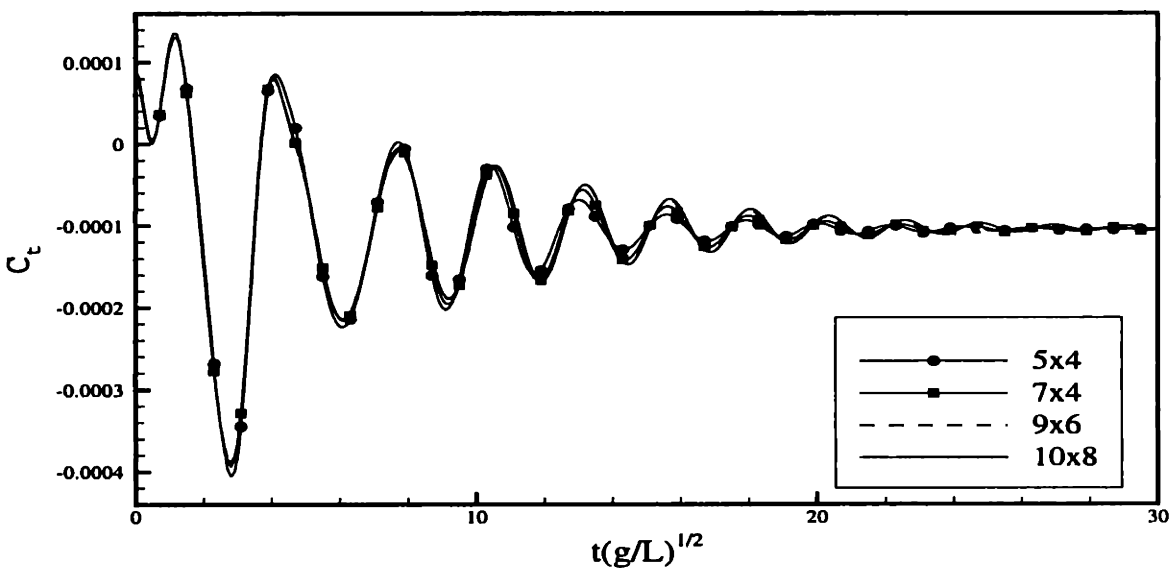

Figure 5-6: Convergence of steady calm-water steady moment using **HITIM**. Non-dimensional moment is $C_t = \frac{F_{steady}(5)}{\frac{1}{2}\rho U^2 L S}$, where S is the surface area of the submarine, and L is its length. In all runs $\Delta t = 0.10$, and $k = 3$

The mean vertical force and pitch moment due to head waves are shown in Figures 5-7 and 5-8. The same quantities developed in following seas are shown in Figures 5-9 and 5-10. In following seas, the mean force and moment have a large value near $\frac{\lambda}{L} \approx 0.2$ due to the $\tau = \frac{1}{4}$ resonance. There, the incident waves propagate energy at exactly the same velocity as the forward speed of the submarine. These lower-order computations require a large number of flat panels in order to reach an converged solution. TIMIT results of the mean loads are nondimensionalized by

$$\tilde{F}_3 = \frac{\bar{F}(3)}{\rho g A^2 L} \tag{5.4}$$

and

$$\tilde{F}_5 = \frac{\bar{F}(5)}{\rho g A^2 L^2}, \tag{5.5}$$

where A is the incident wave amplitude and L is the length of the submarine.

The TIMIT computations show that the mean loads are highly sensitive to wave heading and wavelength. Most notable is the change from a 'bow-down' to a 'bow-up' mean pitch moment as the wave heading changes from head to following seas. For this speed and depth, the largest mean vertical force acting on the submarine is produced by following waves of length $\lambda = 0.75L$. HITIM simulations will be performed with incident waves of this heading, length, and amplitude $A = 0.015L$. Initial transients are minimized by ramping the wave amplitude and the forward speed of the submarine to their steady values.

We integrate the complete Bernoulli pressure in order to determine global forces and moments, but the following definitions are introduced in order to highlight the origin of the mean forces and demonstrate convergence of different quantities.

$$\mathbf{F} = \mathbf{F}^{\text{linear}} + \mathbf{F}^{V^2} \tag{5.6}$$

where,

$$\mathbf{F}^{\text{linear}} = -\rho \iint_{B(t)} \frac{\partial \Phi}{\partial t} \mathbf{n} dS, \tag{5.7}$$

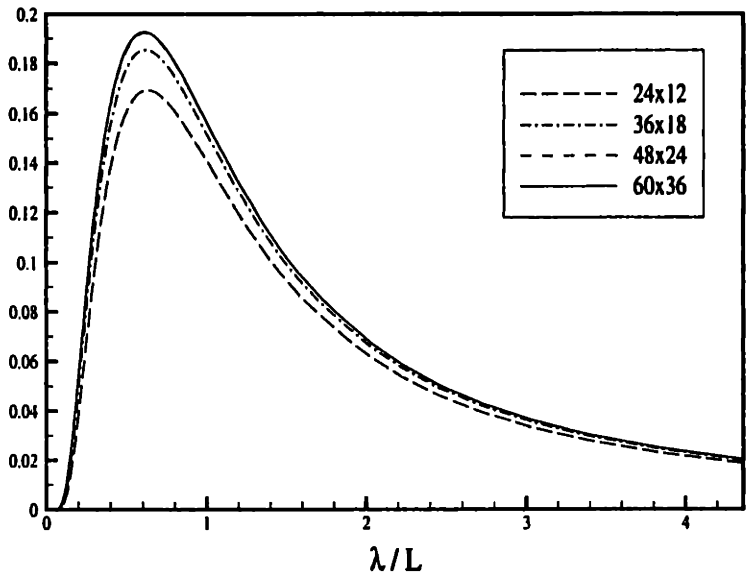

Figure 5-7: Non-dimensional mean vertical force ($\tilde{F}_3$) in head waves. Computations by **TIMIT**.

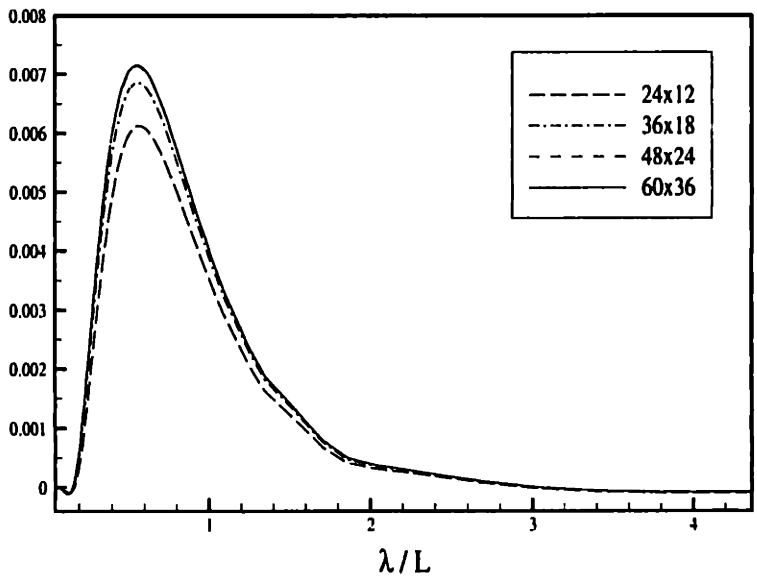

Figure 5-8: Non-dimensional mean trim moment ($\tilde{F}_5$) in head waves. Computations by **TIMIT**.

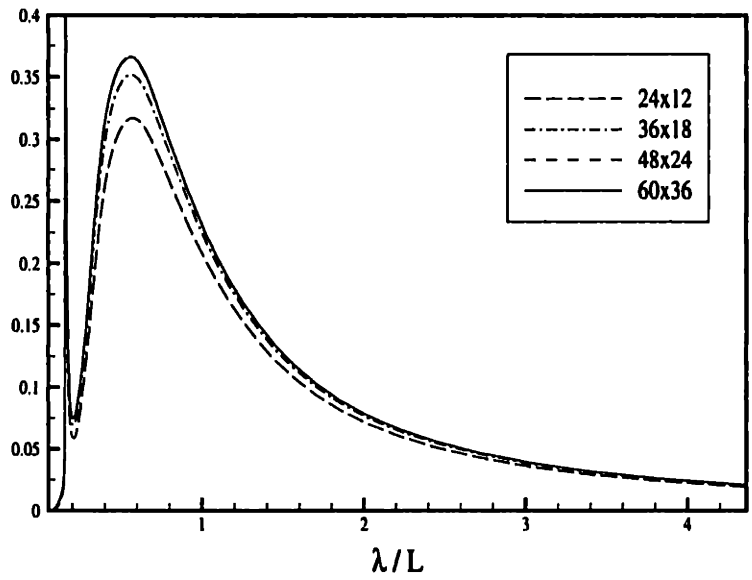

Figure 5-9: Non-dimensional mean vertical force ($\tilde{F}_3$) in following waves. Computations by **TIMIT**.

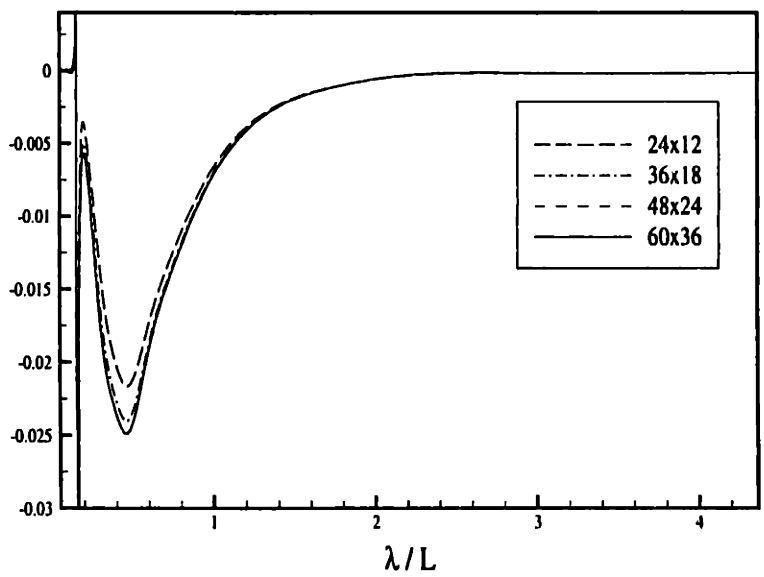

Figure 5-10: Non-dimensional mean trim moment ($\tilde{F}_5$) in following waves. Computations by **TIMIT**.

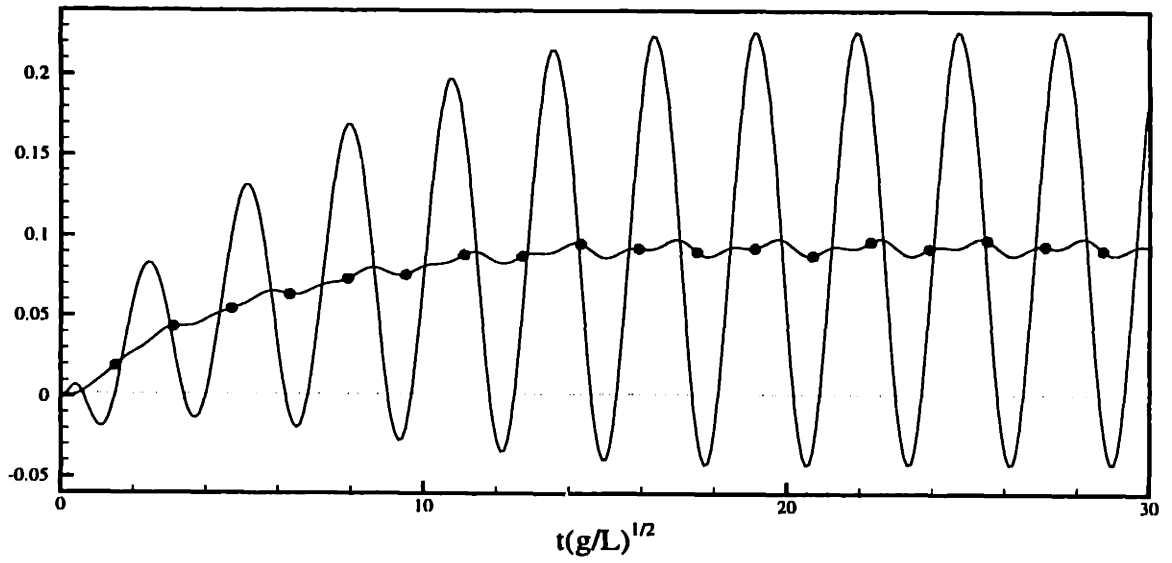

Figure 5-11: Non-dimensional force in the vertical direction is $\frac{F_3}{\frac{1}{2}\rho U^2 S}$, where S is the surface area of the submarine. The contribution to the total force from $F_3^{V^2}$ is shown by the line with circles.

and

$$\mathbf{F}^{V^2} = -\frac{\rho}{2}\iint_{B(t)} V^2 \mathbf{n} dS. \tag{5.8}$$

Figure 5-11 shows the hydrodynamic load acting on the submarine in the vertical direction as the body travels in ambient waves, and reveals the relative importance of the linear and second-order forces. For these conditions, the mean of F^{V^2} is approximately two-thirds of the amplitude of F^{linear}. The integrated value of the linear Bernoulli pressure is shown in Figure 5-12, and demonstrates that vertical component of the linear force, F_3^{linear}, quickly converges to graphical accuracy. A more refined hydrodynamic discretization is required to obtain a converged evaluation of $F_3^{V^2}$, as illustrated in Figure 5-13.

5.4 Depth dependence

Second-order loads on the submarine are due to quadratic interactions of the first-order potential, which suggests that these forces have a vertical attenuation with respect to depth like e^{-2KZ}, where K is the incident wavenumber. This has practical

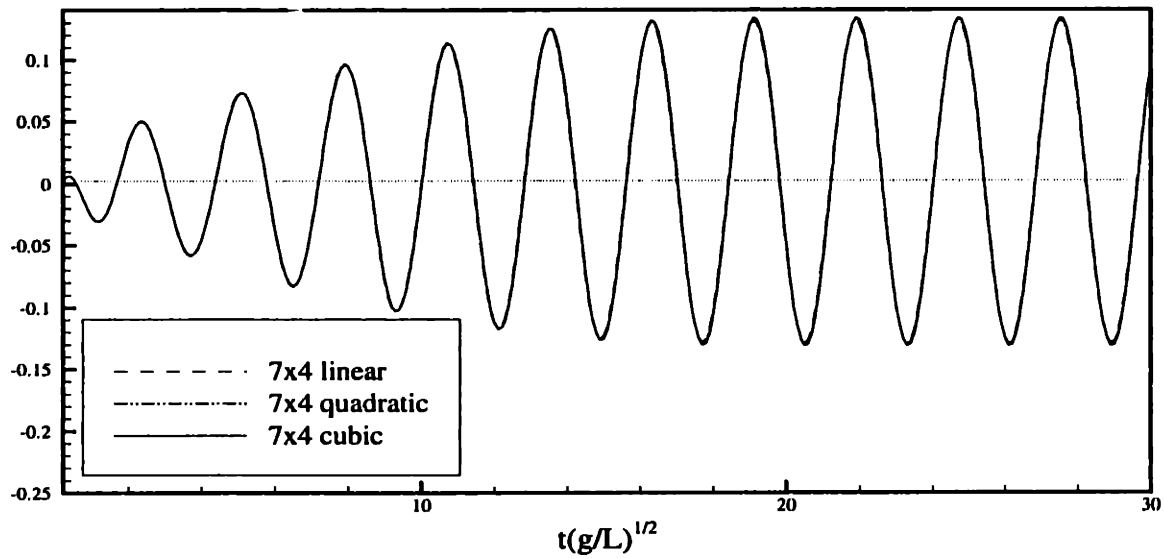

Figure 5-12: Convergence of F_3^{linear} with respect to the B-spline order over 7x4 higher-order panels. The linear force is non-dimensionalized by $\frac{F_3^{\text{linear}}}{\frac{1}{2}\rho U^2 S}$, where S is the surface area of the submarine. In all cases $\Delta t = 0.1$

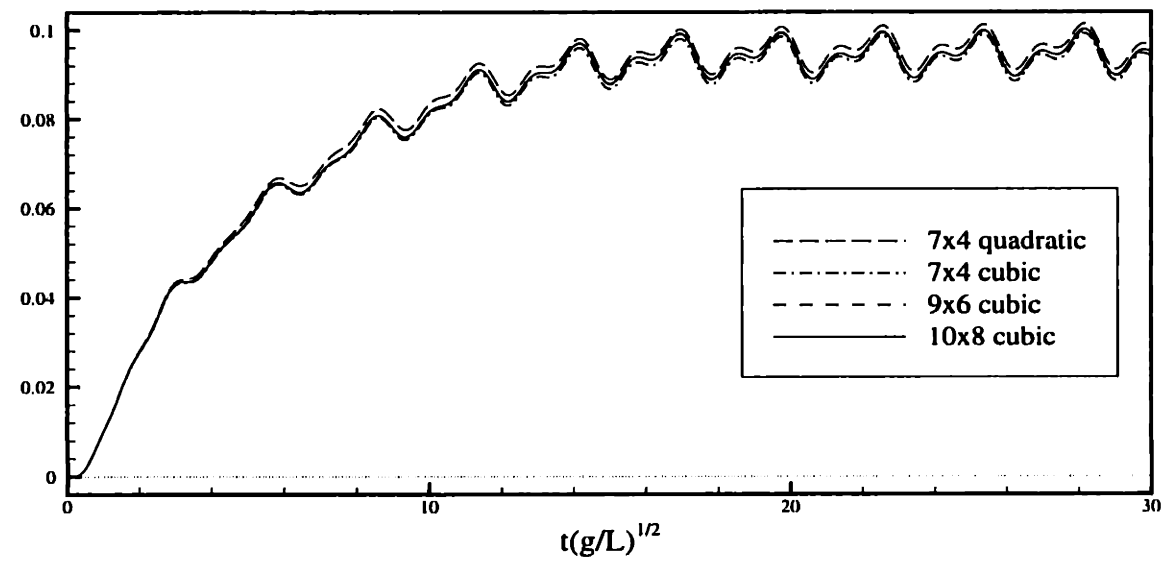

Figure 5-13: Convergence of $F_3^{V^2}$ with respect to the B-spline order and number of higher-order panels. The second-order force is non-dimensionalized by $\frac{F_3^{V^2}}{\frac{1}{2}\rho U^2 S}$, where S is the surface area of the submarine. In all cases $\Delta t = 0.1$

implications for a submarine maneuvering to periscope depth, because the mean forces may increase from a near-zero value when the vessel is deeply submerged, to a non-negligible magnitude as the body approaches the free surface. A body-exact solution is obtained to examine the transient first- and second-order hydrodynamic forces as the submarine follows a prescribed trajectory which is representative of a maneuver to periscope depth.

Time histories of the vertical motion and pitch angle are given in Figures 5-14 and 5-15. The vessel is smoothly accelerated to a forward speed of 5 knots in monochromatic following seas of $\lambda = 0.75L$ and amplitude $A = 0.015L$. The submarine begins the simulation at a depth of $4.5\,r_{pmb}$ and reaches a final centerline depth of $1.82\,r_{pmb}$. During its upwards motion, a 'bow-up' trim angle of 5° is prescribed.

The time history of the vertical force acting on the submarine during this maneuver is shown in Figure 5-16. For small values of time, the body has moderately deep submergence, and the mean vertical force is small compared to the oscillatory load. The wave-frequency loads increases in magnitude as the vessel nears the free surface. Likewise, the quadratic interactions grow in strength, and the mean vertical force in non-negligible at the low submergence.

The trim moment acting on the body during the maneuver is shown in Figure 5-17. The magnitude of the mean load, relative to the amplitude of the oscillating component, is less dominant in the pitch moment than in the heave force. However, a mean trim moment is observed at the final cruising depth.

5.5 Auto-piloted maneuver

A more realistic simulation of the periscope maneuver would allow the vessel to respond to waves while maintaining the gross motion given in Figures 5-14 and 5-15. Since the submarine is neutrally buoyant, an autopilot must be included to offset the second-order wave-induced loads and transients associated with the momentum

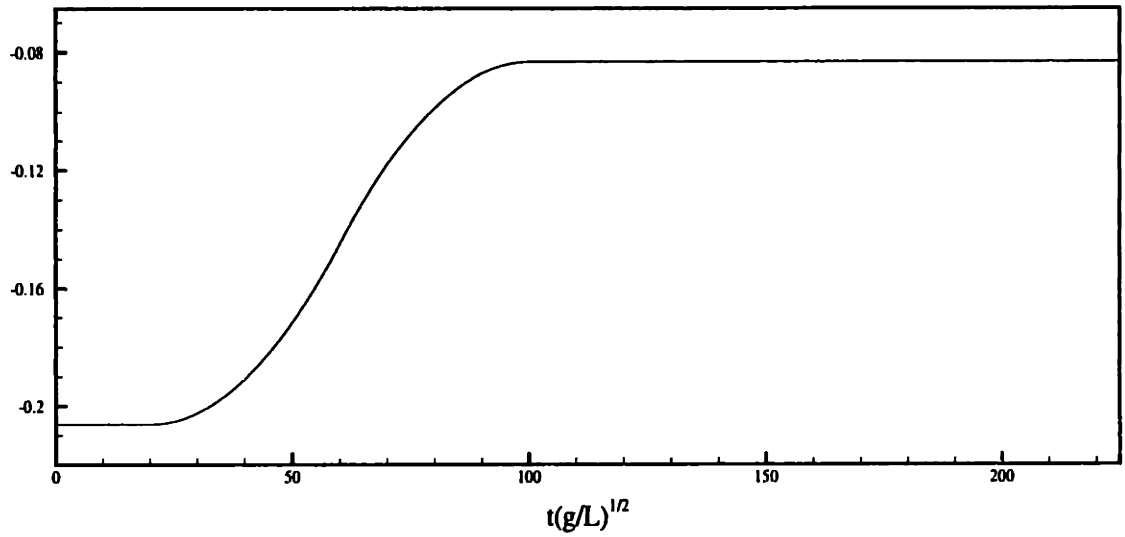

Figure 5-14: Vertical trajectory of the submarine. Initial centerline depth is $4.5\, r_{pmb}$, and the final depth is $1.82\, r_{pmb}$.

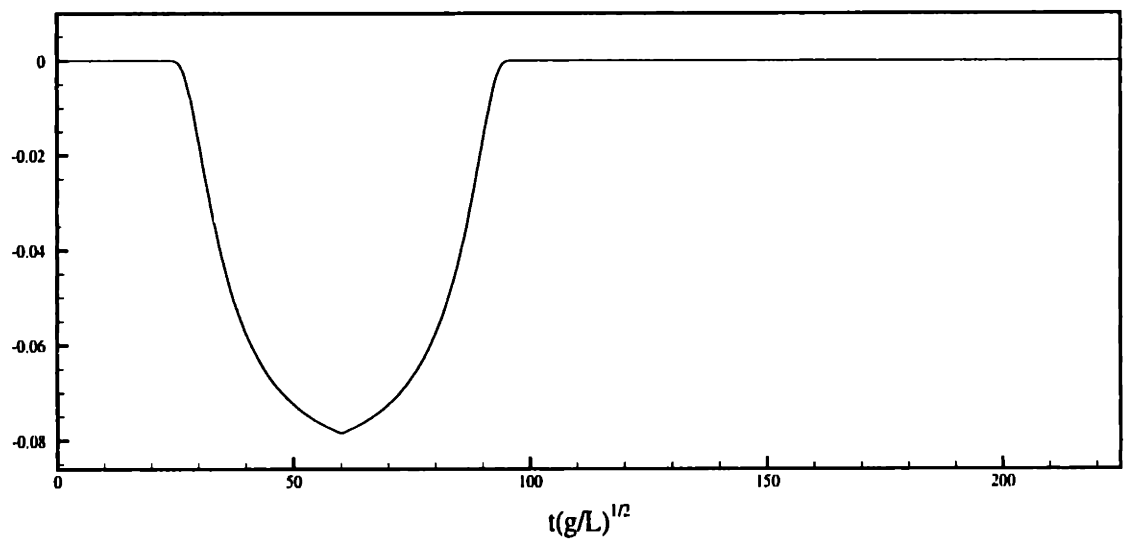

Figure 5-15: Pitch trajectory of the submarine. The maximum trim angle is 5°.

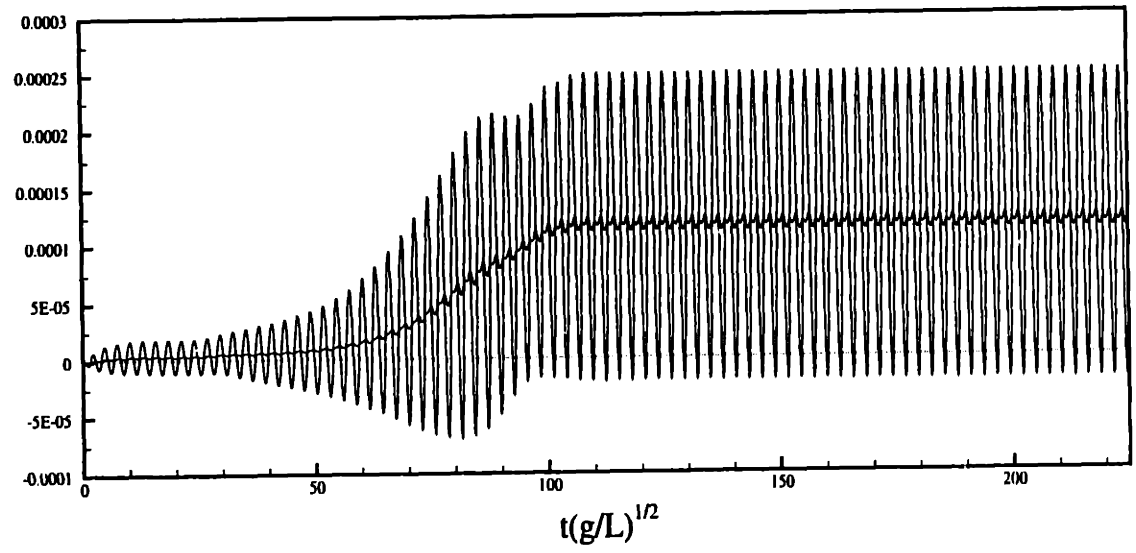

Figure 5-16: The vertical hydrodynamic force (F_3) on the submarine during the maneuver shown in Figures 5-14 and 5-15. The line along the mean value shows the contribution from $F_3^{V^2}$ to the total hydrodynamic force.

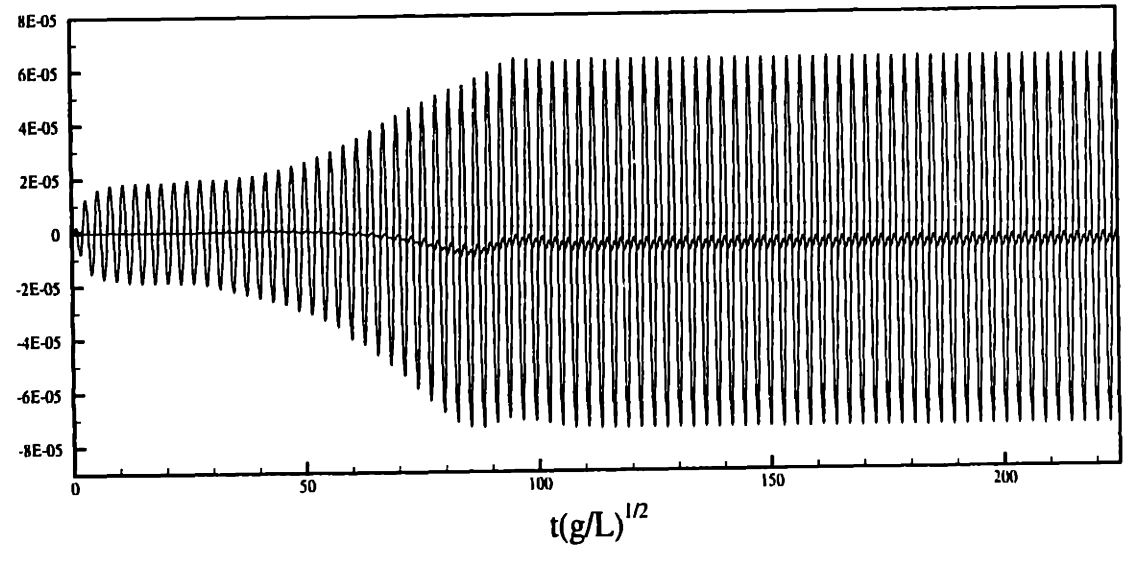

Figure 5-17: The hydrodynamic trim moment (F_5) on the submarine during the maneuver shown in Figures 5-14 and 5-15. The line along the mean value shows the contribution from $F_5^{V^2}$ to the total hydrodynamic force.

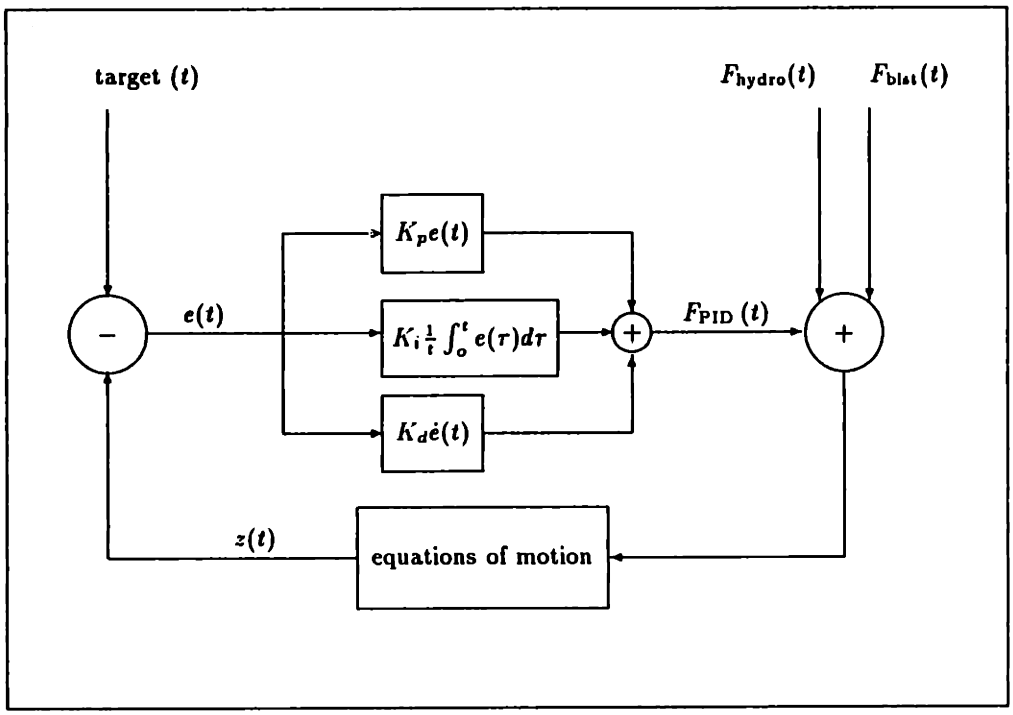

Figure 5-18: The PID + ballast autopilot. $F_{PID}(t)$ is the force from the PID controller, $F_{hydro}(t)$ is the hydrodynamic force, $F_{blst}(t)$ is the negative buoyancy from ballast, $z(t)$ the actual submarine depth, and $e(t)$ the error in position.

Parameters of the autopilots				
mode	K_p	K_i	K_d	ballast
heave	8.5×10^{-3}	12.75×10^{-3}	3.4×10^{-3}	-1.25×10^{-4}
pitch	4.0×10^{-3}	8.0×10^{-3}	2.8×10^{-3}	-1.0×10^{-5}

Table 5.1: The values of the PID + ballast controllers

of the body. For this purpose, a proportional-integral-derivative (PID) controller was used in addition to a negative buoyancy representing the effect of ballast. Unless the ballast is arranged such that it does not change the longitudinal center of gravity, a non-zero pitch moment is developed. Figure 5-18 shows the schematics of the autopilot. The parameters of the PID controller were numerically tuned by performing several body-exact simulations. The settings given in Table 5.1 produced a suitable PID + ballast autopilot.

The same wave conditions and forward speed are prescribed as in the preceding

section, but now the body is allowed to respond in heave and pitch. Using two independent PID + ballast controllers, we are able to achieve the motions shown in Figures 5-19 and 5-20. The large-amplitude motion of the submarine follows the target path well in both modes. In addition, the body assumes small-amplitude oscillations due to the wave-induced loads and forces from the K_p and K_d components of the autopilot. As expected, the wave-frequency motions increase in magnitude as the submarine nears the free surface.

The hydrodynamic force in the vertical direction is shown in Figure 5-21. Comparing the hydrodynamic loads in the present simulation with those plotted in Figure 5-16, it is evident that the wave-frequency heave force is reduced when the body is allowed to respond to the incident waves. However, the mean vertical component of the second-order force remains about the same. The slight overshoot in vertical motion produces a substantial transient in the hydrodynamic force. The hydrodynamic trim moment of Figure 5-22 shows that the linear Bernoulli pressure dominates the second-order moment throughout the maneuver.

Figures 5-23 and 5-24 show, respectively, the time histories of the external vertical force and pitch moment supplied by the autopilot. Ballast is slowly added for $t\sqrt{g/L} > 60$ and offsets the second-order hydrodynamic force. The K_i term of the autopilot produces a slowly-varying vertical force to correct for the difference between the ballast and mean vertical force. The wave-frequency component of the external force is generated by the K_p and K_d terms.

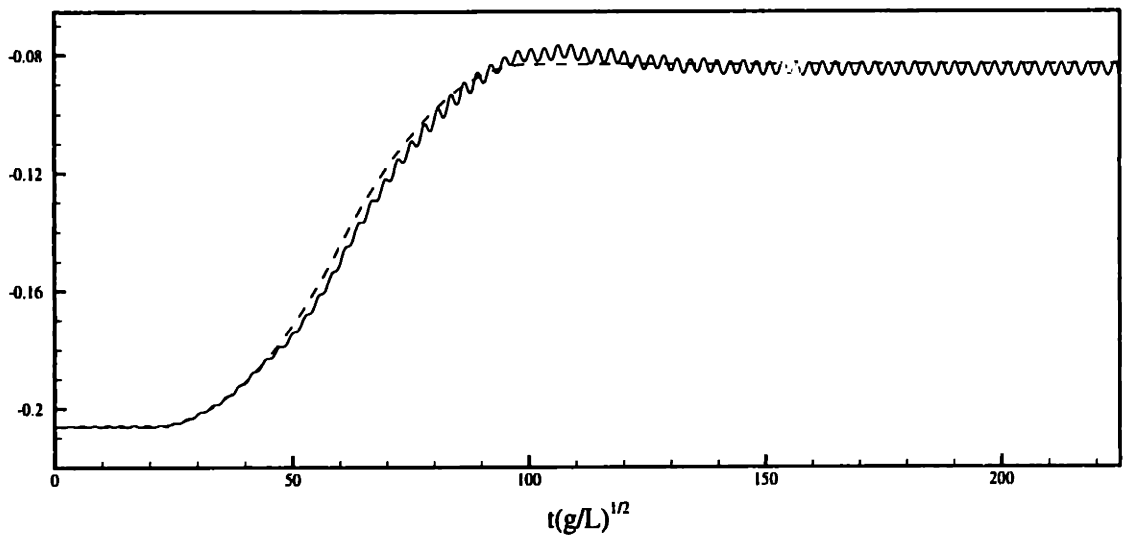

Figure 5-19: Heave motion assumed by the piloted submarine. The dashed line shows the target path of the vertical motion.

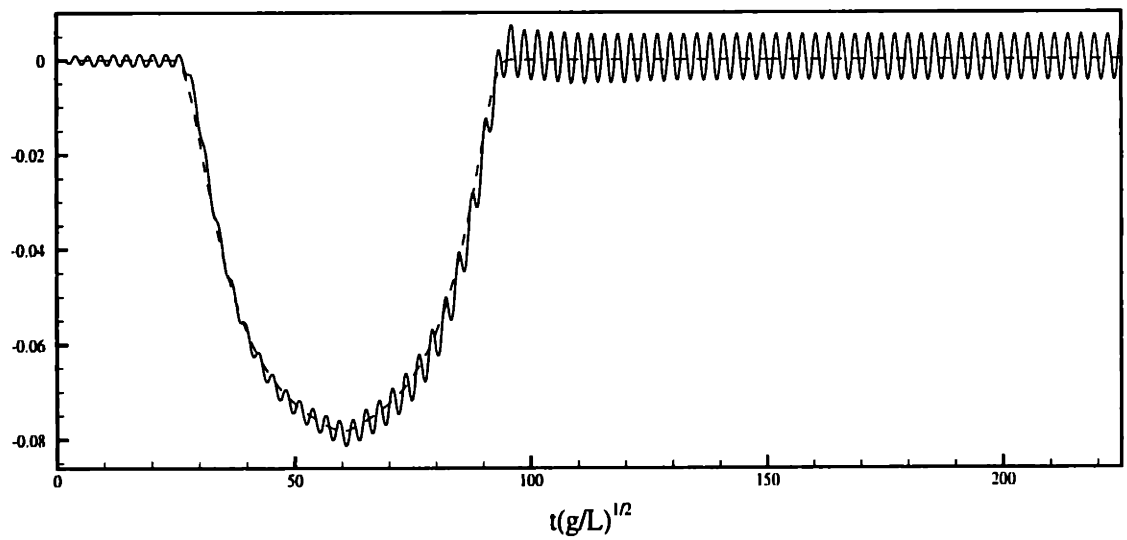

Figure 5-20: Pitch motion assumed by the piloted submarine. The dashed line shows the target pitch angle.

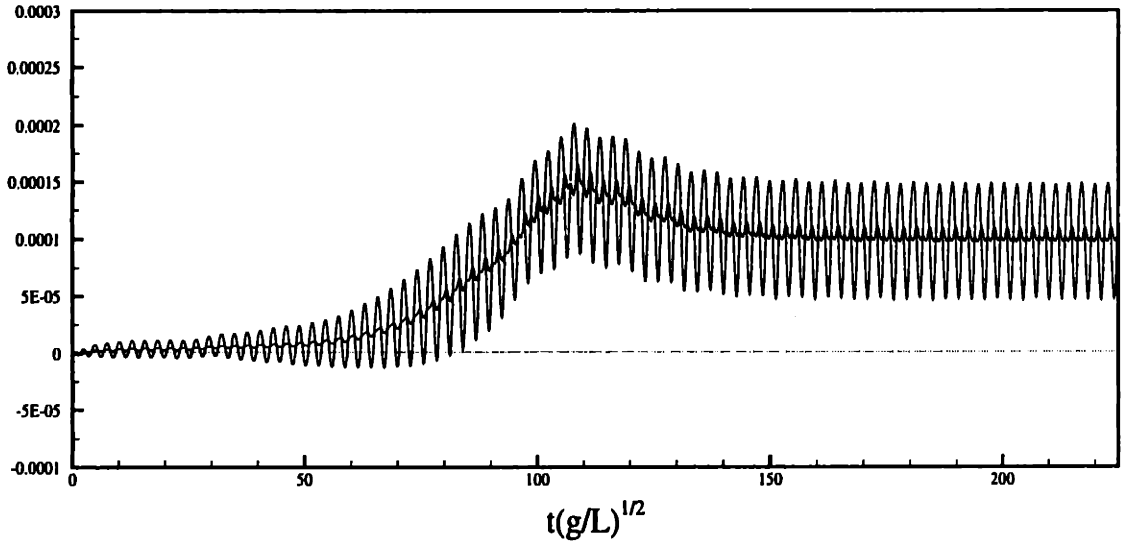

Figure 5-21: Hydrodynamic forces in the vertical direction. The line along the mean value shows the contribution from F^{V^2} to the total hydrodynamic force.

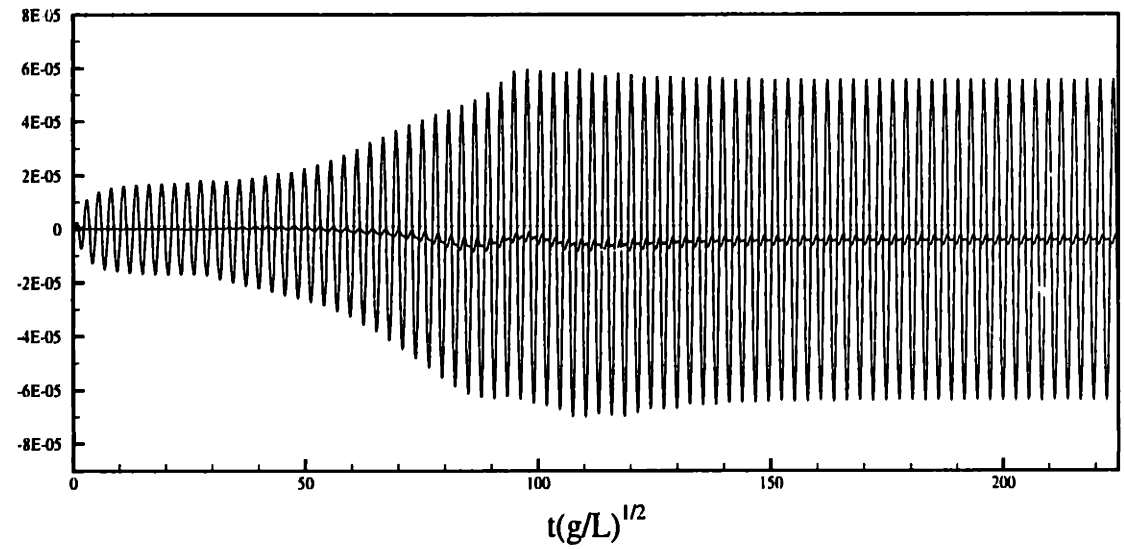

Figure 5-22: Hydrodynamic pitch moments. The line along the mean value shows the contribution from F^{V^2} to the total hydrodynamic moment.

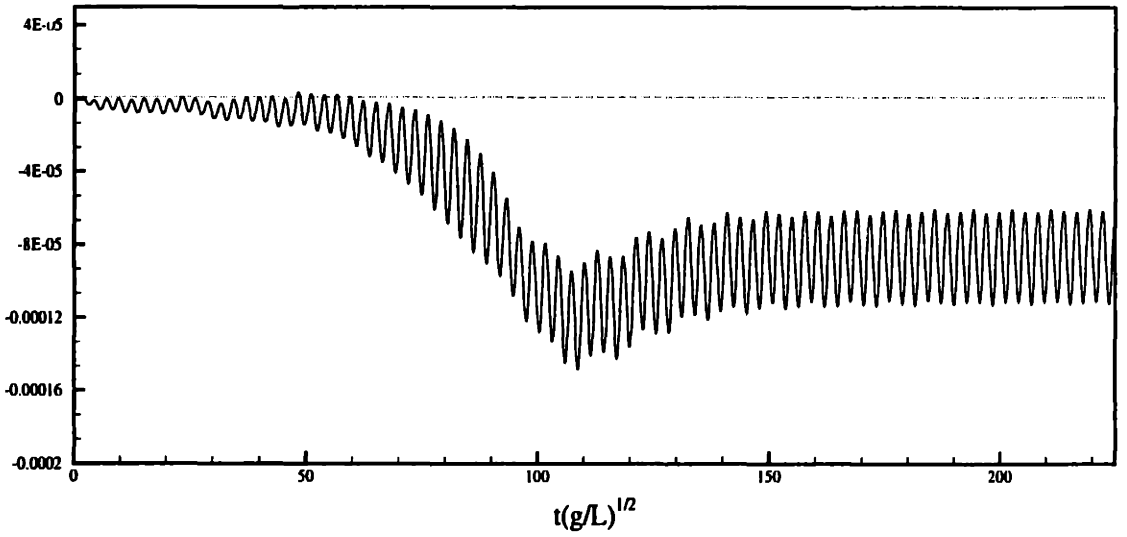

Figure 5-23: Vertical forces developed by PID+ballast autopilot during the maneuver.

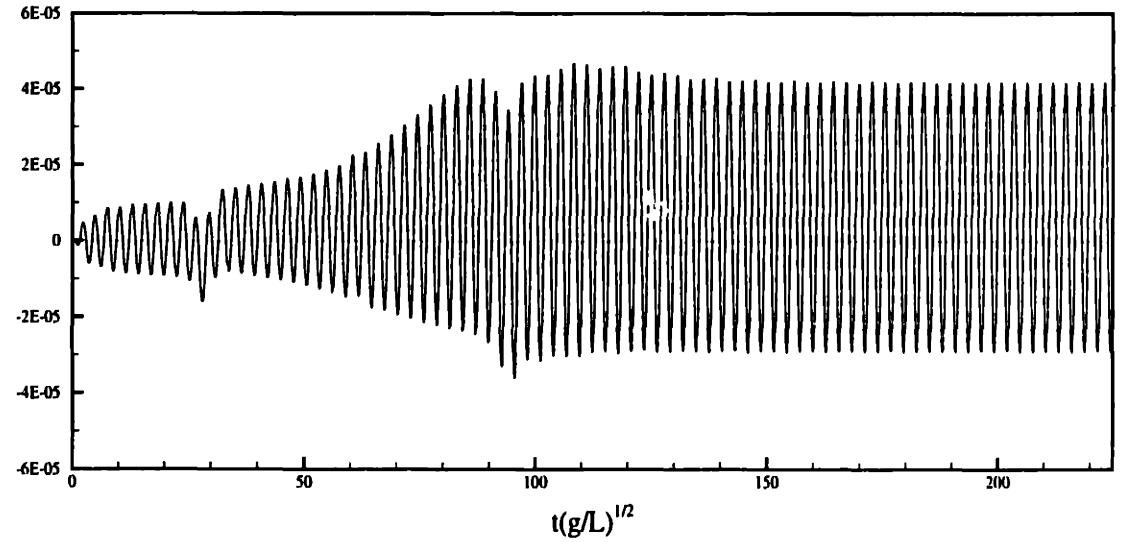

Figure 5-24: Pitch moment developed by PID+ballast autopilot during the maneuver.

Chapter 6

Hydrodynamic Interactions of Neighboring Bodies

Subtle hydrodynamic interactions of two or more neighboring bodies may significantly change the wave flow and resulting body motions. One such example of marine interest is the drift motion of a body that floats in proximity to a fixed structure. Ohkusu [51] carried out model tests in which a ship floating alongside a moored structure obtained drift motions in the direction *opposite* to the incident wave propagation. Additionally, his computations, based on approximate two-dimensional potential theory, predicted a negative drift force on the ship for a range of wave frequencies.

The present study uses a more complete three-dimensional solution to examine the hydrodynamic coupling between the sphere and circular cylinder shown in Figure 6-1. Each body is of radius a, and the draft of the cylinder is $2a$. We will consider the axis of the two bodies to be separated by a distance $2d$. The bodies are subject to monochromatic waves such that the sphere lies on the weather side of the truncated circular cylinder. For ambient waves of amplitude A traveling in the $+X$ direction, the incident potential is

$$\varphi = \frac{gA}{\omega} e^{KZ} \sin(KX + \omega t + \theta) \,, \tag{6.1}$$

where $\omega^2 = gK$, and θ is the phase angle. Of primary interest are the forces on the sphere and its resulting motions as it drifts in the vicinity of the cylinder. The hydrodynamic features of the sphere-cylinder case are representative of more general

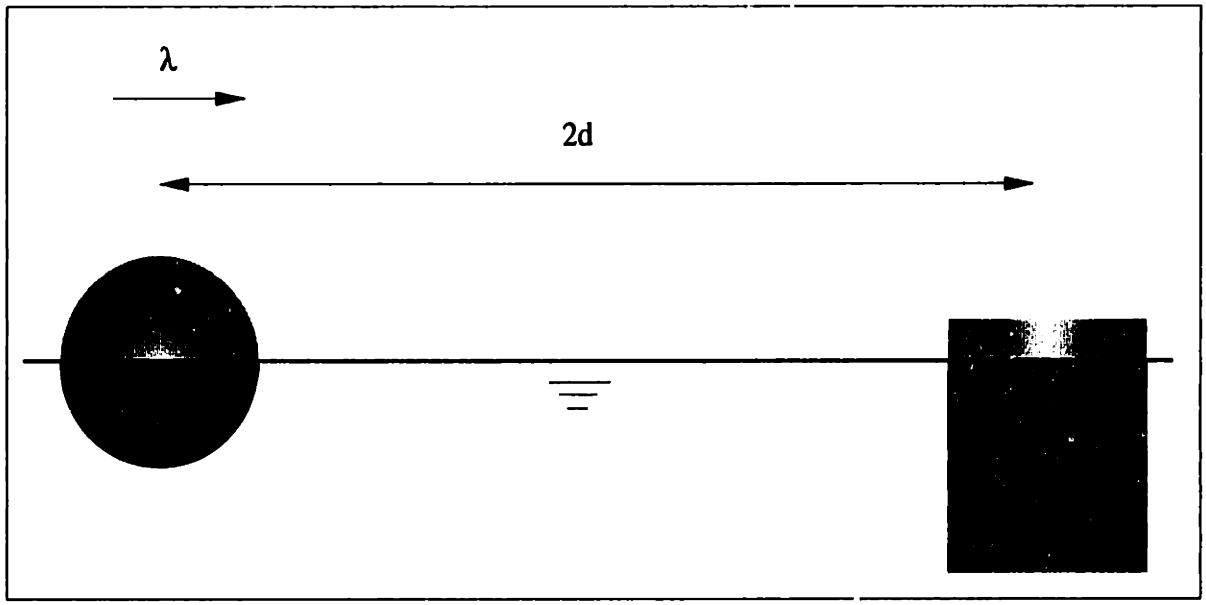

Figure 6-1: The sphere-cylinder arrangement shown in its equilibrium configuration. Distance from the center of the sphere to axis of the cylinder is $2d$. The sphere and cylinder have unit radii, and the draft of the circular cylinder is equal to its diameter. The dry portions of the bodies are shown along with the discretization of the surfaces below $Z = 0$.

multi-body applications, which are common to many marine operations.

The use of a simplified free-surface boundary condition in the present case is justified by an argument put forth by Triantafyllou [54]. He combined multiple time scales and amplitude expansions to derive a theory in which the flow generated due to slow drift motion is governed by a first-order potential that satisfies a linear and homogeneous free-surface boundary condition. The basic assumption is that although the drift motions are large in amplitude, the disturbances they generate may be linearized since the drift velocity is small.

Quadratic interactions of the first-order potential give rise to a second-order force which is proportional to the square of the wave amplitude, and includes the mean drift force as well as a second-harmonic component. A body-exact simulation will allow us to examine the parametric dependence of this drift force on the relative spacing between bodies, and couples hydrodynamic transients with the momentum of the floating sphere. This lift the restrictions of constructing an ad hoc estimate of the drift motions by the solution of a series time-harmonic flows at various spacings.

6.1 A linearized steady-state analysis

Before simulations are performed, a preliminary linearized analysis is carried out in order to gain insight into the hydrodynamic coupling of the two bodies. The geometry-independent higher-order panel code HIPAN is used to determine the variation of mean force with respect to wave frequency and distance of separation, and if any negative drift forces can be realized in the sphere-cylinder arrangement.

First consider the case where both the sphere and cylinder are held fixed and subject to planar waves. The mean drift force on each body is determined as a function of $\frac{Kd}{\pi}$ for three different separation distances. The nondimensional horizontal mean forces on the sphere and cylinder are shown, respectively, in Figures 6-2 and 6-3. At a separation distance of $2d = 5$, body-body interactions produce a negative drift force on the sphere in the range of $\frac{Kd}{\pi} = 0.20$ to 0.40, with its peak near $\frac{Kd}{\pi} = 0.30$. This repulsive force becomes progressively stronger as the distance between the two bodies is reduced to $2d = 4$ and $2d = 3$. In contrast to the mean force acting on the sphere, the drift force on the cylinder remains positive and is always greater in magnitude for the frequency range that produces negative drift forces on the sphere. Therefore, in accordance with theory, the total drift force on the combined system is in the direction of incident wave propagation for all frequencies and separation distances.

The same numerical experiment was performed with the sphere free to assume small oscillations in surge, while keeping the cylinder fixed. Here, the hydrodynamic boundary value problem and pressure integration are defined over the mean position of the body. HIPAN computations of the resulting drift forces on the sphere and cylinder are shown in Figure 6-4 and 6-5, respectively. Allowing the sphere to partially respond to waves results in a general decrease in both the positive and negative drift force acting on the sphere. However, we still observe a negative drift force in the same frequency range as before.

A third steady-state analysis is carried out in which the sphere is allowed to linearly respond in both surge and heave. Again, the flow is computed about the equilibrium position of the sphere. In this case, the vertical body motions of the floating sphere significantly change the drift forces shown in Figures 6-6 and 6-7. Instead of the repulsive force growing for decreasing distances of separation, the negative drift force is absent from the $2d = 3$ configuration. For $2d = 4$, a relatively strong repulsive force appears in the range of $\frac{Kd}{\pi} = 0.40$ to 0.60. A weaker repulsive drift force is observed at a separation distance of $2d = 5$ for waves from $\frac{Kd}{\pi} = 0.42$ to 0.65.

Relating the body-body interactions of the sphere and cylinder to the trapping of waves in a channel helps explain the mean repulsive force. Maniar and Newman [35] investigated the diffraction of waves by long arrays of cylinders of infinite draft, with a spacing between consecutive elements of $2d$. From their analysis, the authors found that quasi-resonant wave interactions occur at critical values of $\frac{Kd}{\pi}$. For the cases of very long arrays, large exciting forces were observed just below the cut-off frequency of $\frac{Kd}{\pi} = \frac{1}{2}$ that corresponds to trapped waves in a channel. Strictly speaking, waves cannot be 'trapped' in an array of finite extent, because energy is radiated into the far field. However, the structure of the flow about the array of cylinders was found to be similar to wave motion in a rectangular channel. Since the normal derivative of the potential must be zero along fictitious sidewalls between neighboring cylinders, this resonance is referred to as a 'Neumann trapped wave'. Numerical results from [35] show that for long arrays of cylinders, the localized wave build-up between bodies is considerably larger than the incident wave elevation. This type of wave trapping is not particular to circular cylinders. Evans and Porter [10] have observed wave-trapping in systems that consist of only a few elements.

In the present case, any localized 'sloshing' between the sphere and cylinder resulting from partial wave trapping may act to repel the two bodies. Figure 6-8 shows the first-order surge exciting force and mean drift force on the sphere for a separation

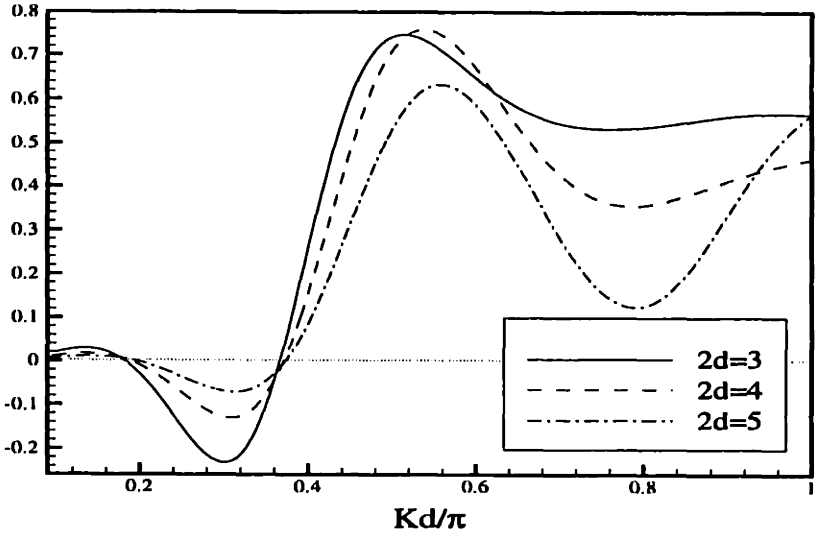

Figure 6-2: Mean drift force on fixed sphere versus $\frac{Kd}{\pi}$. Non-dimensional force is $\frac{\bar{F}}{\rho g A^2}$, where the overbar denotes time average. Computations by **HIPAN**.

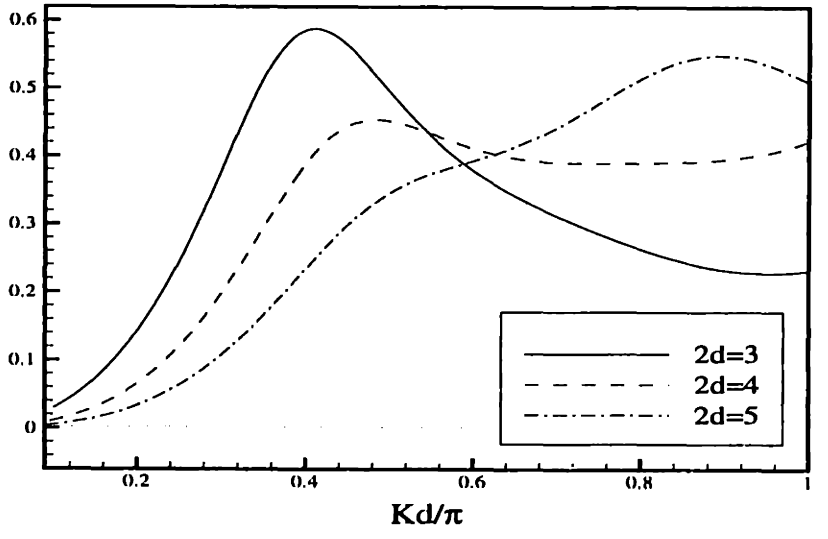

Figure 6-3: Mean drift force on fixed cylinder versus $\frac{Kd}{\pi}$. Non-dimensional force is $\frac{\bar{F}}{\rho g A^2}$, where the overbar denotes time average. Computations by **HIPAN**.

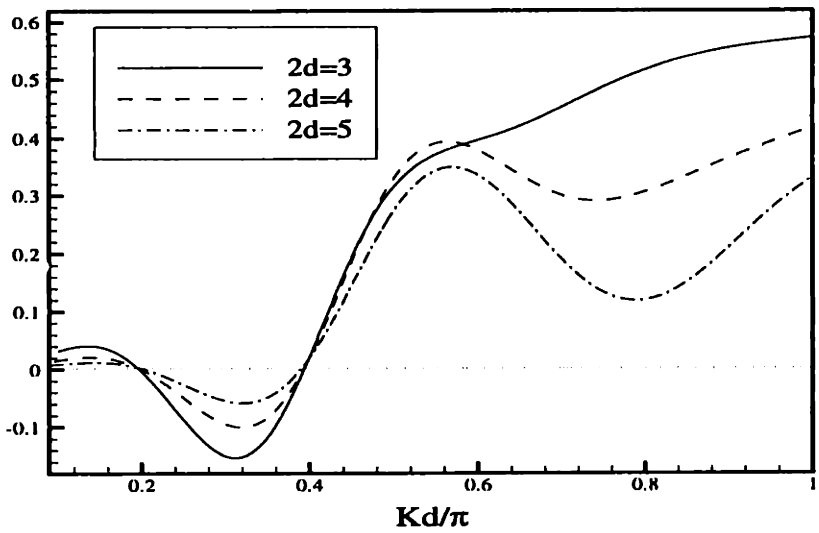

Figure 6-4: Mean drift force on floating sphere versus $\frac{Kd}{\pi}$. Sphere is free in surge. Non-dimensional force is $\frac{\bar{F}}{\rho g A^2}$, where the overbar denotes time average. Computations by **HIPAN**.

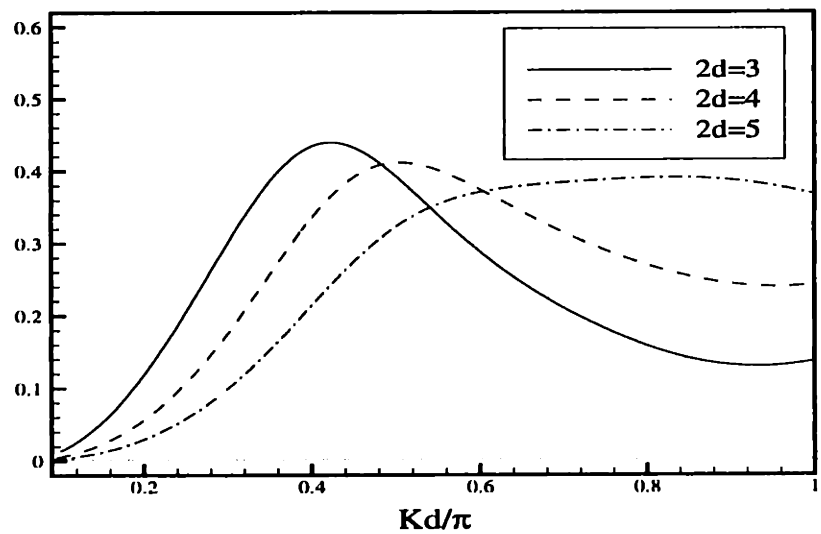

Figure 6-5: Mean drift force on fixed cylinder versus $\frac{Kd}{\pi}$. Sphere is free in surge. Non-dimensional force is $\frac{\bar{F}}{\rho g A^2}$, where the overbar denotes time average. Computations by **HIPAN**.

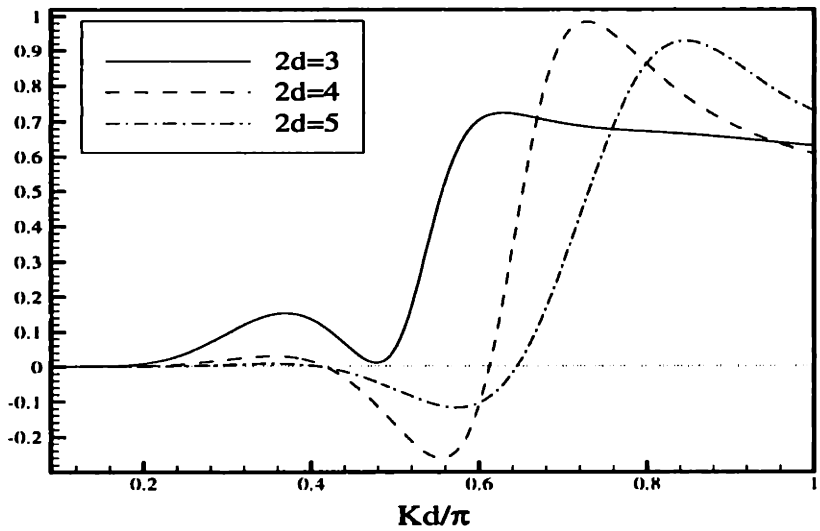

Figure 6-6: Mean drift force on floating sphere versus $\frac{Kd}{\pi}$. Sphere is free in surge and heave. Non-dimensional force is $\frac{\bar{F}}{\rho g A^2}$, where the overbar denotes time average. Computations by **HIPAN**.

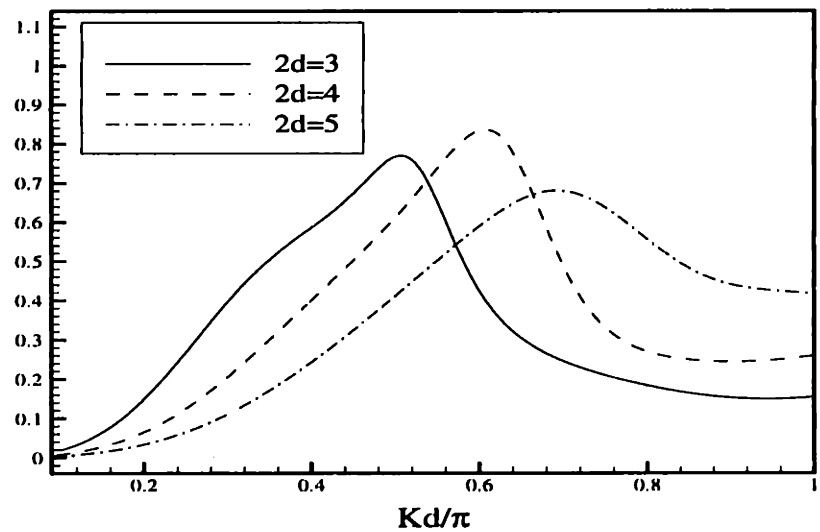

Figure 6-7: Mean drift force on fixed cylinder versus $\frac{Kd}{\pi}$. Sphere is free in surge and heave. Non-dimensional force is $\frac{\bar{F}}{\rho g A^2}$, where the overbar denotes time average. Computations by **HIPAN**.

distance of $2d = 3$. The same quantities for a single, isolated sphere are plotted for comparison. Indeed, the first Neumann trapped mode occurs near the critical wavelength that produces the upwave drift force. The mean force is highly sensitive to the $\frac{Kd}{\pi}$ parameter in the range of this first quasi-resonance. More trapped waves are found for shorter wavelengths, but these weaker resonances are not strong enough to produce a repulsive mean force of considerable magnitude.

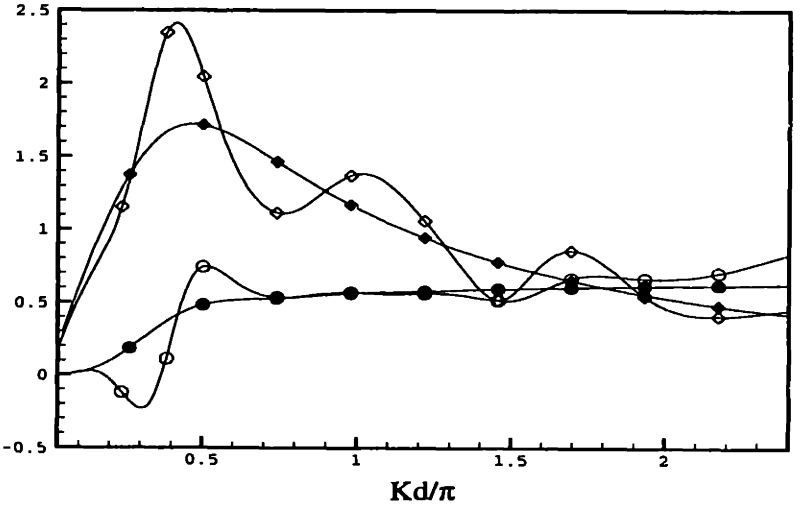

Figure 6-8: Surge exciting force (empty diamonds) and mean drift force (empty circles) on fixed sphere in the presence of a cylinder. Separation distance is $2d = 3$. The exciting force (filled diamonds) and mean drift force (filled circles) experienced by a single, isolated sphere are shown to demonstrate the effect of interference caused by presence of the second body. Computations by **HIPAN**.

6.2 Rise-time of the negative drift force

The frequency-domain results presented above demonstrate the existence of a repulsive mean force under certain conditions, but the implications of this are not obvious. Body momentum and hydrodynamic transients will determine if a floating sphere will continue to drift downwave and collide with the fixed cylinder. We now examine how quickly or slowly the hydrodynamic mean force reaches a steady-state value by solving a transient diffraction problem. In Section 6.3, a transient hydrodynamic solution is combined with the rigid-body mechanics in the motion simulation of the floating

sphere.

The leading order contributions to the drift force come from quadratic interactions in the pressure integration. In order to compare HITIM results with HIPAN computations, we define the second-order surge force as

$$F^q(t) = -\frac{\rho}{2}\iint_{B(t)} V^2 n_1 dS + \frac{\rho g}{2}\int_{\Gamma(t)} \zeta^2 n_1 dl, \tag{6.2}$$

where n_1 is the component of the unit normal in the $+X$ direction. All other terms retain their previous definitions.

Monochromatic waves of $Ka = 0.628$ are supplied for two different separation distances. The amplitude of the incident waves is ramped up to a final value of $\frac{A}{a} = 0.1$. Figure 6-9 shows the time history of the surge force acting on the sphere when both bodies are restrained at a separation distance of $2d = 5$ $\left(\frac{Kd}{\pi} = 0.50\right)$. The same quantity for a single, isolated sphere is shown for comparison. F^q is plotted in nondimensional form for the multi- and single-body cases in Figure 6-10. For this separation and wavelength, the presence of the cylinder acts to increase the drift force to approximately $\bar{F}^q \approx +0.4$.

The time-history of the force acting on the sphere for the same incident waves and a separation distance of $2d = 3$ $\left(\frac{Kd}{\pi} = 0.30\right)$ is shown in Figure 6-11. The amplitude of the oscillatory force is approximately equal to that of the previous case. A more subtle result is the change of its mean value. The second-order surge forces acting on the sphere in the presence of the cylinder and on a single, isolate sphere are plotted in Figure 6-12. The presence of the cylinder acts to increase the magnitude of F^q and changes its mean value to approximately $-.20$.

6.3 The upwave drift of a floating body

Consider the two-body arrangement previously described, with the sphere unrestrained in surge but fixed in its other rigid-body modes. For incident waves of $Ka = 0.628$, the frequency-domain results in Figure 6-4 show a negative drift force

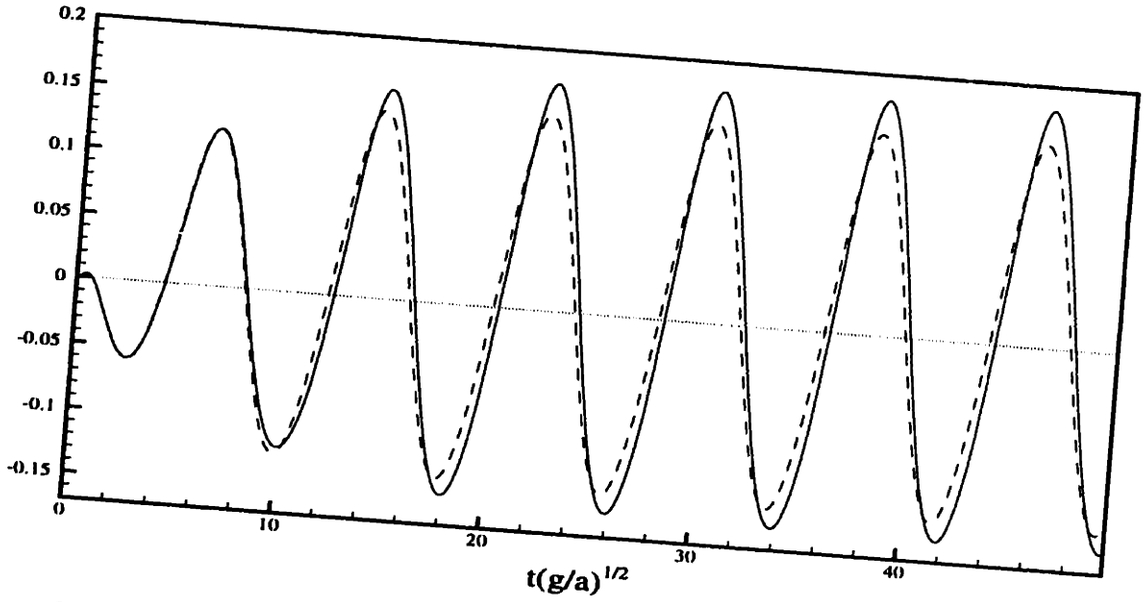

Figure 6-9: First- plus second-order surge force on the fixed sphere for a separation of $2d = 5$ (solid line) and for a single, isolated sphere (dashed line). Incident waves have wavenumber $Ka = 0.628$, $\theta = 180°$ and amplitude $\frac{A}{a} = 0.10$.

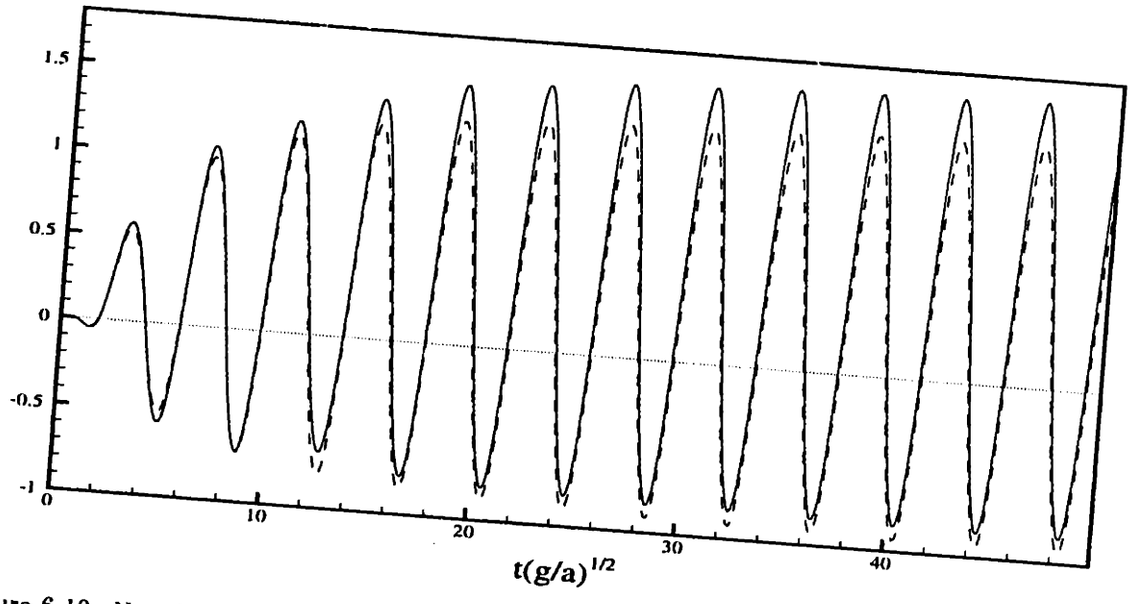

Figure 6-10: Non-dimensional second-order force, $\frac{F^q}{\rho g A^2}$, acting on fixed sphere for a separation of $2d = 5$ (solid line) and a single, isolated sphere (dashed line). Incident waves have wavenumber $Ka = 0.628$, $\theta = 180°$ and $\frac{A}{a} = 0.10$.

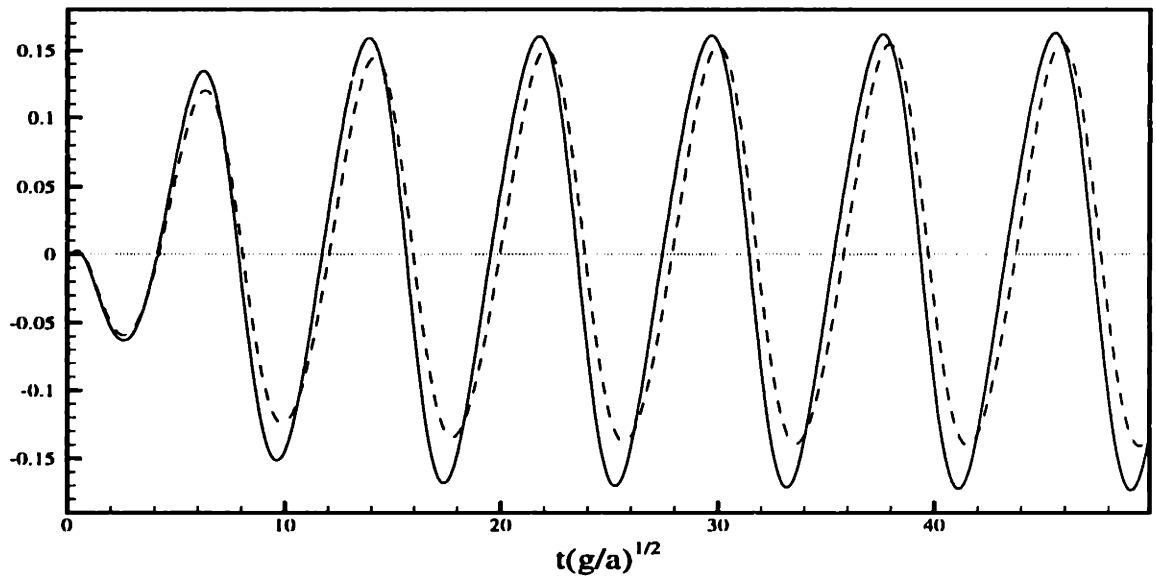

Figure 6-11: First- plus second-order surge force on the fixed sphere for a separation of $2d = 3$ (solid line) and for a single, isolated sphere (dashed line). Incident waves have wavenumber $Ka = 0.628$, $\theta = 180°$ and amplitude $\frac{A}{a} = 0.10$.

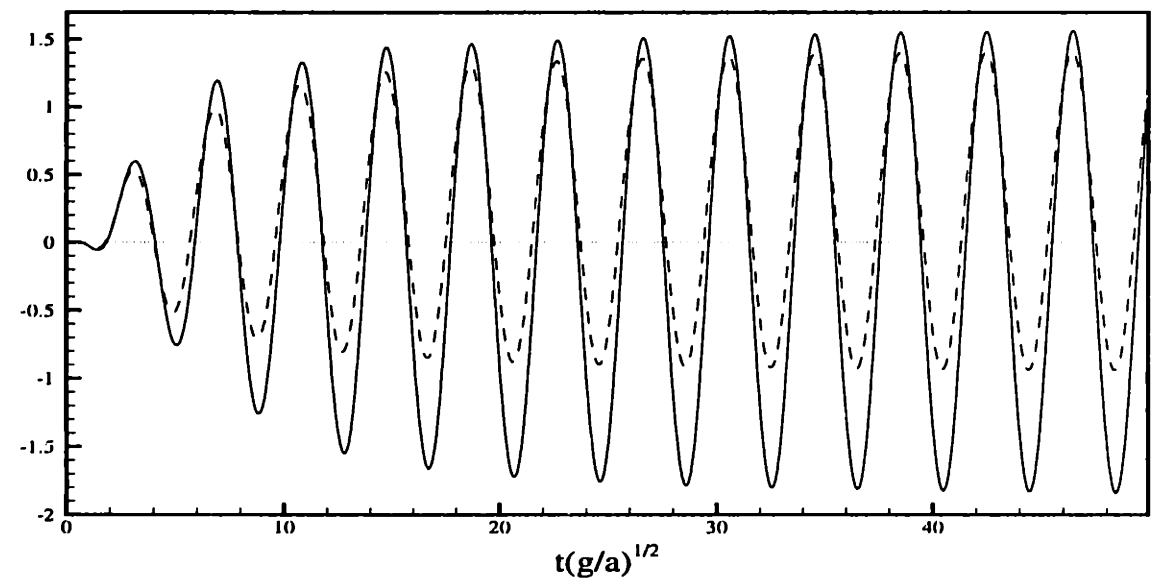

Figure 6-12: Non-dimensional second-order force, $\frac{F^q}{\rho g A^2}$, acting on fixed sphere for a separation of $2d = 3$ (solid line) and a single, isolated sphere (dashed line). Incident waves have wavenumber $Ka = 0.628$, $\theta = 180°$ and $\frac{A}{a} = 0.10$.

on the sphere if the distance to the cylinder is less than $2d = 4$. A simulation is performed with an initial separation distance of $2d = 3.5$, and Figure 6-14 shows the resulting horizontal motion of the sphere. The surge velocity is plotted in Figure 6-15. Low- and wave-frequency components of the motion arise naturally from the solution of the body-exact boundary value problem. Because of the phase of the incident waves, the initial momentum of the sphere is in the $+X$ direction. However, after approximately three wave periods, the sphere is repelled from the cylinder. Here, body-body interactions are strong enough to produce a slow upwave drift of the sphere, and support the earlier fully-linearized analysis.

Conjecture from frequency-domain analysis, however, does not always lead to the correct prediction of the slow drift motions. This may be illustrated by simulating the surge and heave of the sphere. Due to finite-amplitude vertical motions, the wetted surface of the sphere is re-discretized at every time step. Figure 6-13 shows typical discretizations of the sphere at three instants of time. The preliminary frequency-domain analysis of § 6.1 suggests that at $\frac{Kd}{\pi} = 0.50$ and $2d = 5$, the sphere will drift away from the cylinder. Figures 6-16 and 6-17 show, respectively, the surge motion and velocity of the sphere under these initial conditions. In this case, the negative drift force is not large enough to overcome the initial downwave momentum of the sphere, and the body slowly drifts with the waves until it collides with the cylinder.

When the $t = 0$ separation is increased to $2d = 6\left(\frac{Kd}{\pi} = 0.60\right)$, and the sphere is free to respond in heave and surge, the floating body assumes the motion plotted in Figure 6-18. Here, wave interference due to the cylinder is strong enough to repel the floating sphere. After initially drifting in the direction of the incident waves, the low-frequency velocity of the sphere changes sign. Presumably, the mean force would once again become positive if the simulation were continued, and the sphere would perform slow-drift oscillations.

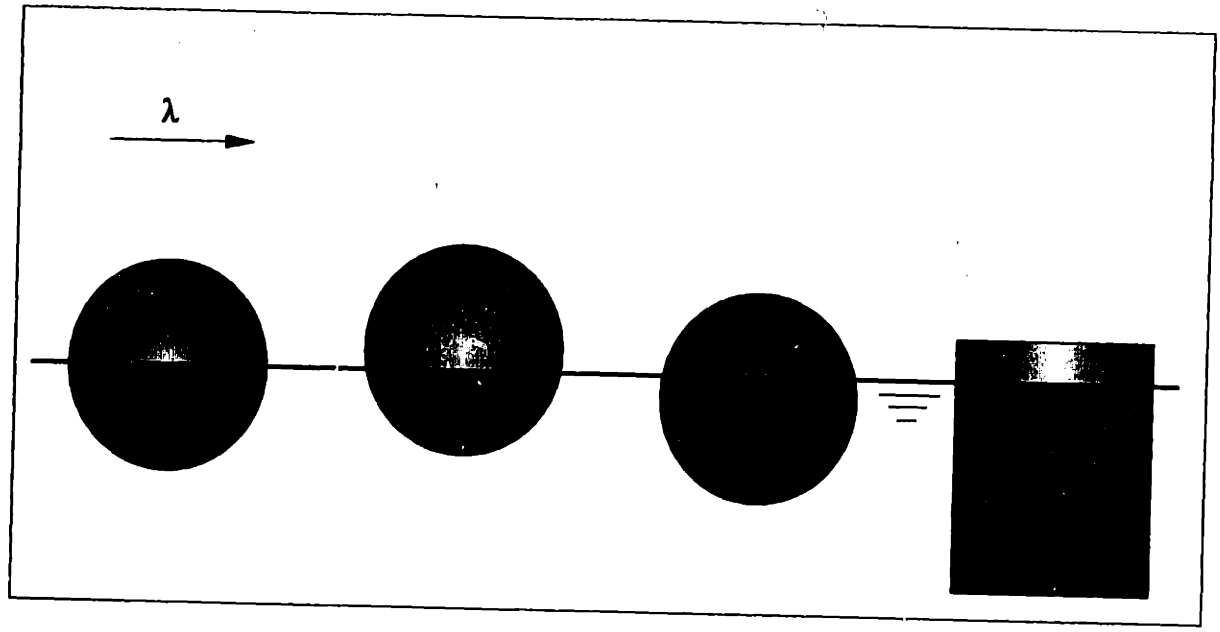

Figure 6-13: The two-body arrangement shown with the sphere in three different positions. Only the portions of the surfaces below $Z = 0$ are discretized.

6.4 The effect of wave-drift damping

The mean force on a floating body is known to be sensitive to its drift velocity. Physically, this is due to the difference in wave scattering about a fixed body and the same body undergoing slowly-varying drift motions. For bodies drifting in waves, the mean force is commonly expressed as

$$\bar{F} = D - \frac{\partial D}{\partial U_{\text{drift}}} U_{\text{drift}} = D - B U_{\text{drift}} \,, \tag{6.3}$$

where D is the mean drift force at zero-speed, B is the wave drift damping coefficient, and U_{drift} is the drift velocity of the body. The conventional analysis of the wave-drift damping is based on quasi-steady assumptions that allow multiple parameter expansions (Emmerhoff and Sclavounos [9]). The leading-order correction of the mean drift force is proportional to the square of the incident wave amplitude, and thus comparable in magnitude to the zero-speed drift force.

In the present case, we are studying a fundamentally different phenomenon: body-body interactions and their influence on the resulting motions. Nonetheless, a rough estimate of the wave-drift damping is made in order to determine its importance =

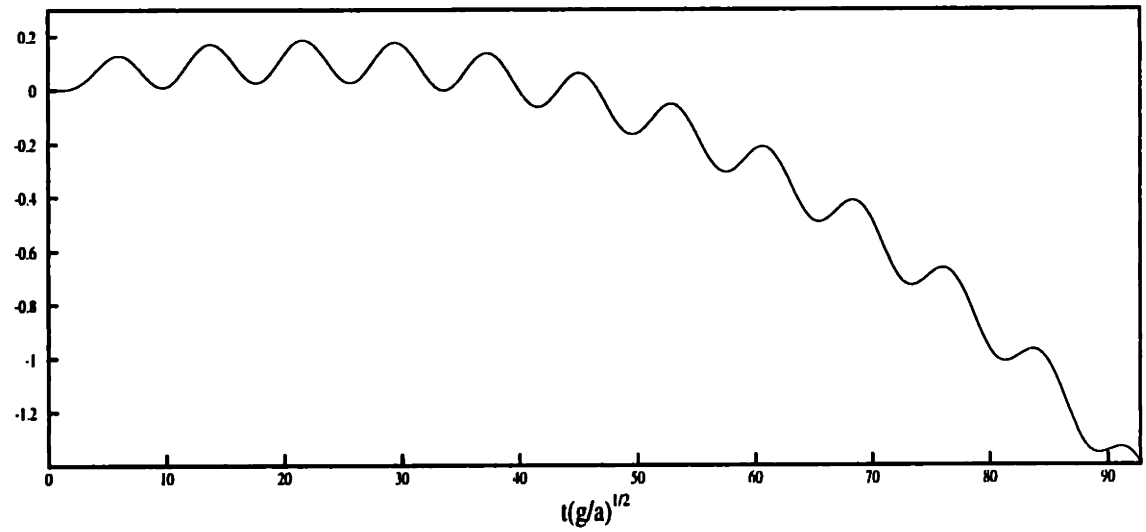

Figure 6-14: Horizontal motion of the floating sphere. Body is free in surge but fixed in heave. Incident waves are in the $+X$ direction. Initial distance to cylinder is $2d = 3.5$. $Ka = 0.628$, $\theta = 180°$, and $\frac{A}{a} = 0.10$

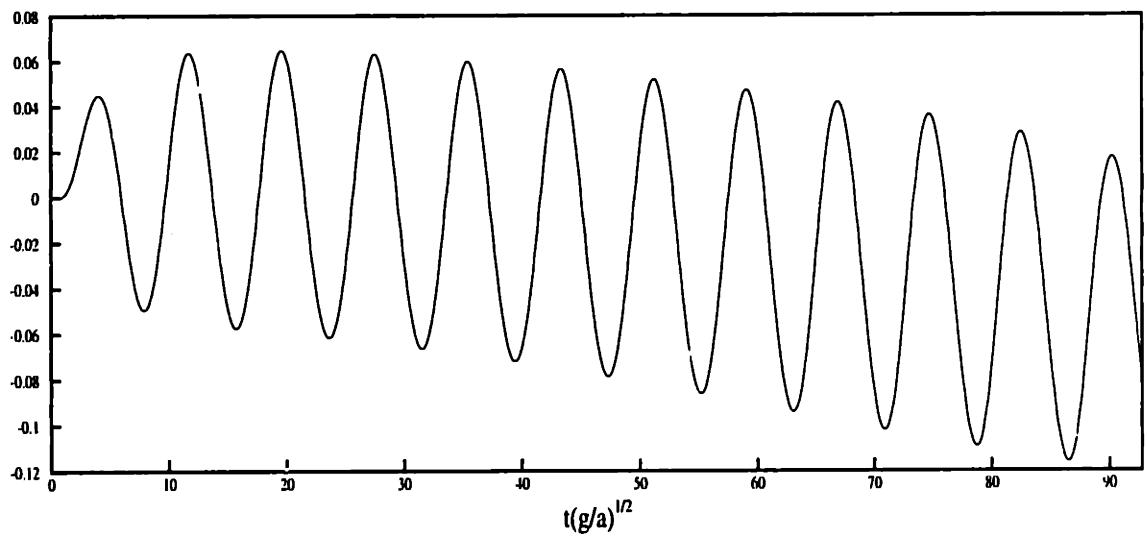

Figure 6-15: Horizontal velocity of the floating sphere. Body is free in surge but fixed in heave. Incident waves are in the $+X$ direction. Initial distance to cylinder is $2d = 3.5$. $Ka = 0.628$, $\theta = 180°$, and $\frac{A}{a} = 0.10$

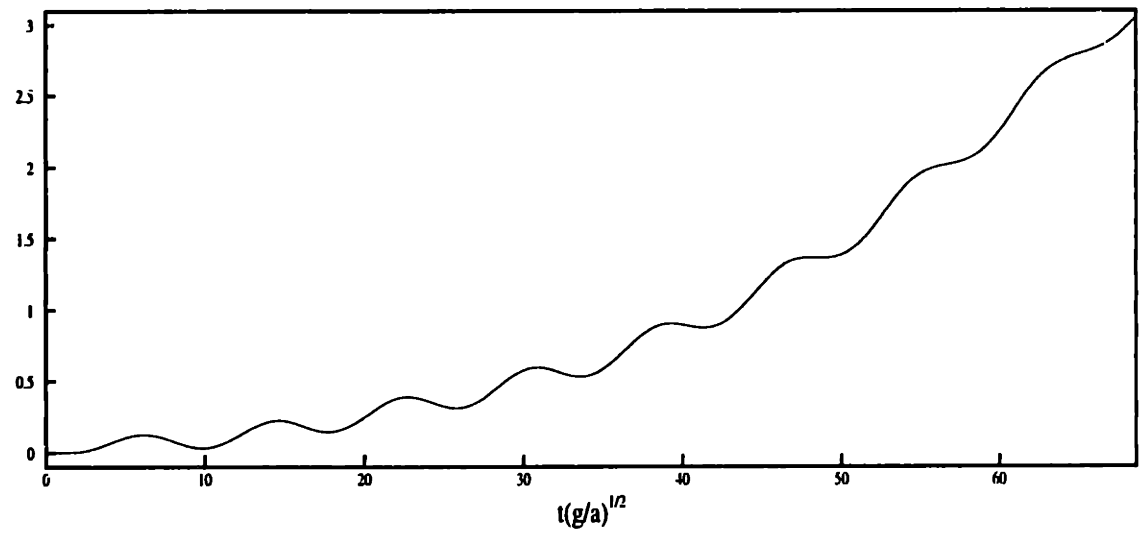

Figure 6-16: Horizontal motion of the floating sphere. Body is free in surge and heave. Incident waves are in the $+X$ direction. Initial distance to cylinder is $2d = 5$. $Ka = 0.628$, $\theta = 180°$, and $\frac{A}{a} = 0.10$

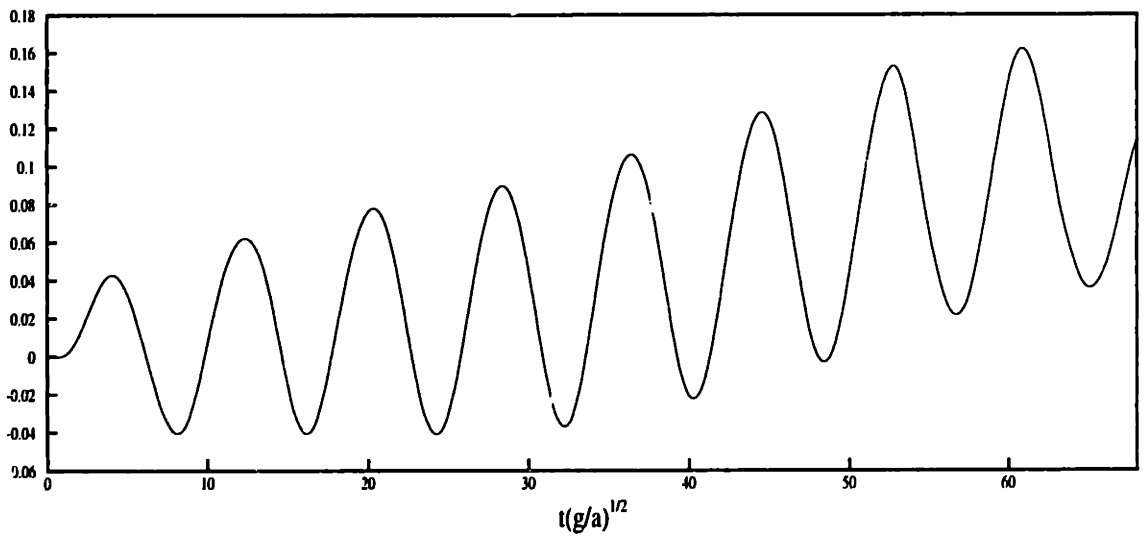

Figure 6-17: Horizontal velocity of the floating sphere. Body is free in surge and heave. Incident waves are in the $+X$ direction. Initial distance to cylinder is $2d = 5$. $Ka = 0.628$, $\theta = 180°$, and $\frac{A}{a} = 0.10$

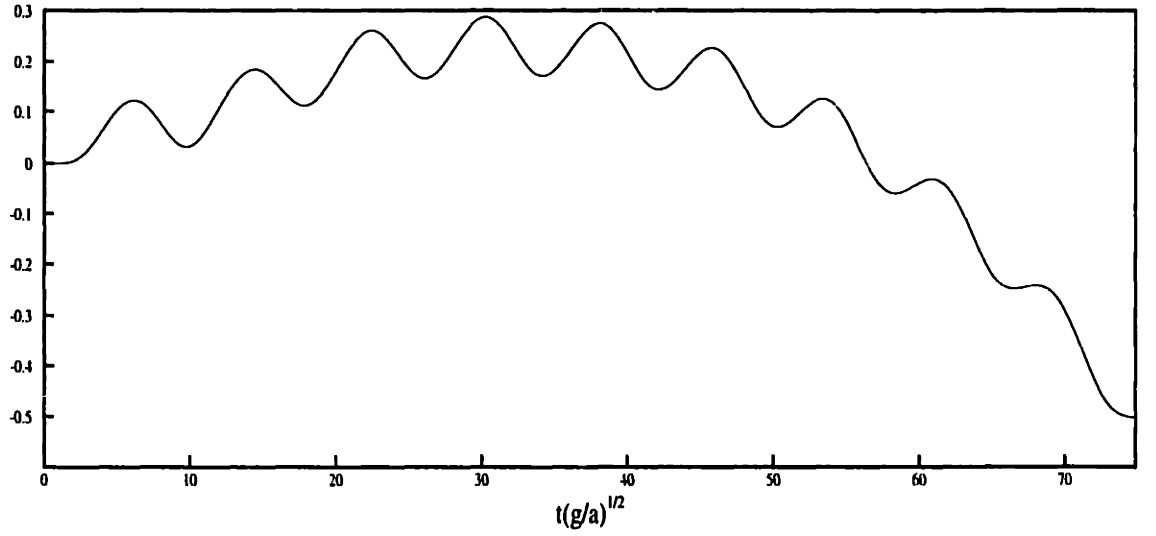

Figure 6-18: Horizontal motion of the floating sphere. Body is free in surge and heave. Incident waves are in the $+X$ direction. Initial distance to cylinder is $2d = 6$. $Ka = 0.628$, $\theta = 180°$, and $\frac{A}{a} = 0.10$

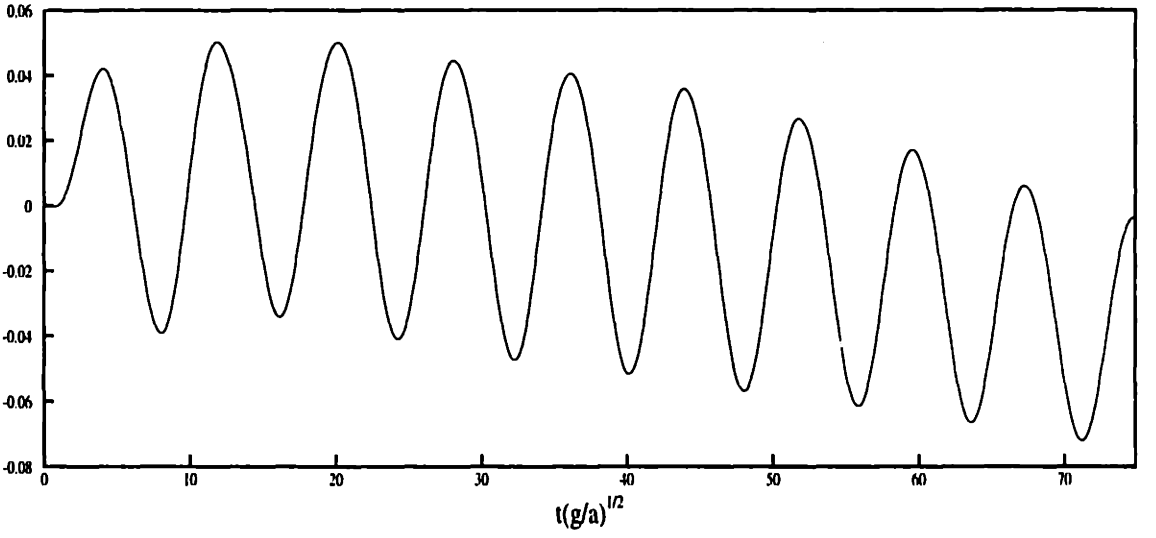

Figure 6-19: Horizontal velocity of the floating sphere. Body is free in surge and heave. Incident waves are in the $+X$ direction. Initial distance to cylinder is $2d = 6$. $Ka = 0.628$, $\theta = 180°$, and $\frac{A}{a} = 0.10$

in the present simulations. Using results for a single floating hemisphere from Nossen et. al. [47], the wave-drift damping coefficient for an isolated, single hemisphere restrained in surge is found to be $\frac{B}{\rho g A^2 a} = 1.25$. Comparing results of fixed and freely floating bodies, one observes that the wave-drift damping coefficient for floating bodies generally decreases by about 50%. Therefore, we use a value of $\frac{B}{\rho g A^2 a} = 0.625$ in estimating the effect of wave-drift damping on the sphere.

From HIPAN computations, the zero-speed mean drift force on a single, isolated hemisphere is $\frac{D}{\rho g A^2 a} = 0.244$. Table 6.1 shows the magnitude of wave-drift damping relative to the total mean force for a single hemisphere for a range of drift velocities. Considering the magnitude of the low-frequency velocity in the body-exact simulations, it is unlikely that wave-drift damping has a dominant effect.

Wave-drift damping of hemisphere	
U_{drift}	$\frac{BU_{\text{drift}}}{F}$
0.02	0.0487
0.04	0.0929
0.06	0.133
0.08	0.170

Table 6.1: The ratio of wave-drift damping to total mean force for a single, isolated hemisphere.

Chapter 7

The Response of Parametrically Excited Systems

The equations governing the motion of a floating body closely resemble those of a mechanical oscillator, although the presence of waves in the hydrodynamic system prevents a direct analogy. However, insight into the response of the body may be gained by examining linear and weakly nonlinear model equations of motion of an idealized mass-spring-dashpot system.

Perhaps the most common use of the linear equations of motion is in the determination of response amplitude operators and the natural frequencies of a floating body. Nonlinear extensions have been widely used to analyze the rolling motion of ships, as changes in the righting arm often lead to model equations that predict observed instabilities. Less publicized, and more general, mechanisms that lead to parametric forcing have been discussed by Rainey [52]. There, the *rates* of change of added-mass, damping, hydrostatic, or exciting forces with respect to displacement lead to a time-varying 'restoring' coefficients. Eatock Taylor and Knoop [8] used arguments put forth by Rainey to analyze the dynamic instability of an idealized ocean structure floating in waves.

As an example of the large-amplitude motion generated by parametric excitation, the body-exact solution from `HITIM` is used to simulate parasitic motions of floating bodies. Two structures are examined. In each case, we introduce approximations in

order to describe the response of the body by Mathieu's equation. Although the non-linear mechanisms in the two cases are physically different, both simulations display analogous instabilities. Approximations used to arrive at this parametrically-forced model equation are more restrictive than those associated with the formulation of the body-exact intimal boundary value problem of Chapter 2. However, the stability properties of Mathieu's equation are well known and help to explain the numerical simulations.

Although these instabilities only occur for a highly tuned system, the implications to real structures in the sea cannot be completely neglected. In a continuous spectrum, some wave energy will always be present at twice the natural frequency. If a mechanism for parametric forcing exists, the observed response of an offshore structure may be very different from what linear analysis predicts.

7.1 A mathematical model for dynamic instability

Assuming small-amplitude sinusoidal motion, the response of a floating body at steady state is governed by

$$M_v\ddot{\chi} + B\dot{\chi} + C\chi = \mathcal{F}(\omega_o, t)\,, \tag{7.1}$$

where χ is the displacement of the body, M_v is the virtual mass of the body, B is the damping coefficient due to wave radiation, C is the hydrostatic and gravitational restoring force coefficient, and $\mathcal{F}(\omega_o, t)$ represents the exciting force of frequency ω_o. The overdot denotes differentiation with respect to the time variable t. As the body responds to waves, a time-varying restoring coefficient may be justified. In this case, the model equation becomes

$$M_v\ddot{\chi} + B\dot{\chi} + [C + \delta\cos(\omega_o t)]\,\chi = \mathcal{F}(\omega_o, t)\,. \tag{7.2}$$

Non-negligible changes of the waterplane area provide the most obvious explanation for the periodic restoring coefficient, but this is not the only possible mechanism of

the parametric forcing [52].

The homogeneous part of (7.2) may be expressed in nondimensional terms as

$$\chi'' + \gamma\chi' + [\alpha + \beta\cos(\tau)]\ \chi = 0\ , \tag{7.3}$$

where,

$$\tau = \omega_o t \quad , \quad \gamma = \frac{B}{M_v\omega_o} \quad , \quad \alpha = \left(\frac{\omega_n}{\omega_o}\right)^2 \quad \text{and} \quad \beta = \frac{\delta}{M_v\omega_o^2}. \tag{7.4}$$

The natural frequency is defined as $\omega_n^2 = \frac{C}{M_v}$, and primes denote differentiation with respect to the variable τ. Introducing another change of variables, we arrive at the standard form of Mathieu's equation,

$$\xi'' + \left[\alpha - \frac{1}{4}\gamma^2 + \beta\cos(\tau)\right]\ \xi = 0\ , \tag{7.5}$$

where $\chi(\tau) = e^{-\frac{1}{2}\gamma\tau}\xi(\tau)$.

From Floquet theory, we know that stable solutions of (7.5) lie within certain regions of the $\alpha\beta$ plane (see Nayfeh [40] or Jordan [18]). Parameters that produce stable/unstable solutions are separated by curves on which solutions of the ordinary differential equation have a periodicity of $\tau = 2\pi$ or $\tau = 4\pi$. For undamped systems, the stability boundaries with solutions of period 4π lie at

$$\beta = 0 \quad \text{and} \quad \alpha_m = \frac{m^2}{4}\ , \text{ for } m = 1, 3, 5, \ldots. \tag{7.6}$$

Transition curves containing 2π solutions lie at

$$\beta = 0 \quad \text{and} \quad \alpha_n = n^2\ , \text{ for } n = 1, 2, 3, \ldots. \tag{7.7}$$

The qualitative features of these stability boundaries are shown in Figure 7-1.

Instabilities occur most often near $\alpha = 1/4$, where the excitation frequency is twice that of the natural response of the body. With this insight, we may design a wave-body simulation that is susceptible to unstable period doubling. This requires a physical mechanism for the parametric forcing to be present and have a frequency of twice the natural response.

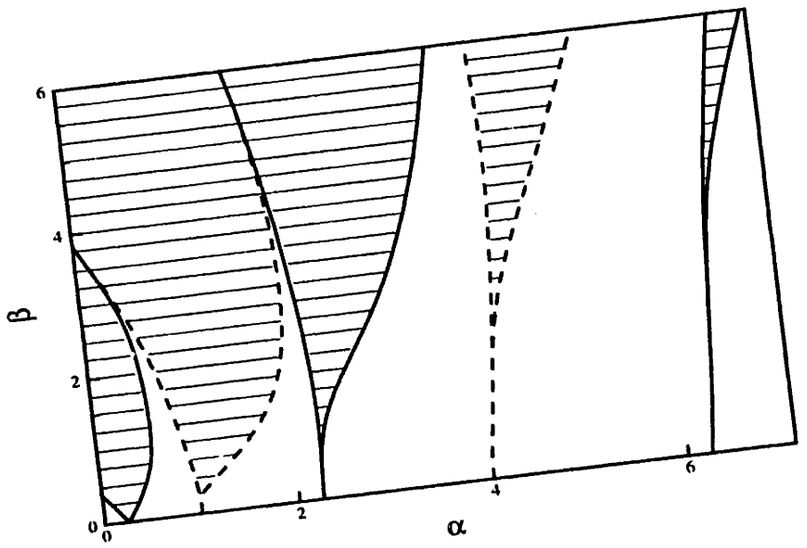

Figure 7-1: Qualitative stability diagram for the undamped Mathieu's equation. Unstable (shaded) regions are separated by boundaries along which solutions have a period of 2π (dashed lines) or 4π (solid line).

7.2 Parametric excitation from a hydrostatic mechanism

The need for a time-varying stiffness coefficient may be easily explained by changes in the waterplane area due to the motion of a floating body. At equilibrium, the hydrostatic restoring coefficients in the heave ($i = 3$) and pitch ($i = 5$) modes are

$$C_{33} = \rho g A_{\text{WP}} \tag{7.8}$$

and

$$C_{55} = \rho g \iint_{\mathcal{B}_0} x^2 n_3 dS - \rho g \mathcal{V}(z_{\text{cb}} - z_{\text{cg}}) \,, \tag{7.9}$$

where A_{WP} is the waterplane area, $\mathcal{V}$ is the volume of water displaced by the body, n_3 is the vertical component of the unit normal vector, and $z_{\text{cg,cb}}$ are the vertical centers of gravity and buoyancy with respect to the body-fixed origin. $\mathcal{B}_0$ is the body surface in its equilibrium position.

To introduce nonlinearities in the hydrostatic restoring forces, the spheroid shown in Figure 7-2 is chosen as a test body. The spheroid has a major radius of a and a minor radius of b. Its major axis is in the vertical direction, and the origin of the

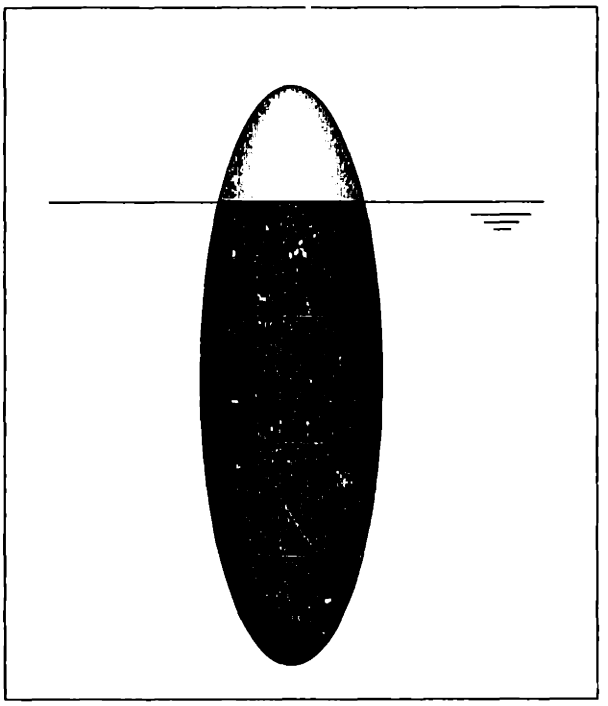

Figure 7-2: The spheroid with major radius a and minor radius b, is shown in its equilibrium position. $R_o = 0.060$, $a = 1$ and $b = 0.25$.

spheroid is submerged a distance R_o below the undisturbed free surface. Because of significant flare at the waterline, heave as well as pitch motions will lead to a time-varying hydrostatic coefficient. Our goal is to design a body that will simultaneously develop period doubling motions in both modes. This requires that the natural frequencies in heave and pitch coincide. We first determine the heave natural frequency, and then tune the pitch natural response.

Supposing the spheroid is in equilibrium for $R_o = 0.60$, the heave restoring coefficient and displaced fluid mass are $C_{33} = 0.126$ and $\rho\mathcal{V} = 0.235$. The heave-heave added-mass and damping coefficients are frequency domain quantities and plotted in Figure 7-3. From $\omega = 0.6$ to $\omega = 0.8$, $A_{33} \approx 0.0127$. Therefore, the heave natural frequency of the spheroid is approximately

$$\omega_{\text{heave}} = \sqrt{\frac{C_{33}}{\rho\mathcal{V} + A_{33}}} \approx \sqrt{\frac{0.126}{0.235 + 0.0127}} = 0.713\,. \tag{7.10}$$

The pitch-pitch added-mass and damping coefficients are shown in Figure 7-4, and $A_{55} = 0.0248$ at $\omega = 0.71$. For a vertical center of gravity of $x_{cg} = -0.40$, the

hydrostatic restoring force coefficient is $C_{55} = 0.0750$. The desired radius of gyration may be found by matching the pitch and heave natural frequencies.

$$\omega_{\text{pitch}} = \sqrt{\frac{C_{55}}{\rho \mathcal{V} r_{55}^2 + A_{55}}} = \omega_{\text{heave}} \,, \tag{7.11}$$

which gives a radius of gyration of

$$\begin{aligned} r_{55} &= \sqrt{\frac{1}{\rho \mathcal{V}} \left[\frac{C_{55}}{\omega_{\text{heave}}^2} - A_{55} \right]} \\ &\approx \sqrt{\frac{1}{0.235} \left[\frac{0.0750}{0.713^2} - 0.0248 \right]} = 0.723. \end{aligned} \tag{7.12}$$

With estimates of the heave and pitch natural frequencies in hand, we may now select incident waves which are likely to induce large-amplitude motions in both modes. Since $\omega_o \approx 2\omega_n$ at the first Mathieu instability, incident waves are chosen such that their wave period is

$$\frac{T_o}{\sqrt{g/a}} = \frac{2\pi}{\omega_o} = \frac{\pi}{\omega_n} = \frac{\pi}{0.713} = 4.41 \,. \tag{7.13}$$

The incident wave elevation and resulting heave and pitch motions of the spheroid are plotted in Figures 7-5 and 7-6. The ordinate of these figures is the non-dimensional time $t\sqrt{g/a}$. The $2T_o$ response quickly dominates the vertical motion of the spheroid. The pitch motion retains a noticeable response at the incident wave frequency for time less than 100 seconds, but this response is also dominated by the $2T_o$ component at large times. As expected, the amplitudes of these low-frequency heave and pitch oscillations grow exponentially.

From the Haskind relations, the wave damping is known to be proportional to the square of the exciting force. Therefore, bodies designed to have small exciting forces commonly experience a highly-tuned resonant motion (Newman [44]). In the present case, this is confirmed by the response amplitude operators shown in Table 7.1. Even though a fully linearized analysis predicts a large resonance, it is important to note that the unstable motions in the present simulation are due to a physically different mechanism.

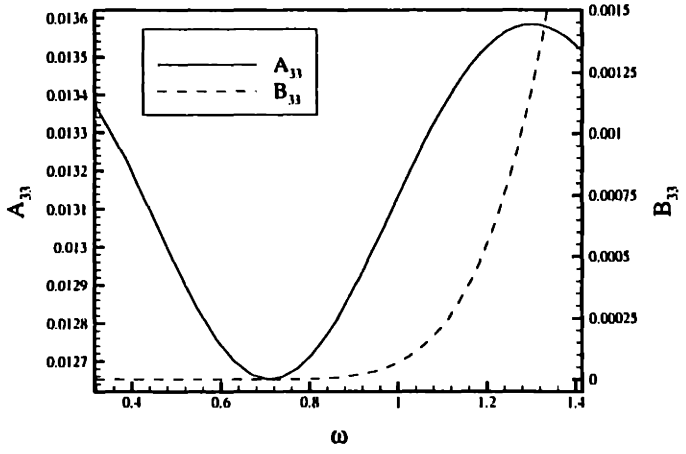

Figure 7-3: Heave-heave added-mass (solid line) and damping (dashed line) for the spheroid in its equilibrium position. Computations by **HIPAN**.

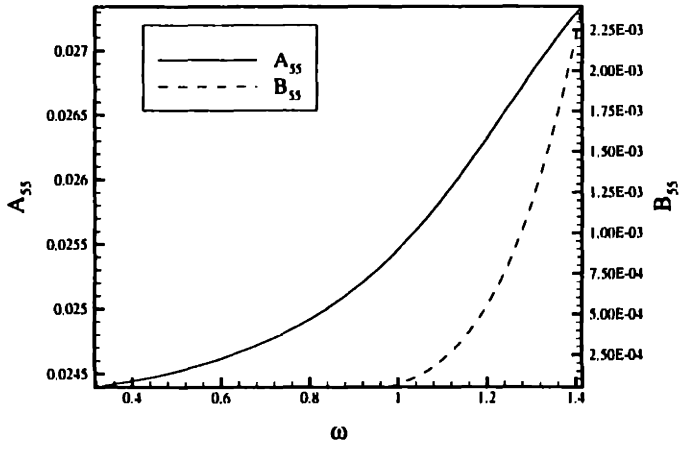

Figure 7-4: Pitch-pitch added-mass (solid line) and damping (dashed line) for the spheroid in its equilibrium position. Computations by **HIPAN**.

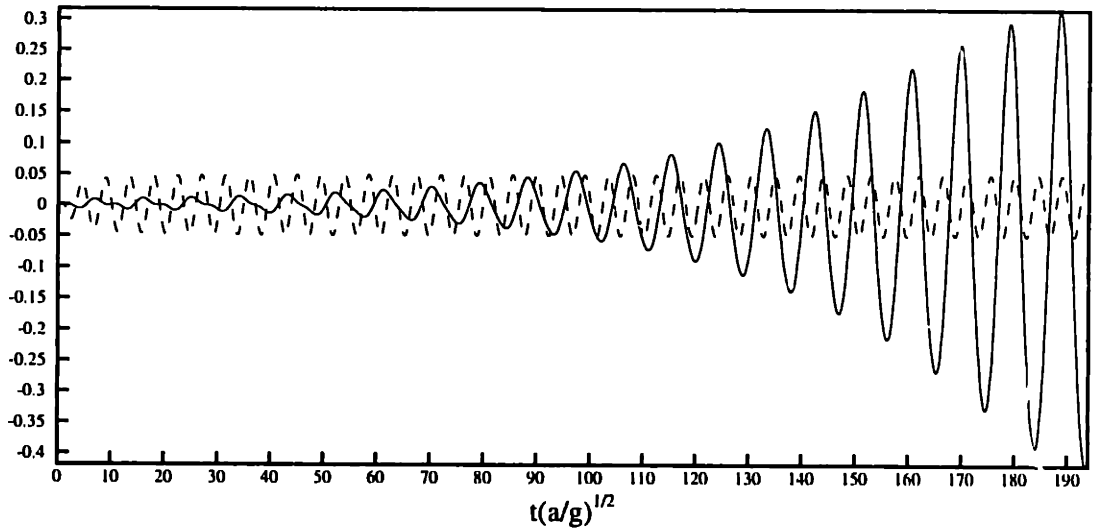

Figure 7-5: Heave motion of the spheroid (solid line) and the elevation of the incident waves (dashed line). Incident waves have period $T_o = 4.3$ and amplitude $\tilde{\eta} = 0.05$.

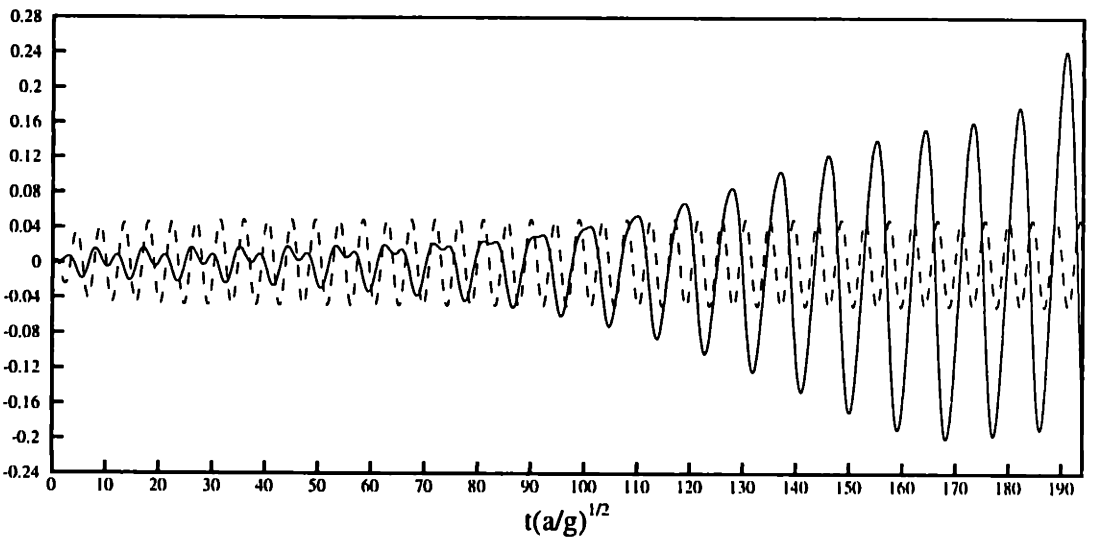

Figure 7-6: Pitch motion of the spheroid (solid line) and the elevation of the incident waves (dashed line). Incident waves have period $T_o = 4.3$ and amplitude $\tilde{\eta} = 0.05$.

Response Amplitude Operators of the Spheroid		
T_o	$\lvert\chi_3\rvert/\tilde{\eta}$	$\lvert\chi_5\rvert/\tilde{\eta}$
4.5	8.72×10^{-2}	2.46×10^{-1}
9.0	7.40	3.25

Table 7.1: The heave and pitch response amplitude operators for the freely floating spheroid. Results for sinusoidal motion at the wave and natural periods. $\tilde{\eta}$ is the amplitude of the incident waves. Computations by **HIPAN**.

7.3 Parametric excitation from a hydrodynamic mechanism

The periodic stiffness coefficient in the preceding example was easily explained by time-varying hydrostatic properties. We now present another mechanism which may provide the parametric forcing required for Mathieu-type instabilities. In this case, coupling between the exponential attenuation of vertical Froude-Krylov exciting forces and the first-order body motions leads to a subharmonic resonance at twice the wave period.

In order to preclude parametric excitation by hydrostatic means, we simulate the vertical translation of the body shown in Figure 7-7. The same flask shape was used in experiments by Rainey [52], and later by Eatock Taylor and Knoop [8]. A sphere of radius a is connected to a vertical circular neck of radius r. At rest, the center of the sphere is a distance $R_o = 2a$ below the undisturbed free surface. In this position, the heave-heave restoring coefficient and mass of displaced fluid are $\rho g A_{\mathrm{wp}} = 0.460$ and $\rho \mathcal{V} = 4.47$.

The equation for vertical translation of a floating body subject to long waves is

$$[\rho \mathcal{V} + A_{33}]\, \ddot{\chi}_3 + \rho g A_{\mathrm{wp}}\, \chi_3 = \mathcal{F}_3 \,, \tag{7.14}$$

where χ_3 and $\mathcal{F}_3$ are, respectively, the heave motion and vertical exciting force. An approximation for the wave loading at the instantaneous position of the body may

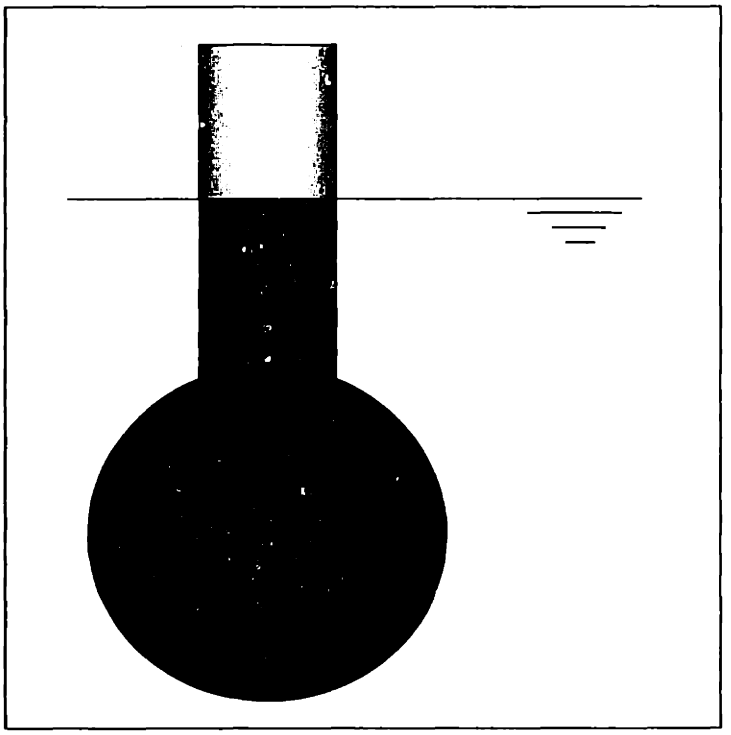

Figure 7-7: The submerged sphere of radius $a = 1$ attached to a circular vertical element of radius $r = 0.383$. At equilibrium $R_o = 2$.

be found by expanding the exciting force about the equilibrium position,

$$\mathcal{F}_3(\chi_3) = \mathcal{F}_3(0) + \frac{\partial \mathcal{F}_3}{\partial \chi_3}\Big|_{\chi_3=0} \chi_3 + \cdots \tag{7.15}$$

For axisymmetric bodies of large volume, the vertical exciting force due to long waves ($\lambda \gg a$) may be approximated as

$$\mathcal{F}_3(\chi_3) = [\rho \mathcal{V} + A_{33}]\, \dot{v} + \rho g A_{\text{wp}}\, \eta, \tag{7.16}$$

where v is the vertical component of the fluid velocity induced by the incident flow, and the incident wave elevation is $\eta = \tilde{\eta}\cos(\omega_o t)$. Because of the large volume and small waterplane area of the body, we have neglected the effects of damping but retained the mass force in the longwave approximation.

In deep water, the fluid motion has exponential attenuation in the vertical direction. Therefore, the exciting force on the body at its true position is

$$\mathcal{F}_3(\chi_3) = [\rho \mathcal{V} + A_{33}]\, \omega_o^2\, \eta\, e^{-\frac{\omega_o^2(h-\chi_3)}{g}} + \rho g A_{\text{wp}}\, \eta\ , \tag{7.17}$$

where h is some distance below the undisturbed free surface, and χ_3 is the vertical translation of the body. The rate of change of the wave load with depth, evaluated at the body's equilibrium position, is

$$\frac{\partial \mathcal{F}_3}{\partial \chi_3} = -[\frac{\rho \mathcal{V} + A_{33}}{g}]\,\omega_o^4\,\eta\,e^{-\frac{\omega_o^2 h}{g}}\ . \tag{7.18}$$

Substituting (7.18) and (7.15) into (7.14) gives a more correct model equation for motion of the body as it performs large-amplitude vertical translation.

$$[\rho \mathcal{V} + A_{33}]\,\ddot{\chi}_3 + \left[\rho g A_{\rm wp} - \frac{\partial \mathcal{F}_3}{\partial \chi_3}\right]\chi_3 = \mathcal{F}_3(0) \tag{7.19}$$

$$\ddot{\chi}_3 + \omega_{\rm n}^2[1 + \beta\cos(\omega_o t)]\,\chi_3 = \frac{\mathcal{F}_3(0)}{[\rho \mathcal{V} + A_{33}]}, \tag{7.20}$$

where

$$\beta = -\frac{1}{\omega_{\rm n}^2[\rho \mathcal{V} + A_{33}]}\frac{\partial \mathcal{F}_3}{\partial \chi_3} = \frac{\tilde{\eta}\rho A_{\rm wp}}{\rho \mathcal{V} + A_{33}}\left(\frac{\omega_o}{\omega_{\rm n}}\right)^4 e^{-\frac{\omega_o^2 h}{g}}\ . \tag{7.21}$$

the homogeneous part of (7.20) is Mathieu's equation, so instabilities are possible for $\omega_0 \approx 2\omega_{\rm n}$. In the present example, the parametric forcing comes from the rate of change of the heave exciting force with respect to the vertical body motion.

In order to select the incident waves that induce a dynamic instability, the natural frequency of the system must be found. The added-mass and damping coefficients are shown in Figure 7-8, which gives a value of $A_{33} = 1.84$ for excitation near $\omega \approx 0.27$. This coincides with the natural heave frequency since

$$\omega_{\rm n} = \sqrt{\frac{\rho g A_{\rm wp}}{\rho \mathcal{V} + A_{33}}} \approx \sqrt{\frac{0.460}{4.47 + 1.84}} = 0.270\ . \tag{7.22}$$

To induce large-amplitude motion, the body is forced with incident waves such that $\omega_o \approx 2\omega_{\rm n}$. Therefore, the incident wave period is

$$T_o\sqrt{g/a} = \frac{2\pi}{\omega_o} = \frac{\pi}{\omega_{\rm n}} = \frac{\pi}{0.270} = 11.6. \tag{7.23}$$

Figure 7-9 shows that even for waves of $\tilde{\eta} = 0.125$, the body has a dominant response at its natural period. As expected from (7.21), the strength of the nonlin-

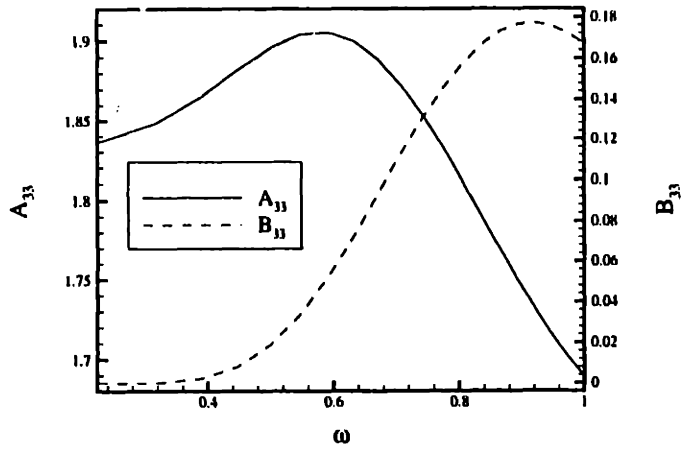

Figure 7-8: Heave-heave added-mass (solid line) and damping (dashed line) for the body shown in Figure 7-7 in its equilibrium position. Computations by **HIPAN**.

earity increases with the amplitude of the incident waves. The instability is more pronounced in the response to waves of $\tilde{\eta} = 0.200$, as seen in Figure 7-10.

In order to illustrate the difference between body-exact and linearized solutions, simulations are carried out in which the boundary value problem and pressure integration are defined over the equilibrium position of the body. Using this linearized formulation, we obtain the heave motion shown in Figure 7-11. Even though we are no longer solving the body-exact problem, energy at the natural frequency is introduced due to transients associated with beginning the simulation from a state of rest. For small values of time, the response is similar that of the body-exact simulation (see Figure 7-10). However, the $2T_o$ response is not unstable and presumably decays in amplitude due to the small amount of wave radiation generated by the body.

A nearly monochromatic response at the wave frequency may be obtained by prescribing initial conditions that minimize transients. Therefore, an initial displacement of

$$\chi_3 = \tilde{\eta} \times \mathrm{RAO}_3 = 0.20 \times 0.433 = 0.0866 \tag{7.24}$$

is chosen, and produces the time history shown in Figure 7-12. Clearly, the response contains less energy at natural frequency than the previous linearized simulation, and

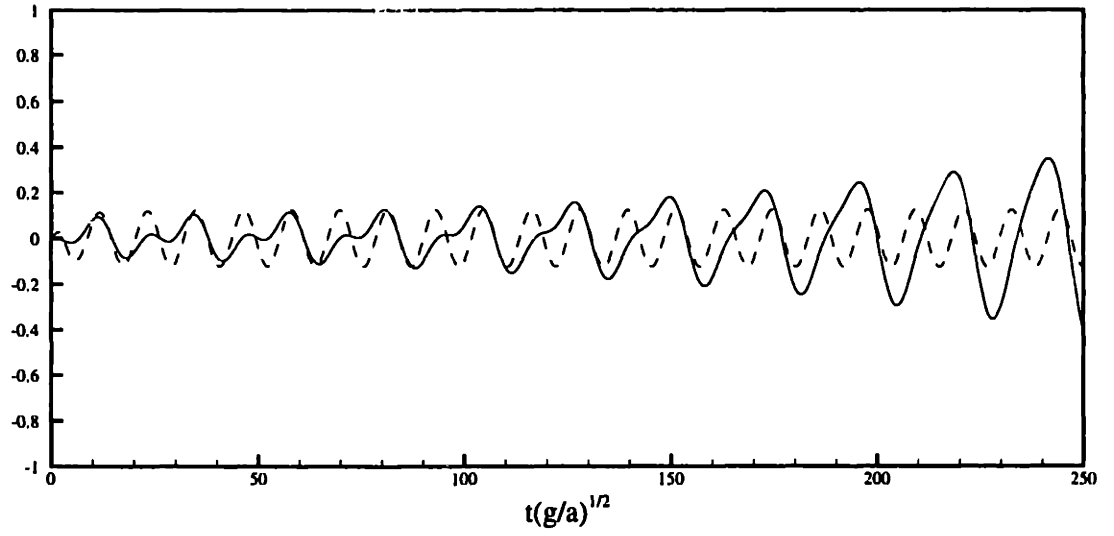

Figure 7-9: Heave motion of the body (solid line) when subject to waves of period $T_o = 11.6$ and $\tilde{\eta} = 0.125$ (dashed line).

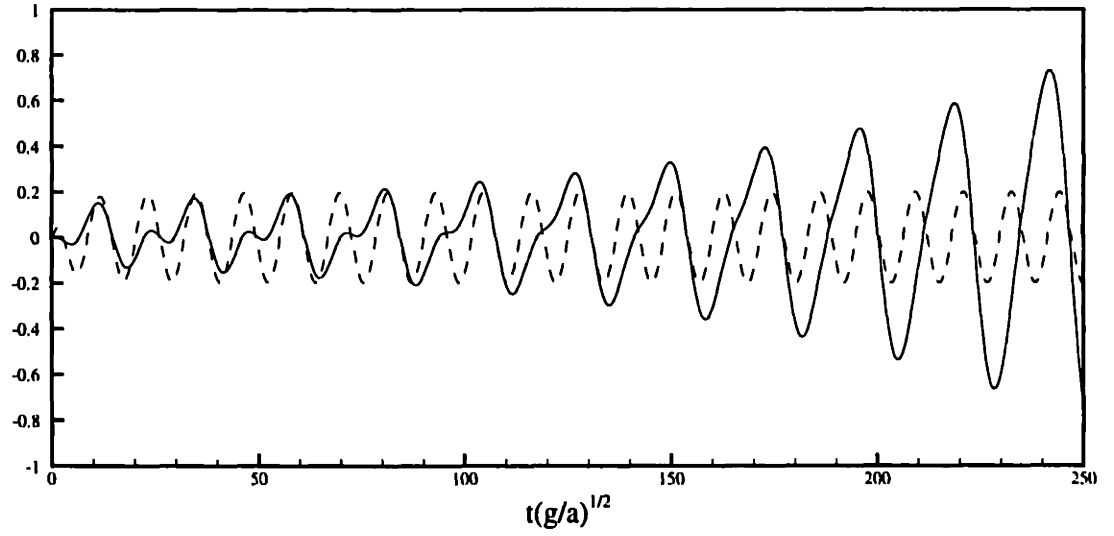

Figure 7-10: Heave motion of the body (solid line) when subject to waves of period $T_o = 11.6$ and $\tilde{\eta} = 0.200$ (dashed line).

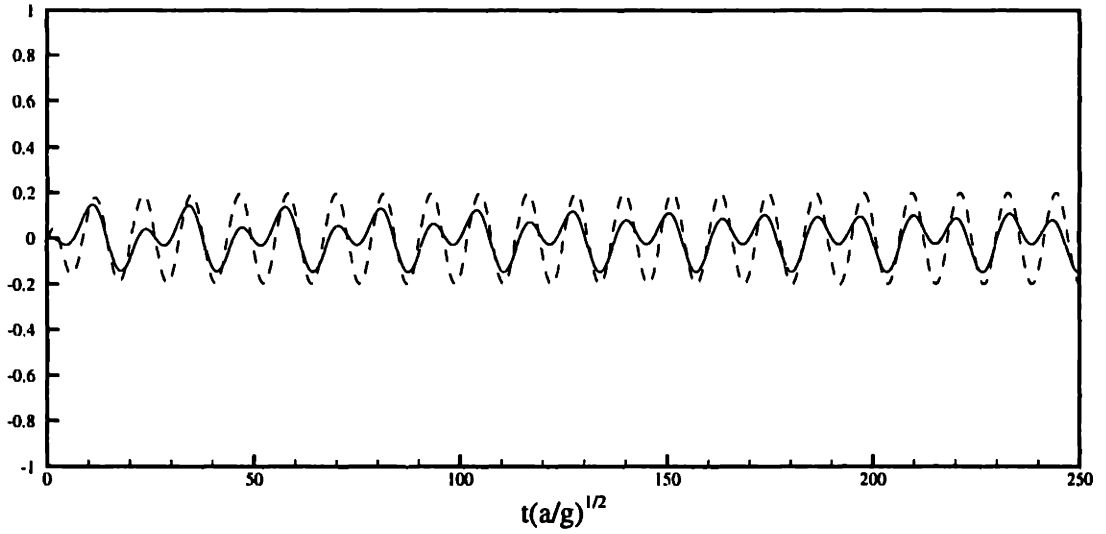

Figure 7-11: Heave motion of the body (solid line) when subject to waves of period $T_o = 11.6$ and $\tilde{\eta} = 0.200$ (dashed line). The initial boundary value problem and pressure integration are performed over the equilibrium position of the body. $\chi_3 = 0$ at $t = 0$.

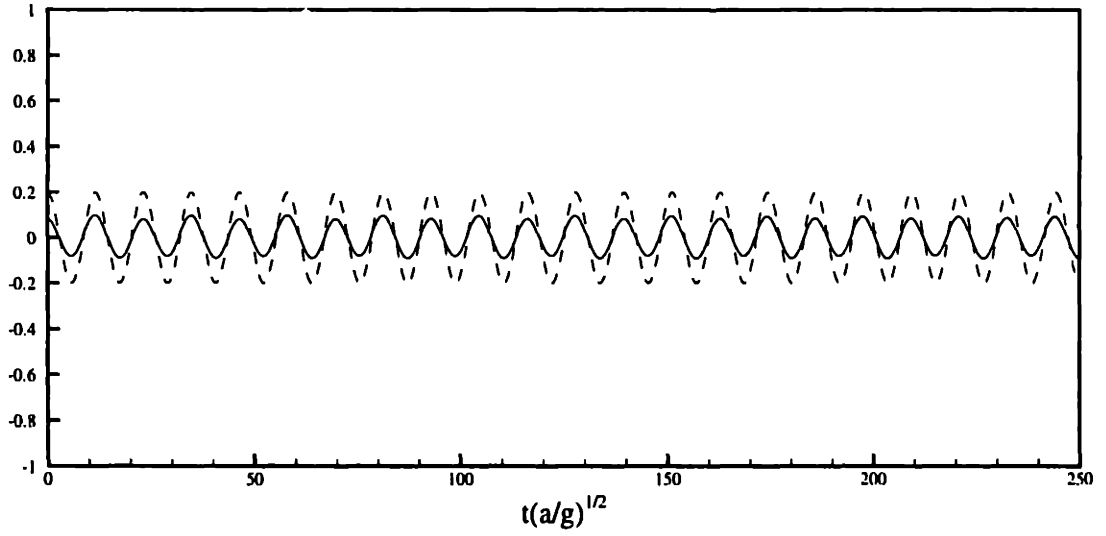

Figure 7-12: Heave motion of the body (solid line) when subject to waves of period $T_o = 11.6$ and $\tilde{\eta} = 0.200$ (dashed line). The initial boundary value problem and pressure integration are performed over the equilibrium position of the body. $\chi_3 \neq 0$ at $t = 0$.

the motion closely follows the incident waves.

The results above demonstrate the importance of using the body-exact formulation in simulating the response of this large-volume, small-waterplane structure. Parametric forcing, and hence the observed instability, are absent from linearized simulations. Clearly, free-surface nonlinearities will be important once the spherical flask broaches the $Z = 0$ plane. However, the body-exact treatment should correctly model the initiation of the Mathieu instability.

Chapter 8

Conclusions and Recommendations

A novel boundary element method has been developed to compute the potential flow about three-dimensional bodies undergoing finite-amplitude motions. In the present study, the body boundary condition is imposed without approximation, and disturbances at the free surface are assumed to be small enough to justify linearization. To solve this body-exact boundary value problem, we apply a new higher-order panel method that separates the hydrodynamic discretization from the geometric representation. The numerical algorithms presented in this thesis adopt a B-spline representation of the velocity potential, but *any* regular parameterization may be used to describe the body surface. This increases the flexibility of the method and allows for greater accuracy in the representation of the body surface, while maintaining the desirable characteristics of higher-order schemes. The application of this geometry-independent higher-order method to the body-exact problem introduces difficulties absent from fully linearized formulations. Most notable is the need to map the higher-order discretization of the velocity potential to a time-varying wetted surface. Surface trimming and interpolation algorithms have been developed for this purpose, and successfully applied to various forms.

Traditional lower-order panel methods describe the body surface by a collection of planar quadrilateral elements, with a piecewise constant distribution of the potential. This requires many elements for the solution of large wave-body problems, and

special attention is required when derivatives of the potential are needed. Higher-order boundary element methods provide a *continuous distribution* of the potential over *curved surfaces.* Superiority of the higher-order schemes over the conventional constant-strength planar-panel method in accurately evaluating gradients of the potential and solving computationally intensive problems has been widely reported [36, 25, 48, 19].

Since any parametric representation of the surface is allowed, complex shapes may be accurately described by computer aided design tools, or analytic definitions may be used to produce error-free geometric models of simple bodies and idealizations of real ocean structures. In either case, the description of the surface may be generated without regard to the hydrodynamic flow. This geometry-independent approach has obvious advantages over panel methods that build a hydrodynamic grid based upon the geometric model. Firstly, a very accurate (and even exact) representation of the surface may be generated. Secondly, various discretizations of the potential may be consistently applied over the same geometric model. Therefore, meaningful methods of adaptive error control may be derived since the hydrodynamic discretization may be refined over the *same* geometric surface.

Our choice of basis functions in the representation of the potential provides for analytic differentiation of the solution. This is of particular importance in the computation of second-order forces from quadratic interactions of the first-order solution. In addition, the continuity inherent in the B-spline discretization of the velocity potential produces a computationally efficient method, as demonstrated in Chapter 3. Reducing the number of unknowns in the resulting linear system of equations is particularly beneficial in the present case, because of the high numerical cost associated with obtaining a body-exact solution.

The first task of the algorithms described in Chapter 3 is to solve what is essentially a surface-surface intersection problem. At every time step, the hydrodynamic grid

must be properly mapped to that portion of the geometry that lies below the mean free surface. The combination of an implicit algebraic surface (the mean free surface) with a regular parametric surface (the body surface) makes this intersection problem well suited for marching algorithms. Such a scheme has been implemented in the present program in order to trace the waterline in parametric space. A bi-linear Gordon-Coons interpolation and the original parameterization of the body surface are then used to map the potential B-splines to physical space.

A solution to the integral equation is obtained via a Galerkin approach. The success of a similar higher-order panel method, based wholly on B-splines, was demonstrated in the thesis of Maniar [36]. There, B-spline representations of the body surface and velocity potential were used in the solution of the linear wave-body problem in the frequency domain. Quadrature schemes similar to those developed by Maniar, and later applied by Lee et. al. [24], have been adopted in the present geometry-independent higher-order method.

The robustness and accuracy of our method has been demonstrated by its application to the body-exact initial boundary value problem. Previous body-exact studies focused on conventional naval applications, specifically the heave and pitch motions of ships with forward speed [16, 29, 33]. The examples presented in Chapters 5, 6, and 7 include the computation of mean forces on a submerged body, the hydrodynamic interactions between multiple bodies, and instabilities of floating ocean structures. In these cases, disturbances at the free surface are expected to be small enough to justify linearization, and the body-exact solution should retain the dominant features of the flow. Since the body-exact formulation is linear but time-varying, nonlinearities in the numerical results come from second-order forcing due to the first-order potential, or the parametric influence of body position on the solution.

The first application involves the evaluation of wave-induced loads on a near-surface submarine. The mean vertical force and trim moment on the vessel have

been shown to strongly depend on the submergence. Transients are observed as the vessel approaches periscope depth, complicating the control of the body as it nears the free surface. Body-exact simulations have been used to numerically tune the parameters of a standard controller and arrive at a successful autopilot for the submarine. This allows for the computation of hydrodynamic loads on the submarine while the vessel responds to waves during the maneuver, and is more complete than an ad hoc construction of a simulation using steady-state results computed with the vessel at various levels of submergence.

Next, the body-exact formulation has been used to study the motions of a floating sphere that drifts in the vicinity of a fixed cylinder. The mean forces on the bodies have been shown to be sensitive to the spacing to wavelength ratio, and an upwave drift of the sphere exists for certain conditions. The features of the sphere-cylinder arrangement are illustrative of interactions that are present in more general multi-body problems. Here, the time-varying linear boundary value problem is sufficient for capturing the mean horizontal force that acts to repel the floating body upwave and away from the fixed structure.

Finally, dynamic instabilities of floating bodies have been observed by accounting for the finite amplitude of the body motions. Parametric forcing from hydrostatic and hydrodynamic mechanisms was shown to induce period doubling and exponentially large body motions. A simple model equation was introduced in order to explain the structure of the more complete numerical simulations. Practical implications of this Mathieu-type instability are important, since real ocean structures subject to the same parametric forcing may have an unexpectedly large response at the natural frequency even though little wave energy may exist at that particular frequency.

The geometric trimming and mapping schemes developed in the present thesis could be applied to solve other formulations of the wave-body problem. One possibility is to apply the geometry-independent higher-order approach to the Rankine

solution of problems with free-surface nonlinearities. There, the accuracy of higher-order schemes will lead to a robust code, and acceleration techniques such as the pre-corrected FFT have the promise of reducing the computational costs associated with the increased number of panels.

Appendix A

The Earth-Fixed Integral Equation

The body-exact boundary value problem is

$$\nabla^2\Phi(\mathbf{X},t) = 0 \quad \text{in} \quad \mathcal{V} \tag{A.1}$$

$$\Phi_{tt} + g\Phi_z = 0 \quad \text{on} \quad \mathcal{F} \tag{A.2}$$

$$\nabla\Phi\cdot\mathbf{n} = (\mathbf{U}-\nabla\varphi)\cdot\mathbf{n} \quad \text{on} \quad \mathcal{B}(\mathrm{t}) \tag{A.3}$$

$$\nabla\Phi \rightarrow 0 \quad \text{at} \quad \mathcal{S}_\infty \tag{A.4}$$

$$\Phi = \Phi_t = 0 \quad \text{on} \quad \mathcal{F}(\mathrm{t}=0) \tag{A.5}$$

where $\mathcal{V}$ is the volume of fluid bounded by the body surface ($\mathcal{B}$), the air/water interface ($\mathcal{F}$), and an imaginary surface at infinity ($\mathcal{S}_\infty$). $\mathbf{U}$ is the local velocity of the body surface, and φ is the incident potential.

For any field point $P=(x,y,z,t)$ and source point $Q=(\xi,\eta,\zeta,\tau)$, the transient Green function satisfying the above boundary value problem (excluding the body boundary condition) may be found in Wehausen and Laitone [56] or Stoker [53], and is

$$\begin{aligned} G(P,Q,t-\tau) &= G^o + H \\ &= \frac{1}{r} - \frac{1}{r'} + 2\int_0^\infty \left[1-\cos\left(\sqrt{gk}(t-\tau)\right)\right] e^{k(z+\zeta)} J_o(k\bar{R})\,dk \end{aligned} \tag{A.6}$$

where,

$$r = |P-Q| = [(x-\xi)^2+(y-\eta)^2+(z-\zeta)^2]^{1/2} \tag{A.7}$$

$$r' = |P - Q'| = [(x-\xi)^2 + (y-\eta)^2 + (z+\zeta)^2]^{1/2} \tag{A.8}$$

$$R = [(x-\xi)^2 + (y-\eta)^2]^{1/2}. \tag{A.9}$$

The body-exact boundary value problem is cast into an integral equation by two applications of Green's theorem. First, assume $\mathcal{S}_p$ to be an infinitesimally small surface surrounding the field point P. Applying Green's second identity to the velocity potential and G_t gives,

$$\iiint_{\mathcal{V}} \left(\Phi \nabla^2 G_\tau - G_\tau \nabla^2 \Phi\right) dV = \iint_{\mathcal{S}_p + \mathcal{F} + \mathcal{B} + \mathcal{S}_\infty} \left(\Phi G_{\tau n_Q} - G_\tau \Phi_{n_Q}\right) dS = 0. \tag{A.10}$$

The integrals over $\mathcal{S}_\infty$ and $\mathcal{S}_p$ do not have any contributions, so the surface integrals only have contributions from the free surface and body surface. Now integrate over the past time history,

$$\int_0^t d\tau \iint_{\mathcal{F}+\mathcal{B}} \left(\Phi G_{\tau n_Q} - G_\tau \Phi_{n_Q}\right) dS = 0. \tag{A.11}$$

The Green function and potential both satisfy the free-surface boundary condition. Therefore, the integral over $\mathcal{F}$ may be rewritten as:

$$\begin{aligned} \iint_{\mathcal{F}} \left(\Phi G_{\tau n_Q} - G_\tau \Phi_{n_Q}\right) dS &= -\frac{1}{g} \iint_{\mathcal{F}} (\Phi G_{\tau\tau\tau} - G_\tau \Phi_{\tau\tau})\, dS \\ &= -\frac{1}{g} \iint_{\mathcal{F}} \frac{\partial}{\partial \tau} \left[\Phi G_{\tau\tau} - G_\tau \Phi_\tau\right] dS. \end{aligned} \tag{A.12}$$

Using the Transport theorem, the temporal differentiation may be moved outside of the integral,

$$\begin{aligned} &-\frac{1}{g} \iint_{\mathcal{F}} \frac{\partial}{\partial \tau} \left[\Phi G_{\tau\tau} - G_\tau \Phi_\tau\right] dS = \\ &-\frac{1}{g} \frac{\partial}{\partial \tau} \iint_{\mathcal{F}} \left[\Phi G_{\tau\tau} - G_\tau \Phi_\tau\right] dS + \frac{1}{g} \int_\Gamma \left[\Phi G_{\tau\tau} - G_\tau \Phi_\tau\right] \mathbf{U} \cdot \mathbf{n}_{2D} dL, \end{aligned} \tag{A.13}$$

where $\mathbf{n}_{2D}$ the two-dimensional unit normal vector in the horizontal plane, and Γ is the waterline curve. Substituting (A.13) into (A.11), and using the initial conditions on the free surface gives,

$$\begin{aligned} &\iint_{\mathcal{F}} \Phi G^o_\zeta dS + \int_0^t d\tau \iint_{\mathcal{B}} (\Phi G_{\tau n_Q} - G_\tau \Phi_{n_Q}) dS \\ &+\frac{1}{g} \int_0^t d\tau \int_\Gamma (\Phi G_{\tau\tau} - G_\tau \Phi_\tau) \mathbf{U} \cdot \mathbf{n}_{2D} dL = 0. \end{aligned} \tag{A.14}$$

The second application of Green's second identity involves Φ and G^o in $\mathcal{V}$,

$$\iiint_{\mathcal{V}} \left(\Phi \nabla^2 G^o - G^o \nabla^2 \Phi\right) dV = \iint_{\mathcal{F}+\mathcal{B}+\mathcal{S}_p+\mathcal{S}_\infty} \left(\Phi G^o_{n_Q} - G^o \Phi_{n_Q}\right) dS \qquad \text{(A.15)}$$

There is no contribution from $\mathcal{S}_\infty$ or G^o over the free-surface, but the integration of Rankine terms over $\mathcal{S}_p$ is 2π. Therefore, the above equation reduces to

$$2\pi\Phi + \iint_{\mathcal{B}} \left(\Phi G^o_{n_Q} - G^o \Phi_{n_Q}\right) dS + \iint_{\mathcal{F}} \Phi G^0_\zeta dS = 0. \qquad \text{(A.16)}$$

The integral over the free surface may be canceled by adding (A.14) and (A.16). This gives an integral equation which only contains contributions from the body surface,

$$2\pi\Phi + \iint_{\mathcal{B}} (\Phi G^o_{n_Q} - G^o \Phi_{n_Q}) dS = \int_0^t d\tau \iint_{\mathcal{B}} (\Phi G_{\tau n_Q} - G_\tau \Phi_{n_Q}) dS + \qquad \text{(A.17)}$$
$$\frac{1}{g} \int_0^t d\tau \int_\Gamma (\Phi G_{\tau\tau} - G_\tau \Phi_\tau) \mathbf{U} \cdot \mathbf{n}_{2D} dL.$$

Appendix B

The Gordon-Coons Interpolation

The parameterization $\mathbf{X} = \mathbf{X}(u, v)$ is assumed to be regular over a 'patch' of the complete body. However, the boundary value problem is defined only over that portion of the surface below $Z = 0$. Let the parametric space that corresponds to this wetted hull surface be defined as $(u, v)_{\text{wet}}$. We now describe a procedure by which a computational domain, the st unit square, may be mapped to $(u, v)_{\text{wet}}$.

Our approach in discretizing the wetted surface involves two main steps. First, the marching algorithm of § 3.1.1 is used to solve the surface-surface intersection problem and define the waterline in (u, v) space. Then, the potential B-splines are mapped from their square computational domain to wet parametric space. This is done by developing the interior $(u, v)_{\text{wet}}$ from its boundary curves. The method used presently is credited to Coons [4], but it was given a mathematical foundation by Gordon [12]. The description of the Gordon-Coons interpolation scheme given below, follows that of Hoschek [14].

We wish to establish a mapping function from a square computational space, the st unit square, to the wet parametric surface; i.e.

$$(u, v)_{\text{wet}} = \mathbf{F}(s, t). \tag{B.1}$$

The portion of the (u, v) plane that corresponds to the wetted body surface is defined by four boundary curves, each of which are parameterized by their arclength. A typical boundary of $(u, v)_{\text{wet}}$ is shown in Figure B-1.

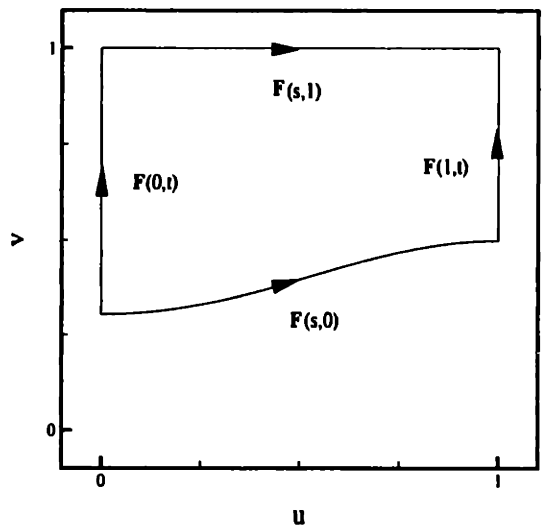

Figure B-1: The wet uv domain enclosed by the four boundary curves: $\mathbf{F}(s,0)$, $\mathbf{F}(0,t)$, $\mathbf{F}(s,1)$, and $\mathbf{F}(1,t)$.

The first step is to interpolate between the $t = 0, 1$ boundaries. We define the interpolation function $\mathbf{P_1F}(s,t)$ such that

$$\mathbf{P_1F}(s,t) = f_0(t)\mathbf{F}(s,0) + f_1(t)\mathbf{F}(s,1), \tag{B.2}$$

where the two blending functions are

$$f_0(\chi) = (1-\chi) \quad \text{and} \quad f_1(\chi) = \chi. \tag{B.3}$$

Other Hermite polynomials may be chosen, but the linear blending function above will be adequate for our purposes. A graphical interpretation of the $\mathbf{P_1F}$ interpolation is shown in Figure B-2. Next, the blending functions are used to interpolate between the two $s = 0, 1$ boundaries,

$$\mathbf{P_2F}(s,t) = f_0(s)\mathbf{F}(0,t) + f_1(s)\mathbf{F}(1,t). \tag{B.4}$$

This is shown graphically in Figure B-3.

If the boundary curves are not straight lines, the above interpolations will introduces errors. For example, Figure B-4 shows error produces by the $\mathbf{P_2}$ interpolation

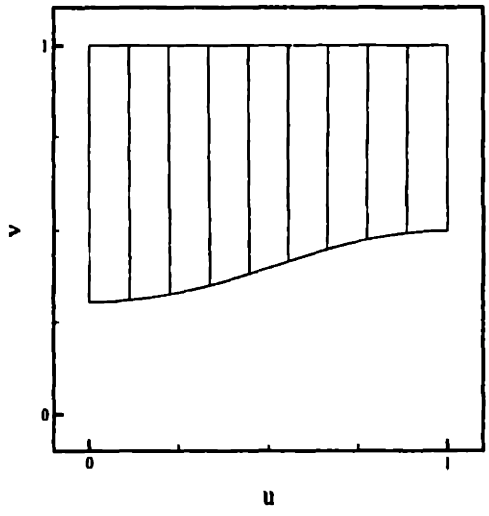

Figure B-2: P_1 interpolation of the uv_{wet}.

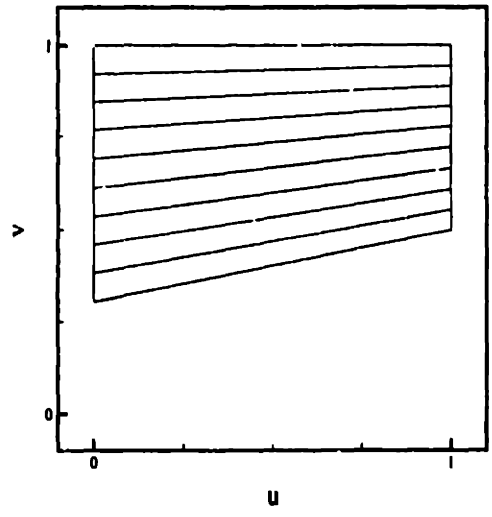

Figure B-3: P_2 interpolation of the uv_{wet}.

at the $t = 1$ boundary. We may define this precisely as

$$\mathbf{F}(s,1) - [f_0(s)\mathbf{F}(0,1) - f_1(s)\mathbf{F}(1,1)] \tag{B.5}$$

or, symbolically, as

$$\mathbf{F} - \mathbf{P_2F}. \tag{B.6}$$

A correction should be applied at the $t = 0, 1$ boundaries and every straight line defined by the $\mathbf{P_1F}$ operation,

$$\mathbf{P_1}(\mathbf{F} - \mathbf{P_2}) = \mathbf{P_1F} - \mathbf{P_1P_2F}. \tag{B.7}$$

The interior surface is the sum of the $\mathbf{P_2F}$ interpolation and (B.7),

$$\mathbf{F}(s,t) = \mathbf{P_1F} + \mathbf{P_2F} - \mathbf{P_1P_2F}, \tag{B.8}$$

or

$$\mathbf{F}(s,t) = (1-t)\mathbf{F}(s,0) + t\mathbf{F}(s,1) + (1-s)\mathbf{F}(0,t) + s\mathbf{F}(1,t) \tag{B.9}$$
$$-[(1-s)((1-t)\mathbf{F}(0,0) + t\mathbf{F}(0,1)) + s((1-t)\mathbf{F}(1,0) + t\mathbf{F}(1,1))].$$

From the above expression, it is evident that the surface defined in the Gordon-Coons interpolation is the combination of two linear interpolations and a corrections that

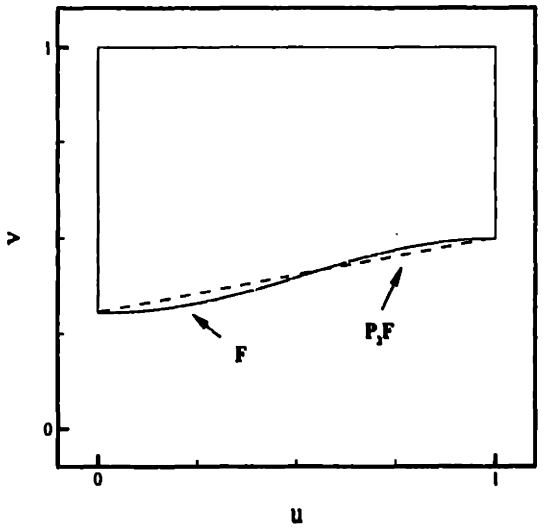

Figure B-4: The error at a boundary due to linear interpolation

involves the four corners of the boundary. Applying (B.8) to a set of typical bounding curves produces the interior surface shown in Figure B-5. The corresponding computational space in plotted in Figure B-6. Also, it is clear that the boundary curves are exactly reproduced by (B.8).

Since the Gordon-Coons mapping is given explicitly, the Jacobian of the $(s,t) \rightarrow (u,v)_{\text{wet}}$ mapping may be found by directly differentiating (B.8).

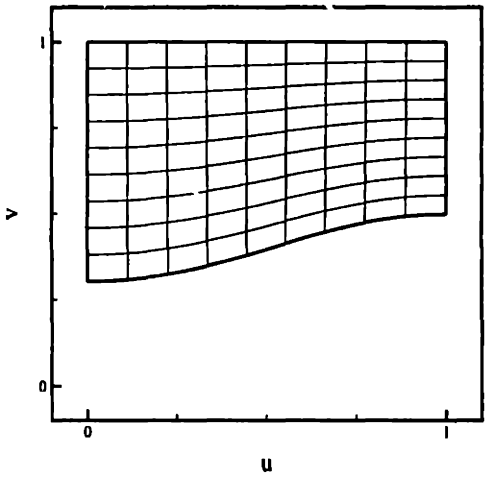

Figure B-5: the wet uv space divided by the interpolation

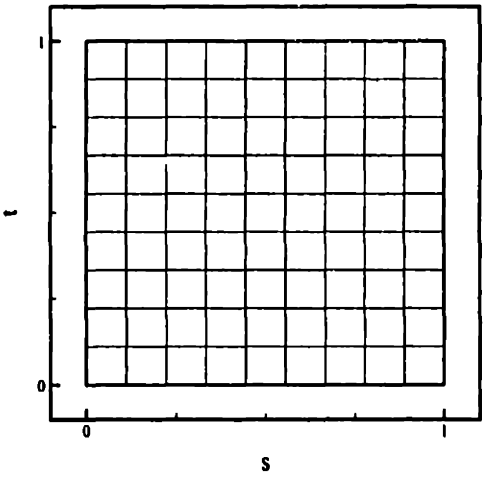

Figure B-6: the st space

Appendix C

Self Influence Quadrature

We wish to evaluate the source self-influence

$$\begin{aligned} I_{ij} &= \iint \mathcal{S}_i \mathcal{T}_j \frac{1}{R} dS \\ &= \iint \mathcal{S}_i \mathcal{T}_j J \frac{1}{R} ds\, dt, \end{aligned} \tag{C.1}$$

and the dipole term

$$H_{ij} = \iint \mathcal{S}_i \mathcal{T}_j \frac{\partial}{\partial n} \frac{1}{R} J\, ds\, dt, \tag{C.2}$$

where, the J is the Jacobian of the $(s,t) \rightarrow \mathbf{X}$ transformation

$$J = \frac{\partial \mathbf{X}}{\partial (s,t)} = \frac{\partial (u,v)}{\partial (s,t)} \frac{\partial \mathbf{X}}{\partial (u,v)}. \tag{C.3}$$

The singularity as $R \rightarrow 0$ in each case requires special care. We will examine how to evaluate (C.2) and extend this to the dipole case. This appendix describes the triangulation and quadrature schemes derived by Newman [41, 42] and Lee [23].

The B-spline basis functions may be expressed as polynomials, centered about the panel's midpoint (s_m, t_m),

$$\mathcal{S} = a_k s'^{k-1} + a_{k-1} s'^{k-2} + \cdots + a_2 s' + a_1 \tag{C.4}$$

$$\mathcal{T} = b_k t'^{k-1} + b_{k-1} t'^{k-2} + \cdots + b_2 t' + b_1, \tag{C.5}$$

where $(s', t') = (s - s_m, t - t_m)$. We can express (C.2) as a linear combination of I^c_{mn},

$$I^c_{mn} = \int_{s'_1}^{s'_2} \int_{t'_1}^{t'_2} s'^{m-1}\, t'^{n-1}\, \frac{1}{R} J\, ds' dt'. \tag{C.6}$$

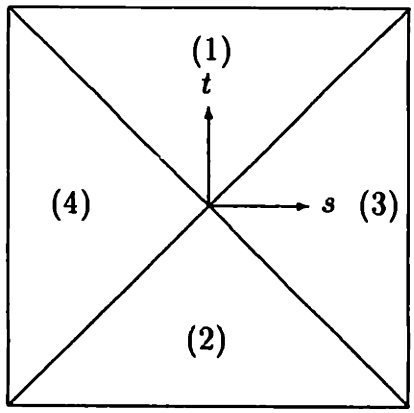

Figure C-1: The self-influence square is further subdivided into four triangles.

With proper subdivision, we may arrive at a square self influence domain centered about the field point's parametric coordinates (see Figure C-1). We begin by centering the square about the field point,

$$(\hat{s},\hat{t}\,) = (s' - s'_f, t' - t'_f), \tag{C.7}$$

and use the polynomial form of the B-spline basis functions to arrive at

$$L^c_{mn} = \int_{\hat{s}_a}^{\hat{s}_b}\int_{\hat{t}_a}^{\hat{t}_b} \hat{s}^{m-1}\,\hat{t}^{n-1}\,\frac{1}{R}\,J\,d\hat{s}d\hat{t}. \tag{C.8}$$

Assuming a regular surface, we may approximate the distance form the field point to the source point, locally, as

$$\begin{aligned} R &= |\mathbf{X}(s,t) - \mathbf{X}(s_f,t_f)| = |\mathbf{X}(\hat{s} - s'_f + s_m, t) - \mathbf{X}(s_f,t_f)| \\ &\approx \left|\frac{\partial \mathbf{X}(s_f,t_f)}{\partial s}\hat{s} + \frac{\partial \mathbf{X}(s_f,t_f)}{\partial t}\hat{t}\right| = \sqrt{e\hat{s}^2 + 2f\hat{s}\hat{t} + g\hat{t}^2}. \end{aligned} \tag{C.9}$$

Here, e, f and g are the first fundamental forms of the surface,

$$\begin{aligned} e &\equiv \mathbf{X}_s(s_f,t_f)\cdot\mathbf{X}_s(s_f,t_f) \\ f &\equiv \mathbf{X}_s(s_f,t_f)\cdot\mathbf{X}_t(s_f,t_f) \\ g &\equiv \mathbf{X}_t(s_f,t_f)\cdot\mathbf{X}_t(s_f,t_f). \end{aligned} \tag{C.10}$$

Normalize the local variables $(\hat{s},\hat{t})$ by the square's half-length

$$\bar{s} = \frac{\hat{s}}{\sigma} \quad , \quad \bar{t} = \frac{\hat{t}}{\sigma} \tag{C.11}$$

where, $\sigma = \frac{s'_b - s'_a}{2} = \frac{t'_b - t'_a}{2}$. This gives

$$L^c_{mn} = \sigma^2 \int_{-1}^{1}\int_{-1}^{1} (\sigma\bar{s} + s_f)^{m-1} (\sigma\bar{t} + t_f)^{n-1} \frac{\sqrt{e\bar{s}^2 + 2f\bar{s}\bar{t} + g\bar{t}^2}}{R} \frac{1}{\sqrt{e\bar{s}^2 + 2f\bar{s}\bar{t} + g\bar{t}^2}} J\, d\bar{s}d\bar{t}. \tag{C.12}$$

Over triangle 1 the above integral becomes

$$L^c_{mn,1} = \sigma^2 \int_{0}^{1}\int_{-1}^{1} f(\bar{s},\bar{t}) \frac{1}{\sqrt{e\bar{s}^2 + 2f\bar{s}\bar{t} + g\bar{t}^2}} J\, d\bar{s}d\bar{t}, \tag{C.13}$$

where,

$$f(\bar{s},\bar{t}) = (\sigma\bar{s} + s_f)^{m-1} (\sigma\bar{t} + t_f)^{n-1} \frac{\sqrt{e\bar{s}^2 + 2f\bar{s}\bar{t} + g\bar{t}^2}}{R}. \tag{C.14}$$

The singularity at $R = 0$ may be analytically removed by introducing the following transformation

$$\bar{s} = x \quad , \quad \bar{t} = xy. \tag{C.15}$$

Substituing this into (C.14) and including the integration over triangle 2,

$$L^c_{mn,1+2} = \sigma^2 \int_{-1}^{1}\int_{-1}^{1} f(x,xy) \frac{1}{\sqrt{e + 2fy + gy^2}} J\, dxdy. \tag{C.16}$$

For triangles 3 and 4, apply the transformation

$$\bar{s} = xy \quad , \quad \bar{t} = x, \tag{C.17}$$

to obtain the non-singular integrals

$$L^c_{mn,3=4} = \sigma^2 \int_{-1}^{1}\int_{-1}^{1} f(x,xy) \frac{1}{\sqrt{ey^2 + 2fy + g}} J\, dxdy. \tag{C.18}$$

We now wish to account for the form of the square-root behavior in the integrations over the four triangles. For $L^c_{mn,1+2}$, let

$$\beta \equiv -\frac{f}{g} \quad , \quad \alpha \equiv \sqrt{\frac{e}{g} - \beta^2}. \tag{C.19}$$

Therefore, (C.16) becomes

$$L^c_{mn,1+2} = \sigma^2 \int_{-1}^{1}\int_{-1}^{1} f(x,xy) \frac{1}{|\mathbf{b}|\alpha\sqrt{1 + \left(\frac{y-\beta}{\alpha}\right)^2}} J\, dxdy. \tag{C.20}$$

This suggest another change of variables:

$$z = sinh^{-1}\left(\frac{y-\beta}{\alpha}\right) \tag{C.21}$$

$$\begin{aligned} dz &= \frac{d}{dy} sinh^{-1}\left(\frac{y-\beta}{\alpha}\right) dy \\ &= \frac{d}{dy} log\left\{\left(\frac{y-\beta}{\alpha}\right) + \sqrt{1+\left(\frac{y-\beta}{\alpha}\right)^2}\right\} dy \\ &= \frac{dy}{\alpha\sqrt{1+\left(\frac{y-\beta}{\alpha}\right)^2}} \end{aligned} \tag{C.22}$$

The lower and upper limits of integration become, respectively, $z_L = \sinh^{-1}\left(\frac{-1-\beta}{\alpha}\right)$ and $z_U = \sinh^{-1}\left(\frac{1-\beta}{\alpha}\right)$. Finally, we use another normalization,

$$z = \frac{z_U - z_L}{2} w + \frac{z_U + z_L}{2} = pw + q, \tag{C.23}$$

to give the integration over triangles 1 and 2,

$$L^c_{mn,1+2} = \sigma^2 p \int_{-1}^{1}\int_{-1}^{1} f(x, x(\alpha sinh(pw+q)+\beta))\frac{1}{|\mathbf{b}|} J\, dx dw, \tag{C.24}$$

and

$$L^c_{mn,3+4} = \sigma^2 p' \int_{-1}^{1}\int_{-1}^{1} f(x(\alpha sinh(p'w+q')+\beta'), x)\frac{1}{|\mathbf{a}|} J\, dx dw, \tag{C.25}$$

for triangles 3 and 4. In the latter integration,

$$\beta' \equiv -\frac{f}{e} \quad , \quad \alpha' \equiv \sqrt{\frac{g}{e} - \beta'^2}. \tag{C.26}$$

We add the integrals over all four triangles and obtain a result for the entire self-influence sqaure.

$$\begin{aligned} L^c_{mn,1+2+3+4} &= \sigma^2 p \int_{-1}^{1}\int_{-1}^{1} f(x, x(\alpha sinh(pw+q)+\beta))\frac{1}{|\mathbf{b}|} J\, dx dw \\ &+ \sigma^2 p' \int_{-1}^{1}\int_{-1}^{1} f(x(\alpha sinh(p'w+q')+\beta'), x)\frac{1}{|\mathbf{a}|} J\, dx dw \end{aligned} \tag{C.27}$$

where

$$f(\bar{s},\bar{t}) = (\sigma\bar{s}+s_f)^{m-1}(\sigma\bar{t}+t_f)^{n-1}\frac{\sqrt{e\bar{s}^2+2f\bar{s}\bar{t}+g\bar{t}^2}}{R} \tag{C.28}$$

for the source singularity, and

$$f(\bar{s},\bar{t}) = (\sigma\bar{s} + s_f)^{m-1}\,(\sigma\bar{t} + t_f)^{n-1}\,\frac{\sqrt{e\bar{s}^2 + 2f\bar{s}\bar{t} + g\bar{t}^2}(\mathbf{R}\cdot\mathbf{N})}{R^3} \qquad \text{(C.29)}$$

for the dipole singularity.

Appendix D

Vector and "Matrix" Cross-Product Notations

Let $\mathbf{a}, \mathbf{b}$, and $\mathbf{c}$ denote the following $3x1$ column vectors,

$$\mathbf{a} = \left\{ \begin{array}{c} a_1 \\ a_2 \\ a_3 \end{array} \right\}, \quad \mathbf{b} = \left\{ \begin{array}{c} b_1 \\ b_2 \\ b_3 \end{array} \right\}, \quad \text{and} \quad \mathbf{c} = \left\{ \begin{array}{c} c_1 \\ c_2 \\ c_3 \end{array} \right\}. \tag{D.1}$$

The vector-vector cross product is defined in the conventionally manner,

$$\mathbf{c} = \mathbf{a} \times \mathbf{b} = \left\{ \begin{array}{c} a_2 b_3 - a_3 b_2 \\ a_3 b_1 - a_1 b_2 \\ a_1 b_2 - a_2 b_1 \end{array} \right\}. \tag{D.2}$$

Define a $3x3$ matrix $[X]$. The "matrix" cross product is defined as

$$\mathbf{a} \times [X] \equiv [\{\mathbf{a} \times \mathbf{x}_1\} \{\mathbf{a} \times \mathbf{x}_2\} \{\mathbf{a} \times \mathbf{x}_3\}], \tag{D.3}$$

where $\mathbf{x}_i$ is the i^{th} column vector of $[X]$. The following idendtities hold for the $3x1$ column vectors $\mathbf{a}$ and $\mathbf{b}$ and $3x3$ sqaure matricies $[X]$ and $[Y]$,

$$\{\mathbf{a} \times [X]\mathbf{b}\} = [\mathbf{a} \times [X]]\mathbf{b} \tag{D.4}$$

$$[\mathbf{a} \times [X][Y]] = [\mathbf{a} \times [X]]\,[Y] \tag{D.5}$$

Bibliography

[1] Robert F. Beck and Allan R. Magee. Time-domain analysis for predicting ship motions. In W.G. Price, Temarel, and A.J. Keane, editors, *Dynamics of Marine Vehicles and Structures in Waves.* Elsevier Science Publishers, 1991.

[2] Harry Bradford Bingham. *Simulating Ship Motions in the Time Domain.* PhD dissertation, Massachusetts Institute of Technology, Department of Ocean Engineering, February 1994.

[3] H.B. Bingham, F.T. Korsmeyer, and J.N. Newman. Prediction of the seakeeping characteristics of ships. In *Proc. of the* 20^{th} *symposium on Naval Hydrodynamics*, Santa Barbara, June 1994.

[4] S.A. Coons. Surfaces for computer aided design of space forms. Technical report, Massachusetts Institute of Technology Project MAC-TR-41, 1967.

[5] W.B. Cummins. The impulse response function and ship motions. *Schiffstecknik*, 9:101–109, 1962.

[6] Marcos Danato Auler da Silia Ferreira. *Second-Order Steady-Forces on Floating Bodies with Forward Speed.* PhD dissertation, Massachusetts Institute of Technology, Department of Ocean Engineering, June 1997.

[7] Douglas Dommeruth. *Numerical Methods for Solving Nonlinear Water Wave Problems in the Time Domain.* PhD dissertation, Massachusetts Institute of Technology, Department of Ocean Engineering, October 1987.

[8] R. Eatock Taylor and J. Knoop. Dynamic instability of a freely floating platform in waves. In G.S.T. Armer and F.K. Garas, editors, *Design for Dynamic Loading - The Use of Model Analysis.* Construction Press, 1982.

[9] O.J. Emmerhoff and P.D. Sclavounos. The slow-drift motion of arrays of vertical cylinders. *Journal Fluid Mech.*, 242:31–50, 1992.

[10] D. V. Evans and R. Porter. Trapped modes about multiple cylinders in a channel. *Journal Fluid Mech.*, 339:331–356, 1997.

[11] Pierre Ferrant. Simulation of strongly nonlinear wave generation and wave-body interactions using a three-dimensional mixed-eulerian-lagrangian model. In *Proc. 21st Symposium on Naval Hydrodynamics*, Trondheim, June 1996.

[12] W.J. Gordon. Blending function methods of bivariate and multivariate interpolation and approximation. *SIAM Journal on Numerical Analysis*, pages 158–177, August 1971.

[13] John L. Hess and A. M. O. Smith. Calculation of nonlifting potential flow about arbitrary three-dimensional bodies. *Journal of Ship Research*, 8(2):22–44, 1964.

[14] Josef Hoschek and Dieter Lasser. *Fundamentals of computer aided geometric design.* AK Peterks, Wellesley, Massachusetts, 1989.

[15] C.Y. Hsin, J.E. Kerwin, and J.N. Newman. A higher-order panel method for ship motions based on b-splines. In *Proc. Sixth International Conference on Numerical Ship Hydrodynamics*, Iowa City, Iowa, August 1993.

[16] Yifeng Huang. *Nonlinear Ship Motions by a Rankine Panel Method.* PhD dissertation, Massachusetts Institute of Technology, Department of Ocean Engineering, February 1997.

[17] H.A. Jacskon. Submarine design trends. Technical report, Massachusetts Institute of Technology, Ocean Engineering Department, Cambridge, Massachusetts, 1991.

[18] D.W. Jordan and P. Smith. *Nonlinear Ordinary Differential Equations*, chapter 9, pages 243–266. Oxford applied mathematics and computing science series. Claredon Press, Oxford, UK, 1987.

[19] D.J. Kim and M.H. Kim. Wave-current interaction with a large three-dimensional body by the higher-order boundary element method. *Journal of Ship Research*, 41(4):273–285, December 1997.

[20] Bradley King. *Time-Domain Analysis of Wave Exciting Forces on Ships and Bodies.* PhD dissertation, University of Michigan, Department of Naval Architecture and Marine Engineering, February 1987.

[21] F.T. Korsmeyer. *The First- and Second-order Transient Free-surface Wave Radiation Problems.* PhD dissertation, Massachusetts Institute of Technology, Department of Ocean Engineering, January 1988.

[22] David C. Kring. *Time Domain Ship Motions by a Three-Dimensional Rankine Panel Method.* PhD dissertation, Massachusetts Institute of Technology, Department of Ocean Engineering, May 1994.

[23] C.-H. Lee. Self-influence quadrature for the geometry-independent higher-order panel method. MIT Computational Hydrodynamics Facility note, 1997.

[24] C.-H. Lee, L. Farina, and J. N. Newman. A geometry-independent higher-order panel method and its application to wave-body interactions. In *Proc. Engineering Mathematics and Applications Conference*, Adelaide, July 1998.

[25] C.-H. Lee, H.D. Maniar, J.N. Newman, and X. Zhu. Computations of wave loads using a b-spline panel method. In *Proc. of the* 21^{st} *Symposium on Naval Hydrodynamics*, Trondheim, June 1996.

[26] C.-H. Lee and J.N. Newman. First- and second-order wave effects on a submerged spheroid. *Journal of Ship Research*, 35(3):183–190, 1991.

[27] C.-H. Lee and J.N. Newman. Second-order wave effects on offshore structures. In *Proc. Seventh International Conference on the Behavior of Offshore Structures*, Boston, August 1994.

[28] Stergios John Liapis. *Time Domain Ship Analysis of Ship Motions.* PhD dissertation, University of Michigan, Department of Naval Architecture and Marine Engineering, April 1986.

[29] W.-M. Lin and D.K.P. Yue. Numerical simulations for large-amplitude ship motions in the time domain. In *Proc. of the* 18^{th} *Symposium on Naval Hydrodynamics*, Ann Arbor, Michigan, 1990.

[30] Woei-Min Lin. *Nonlinear Motion of the Free Surface Near a Moving Body.* PhD dissertation, Massachusetts Institute of Technology, Department of Ocean Engineering, September 1984.

[31] Yming Liu. *Nonlinear Wave Interactions with Submerged Obstacles With or Without Current.* PhD dissertation, Massachusetts Institute of Technology, Department of Ocean Engineering, May 1994.

[32] M.S. Longuet-Higgins, F.R.S., and E.D. Cokelet. The deformation of steep surface waves on water. In *Proc. Royal Society of London*, volume 350, pages 1–26, 1976.

[33] Allan Magee. Seakeeping applications using a time-domain method. In *Proc. of the* 20^{st} *Symposium on Naval Hydrodynamics*, Santa Barbara, June 1994.

[34] Allan R. Magee. *Large-Amplitude Ship Motions in the Time Domain.* PhD dissertation, University of Michigan, Department of Naval Architecture and Marine Engineering, February 1991.

[35] H.D. Maniar and J.N. Newman. Wave diffraction by a long array of cylinders. *Journal Fluid Mech.*, 339:309–330, 1997.

[36] Hiren Dayalal Maniar. *A Three Dimensional Higher Order Panel Method Based on B-Splines.* PhD dissertation, Massachusetts Institute of Technology, Department of Ocean Engineering, September 1995.

[37] H. Maruo. The drift of a body floating in waves. *Journal of Ship Research*, 4(3):1–10, 1960.

[38] A.J. Musker. Prediction of wave forces and moments on a near-surface submarine. *International Shipbuilding Progress*, 31:2–12, 1984.

[39] D.E. Nakos. *Ship Wave Patterns and Wave Patterns by a Three Dimensional Rankine Panel Method.* PhD dissertation, Massachusetts Institute of Technology, Department of Ocean Engineering, 1990.

[40] Ali Hasan Nayfeh and Dean T. Mook. *Nonlinear Oscillations*, chapter 5, pages 273–279. Oxford applied mathematics and computing science series. John Wiley and Sons, New York, NY, 1987.

[41] J. N. Newman. A quadrature for integrating the rankine self-influence functions on an arbitrary patch - i. MIT Computational Hydrodynamics Facility note, March 1996.

[42] J. N. Newman. A quadrature for integrating the rankine self-influence functions on an arbitrary patch - ii. MIT Computational Hydrodynamics Facility note, July 1997.

[43] J.N. Newman. The drift force and moment on ships in waves. *Journal of Ship Research*, 11:51–60, 1967.

[44] J.N. Newman. *Marine Hydrodynamics.* MIT Press, Cambridge, MA, 1977.

[45] J.N. Newman. The theory of ship motions. *Advances in Applied Mechanics*, 18:221+, 1978.

[46] J.N. Newman. To second order and beyond. In *Tension Leg Platform Technology*, Proc. of the Fourth Offshore Symposium, Houston, February 1995. The Texas Section of the Society of Naval Architecture and Marine Engineers.

[47] Jan Nossen, John Grue, and Enok Palm. Wave forces on three-dimensional floating bodies with small forward speed. *Journal Fluid Mech.*, 227:135–160, 1991.

[48] Jens Olav Nygaard and John Grue. Wavelet and spline methods for the solution of wave-body problems. In *Proc. of the* 12^{th} *International Workshop of Water Waves and Floating Bodies*, Carry-le-Rouet, March 1997.

[49] T.F. Ogilvie. Recent progress toward the understanding and prediction of ship motions. In *Proc.* 5^{th} *Symposium on Naval Hydrodynamics*, Bergen, September 1964.

[50] T.F. Ogilvie. Second-order hydrodynamic effects on ocean platforms. In *International Workshop on Ship and Platform Motions*, Berkeley, 1983.

[51] Makoto Ohkusu. Ship motions in the vicinity of a structure. In *Proc. Behavior of Offshore Structures*, Trondheim, August 1976.

[52] R.C.T. Rainey. Parasitic motions of offshore structures. In *The Royal Institute of Naval Architects*, volume 123, pages 177–194, 1981.

[53] J.J. Stoker. *Water Waves.* Pure and Applied Mathematics. Interscience Publishers, INC., New York, 1957.

[54] Michael S. Triantafyllou. A consistent hydrodynamic theory for morred and positioned vessels. *Journal of Ship Research*, 26(2):97–106, 1982.

[55] T. Vinje and P. Brevig. Numerical simulation of breaking waves. *Adv. Water Resources*, 4:77–82, June 1981.

[56] J. V. Wehausen and E. V. Laitone. Surface waves. *Handbuch der Physik*, 9:446–778, 1960.

[57] P. Wilmott. On the motion of a slender body submerged beneath surface waves. *Journal of Ship Research*, 32:208–19, 1988.